EUSKAL HERRIKO UNIBERTSITATEA
THE UNIVERSITY OF THE BASQUE COUNTRY

A Rigorous Exploration of the Plexcitonic Phenomena: Hybridized Light-Matter States using Gold Nanoparticles and J-aggregates

Thesis by

Alba María Jumbo Nogales

Supervised by

Prof. Yury Rakovich
Dr. Marek Grzelczak

Donostia-San Sebastián, March 2024

To my grandparents Inés and Armando,
my aunts Sulma and Mercedes,
my parents María and Patricio,
and my sisters: Belén,
Nazareth and Sofía,
You are my greatest inspiration.

ACKNOWLEDGMENTS

I would like to thank my thesis supervisors: Yury Rakovich and Marek Grzelczak for allowing me to join the Nanomaterials and Spectroscopy and the Colsyschem research group, and for the time they devoted to this work. Being part of these research groups led me to meet amazing scientists who played a key role in the development and completion of this doctorate, and now I consider them as part of my doctorate-built family.

The first members I met were Joscha and María who helped me with my first gold nanoparticles synthesis and shared with me the tricks and tips to improve my experimental work. Especially María, because she shared with me her expertise in gold nanoparticle functionalization: your suggestion saved my second plexcitonic system.

One year later, Zuzanna Lawera joined the group. Zuzzy, you know I consider you my lab sister, always eager to discuss stuff related to molecules and the ligand exchange process. I'll be forever grateful for your friendship, and your support in the difficult moments but also for celebrating with me every small success happening through this PhD journey. I was lucky to share this whole experience with you. And for sure for the swimming training! There was no turning back for me after learning how to do the flips. (Also for teaching me how to pronounce Marek's surname properly, which is not trivial for a non-Polish speaker, and if you doubt, please, go to the beginning of this page and test yourself).

Some months after Zuzanna, Adam Olejniczak joined our group. First, I have to thank Adam because of his commitment to measuring the luminescence response of my samples and obtaining beautiful spectra (we got splitting there!). Also for resolving my doubts about time-resolved measurements and the Purcell effect. More importantly, because of his friendship, his dedication to teaching me proper Polish (Moje rzeczy), and also for ensuring that I will survive during the manuscript writing process. Dziękuję bardzo, Zuzzy and Adamito!

Anish Rao arrived just a year ago, but I've shared with you so many enthusiastic discussions about plexcitonic systems. Thank you for your dedicated corrections throughout this work, and for all the time you spent answering my questions.

¡Muchas gracias, Anish-shifu!

I would like to thank Sabine for her valuable advice about Ph.D. life, the amazing breakfasts, hanging out, hikes, and all the time we have shared, but mainly for being the best flatmate I could ever imagine: Vielen Dank!

And to all the incredible persons that I had the pleasure to know: Ane, Jozef, Jehyeok, Victor, Ché Mikel y Mario (mis inolvidables primeros compañeros de despacho), Carlos (wey, gracias por obligarme a hacer amigos, ja, ja, ja), Raúl (gracias por contestar mis dudas respecto al depósito de la tesis), Jorge (por las tardes en la playa de Ondarreta y ayudarme a perder el miedo a nadar en el mar), Auguste (gracias por compartir tus habilidades culinarias), Fer (mi primer amigo transferido a Hamburgo), Miriam (nos vemos pronto en Austria), Dorde, Jason, Sha, Rubén (el bueno), Alberto (y Jano), María (de Canarias), Carolina, Aye, Coco, Katherina, Nathaniel, Paschalis y Divya. I feel fortunate to have found such a nice group of people to talk to and share our lunchtime, pintxos, sociedades, or Quantum Breakfasts. Meet you all made this journey a rewarding experience.

También quisiera mencionar y agradecer a Uxue, por ser parte de los profesionales a quienes admiro por la dedicación y cariño con el cual realizan su trabajo. Fundamentalmente por compartir su tiempo y comprensión para conmigo.

Por otro lado también me gustaría agradecer a mi familia, que siempre ha encontrado la manera de hacerme saber cuánto me quieren, pese a la distancia. A mis padres por haberme apoyado en todo momento, por más fuera de lugar que haya sonado en un principio que fuese a estudiar física o a hacer una maestría y después un doctorado a más de un océano de distancia. A mis hermanas: Belén, Nazareth y Sofía, por ser mi inspiración diaria a ser una mejor persona y una buena profesional. A mis tías: Mercedes y Sulma por su incansable dedicación para conmigo y su ejemplo diario como seres humanos extraordinarios. A mis abuelitos Inés y Armando por haberme obsequiado con una infancia feliz y completa: sé que desde algún lugar sois testigos de mis pequeños logros. A todos mis tíos y primos, porque aunque este sea un paso profesionalmente importante, lo que ha sido fundamental es contar con todos vosotros como familia.

A Pablo, por haber sido y seguir siendo mi aliado macroscópico más pertinaz. Te agradezco por haberme acompañado en este camino desde hace casi ocho años y sobretodo por haber estado a mi lado durante estos últimos tres, que han sido una prueba de fuego para los dos en muchos sentidos.

Al personal del CFM, que con su dedicación nos hacen el día a día más fácil: Mari Jose, Idoia, Feli, Koldo, Gotzon, Ibai, Maite, Ekain, Juan, María Formoso y a todos aquellos que no recuerdo su nombre por mi mala memoria.

Last, but not least I would like to thank the people organizing and taking care of the CFM's Ph.D. fair, this represented a nice opportunity to join the CFM team. This doctorate experience (for me) and the present work would not be possible without the funding and the ones who put their effort into making these fairs a reality.

Abstract

The study of light-matter interaction has long captivated scientific inquiry, dating back to the earliest investigations in science. Over time, this fascination has evolved from basic observations of natural phenomena to more sophisticated inquiries to understand the underlying principles governing these interactions. Initially, scientific curiosity was centered around fundamental phenomena like light reflection, refraction, scattering, absorption, emission, etc. These foundational understandings provided a basis for delving into more complex processes like photoinduced energy transfer, photoinduced electron transfer, photothermal heating, etc.

As scientific inquiry progressed, there was a shift from passive observation and explanations of natural phenomena to active manipulation of light-matter interactions for practical applications. This paradigm shift led to the development of various technologies and methodologies, including metamaterials, photonic integrated circuits, and advancements in fields such as solar water desalination, photocatalysis, and artificial photosynthesis. However, in all these processes, the identity of the material components was retained thereby limiting the properties of the system to the inherent characteristics of the materials involved. For example, a highly efficient photocatalyst fabricated from water-unstable materials would be unsuitable for aqueous photocatalytic reactions. Moreover, despite the remarkable advancements, many applications of light were limited by its role as merely an energy source or mediator, lacking the ability to fundamentally alter the properties of materials.

To address this limitation, researchers began investigating new approaches where light could induce transformative changes in material properties. This led to the proposal and subsequent confirmation of a fundamentally new process, representing a paradigm shift in our understanding of light-matter interactions. These systems involved a cavity interacting with excitonic components, potentially altering their fundamental identities.

In the late 20th century, the exploration of coupling between light and material states ushered in a new era of scientific discovery. Theoretical frameworks suggested that in such hybrid systems, excitonic components could exhibit properties distinct from their conventional behaviors, such as enhanced photostability, catalytic selectivity, improved conductivity, etc. Initial demonstration of strong coupling was done

for an ensemble of Rydberg atoms in a millimeter cavity. Following this, different types of cavities like Fabry–Perot, Bragg reflectors, micropillar, or microdisk cavities were utilized to couple to a wide variety of emitters like quantum dots, dye molecules, single atoms, and quantum wells. Later, similar coupling phenomena were also expanded to using plasmonic cavities (like plasmonic arrays) for coupling to electronic transitions. Here, plasmons emerged as an appealing choice for coupling with excitons due to their unique ability to confine electromagnetic energy at nanoscale dimensions.

In the realm of strong coupling between plasmonic cavity modes and excitons, extensive research has been conducted to study and exploit these unique light-matter interactions for various applications. Initial studies aimed to demonstrate the feasibility of achieving strong coupling using plasmonic cavities and excitons across diverse material systems, including organic molecules, quantum dots, and 2D materials. This was accomplished by precisely engineering the geometry of the cavity and properties of the exciton to achieve resonant interactions. Subsequently, researchers have developed several techniques to adjust the strength of coupling between plasmonic cavities and excitons. These techniques involve modifying parameters such as cavity size, material properties, and external stimuli like temperature or applied fields. By doing so, researchers have successfully tuned the coupling strengths between the cavity and excitonic system. These strong coupling interactions have been shown to induce modifications in emission and absorption spectra, enhance light absorption, and facilitate energy transfer processes. These findings hold promise for a wide range of potential applications in the field of sensing and catalysis.

Researchers explored individual plasmonic nanoparticles as nanocavities in a parallel effort to develop systems demonstrating strong coupling with electronic energy states. Leveraging the tunability of plasmonic nanoparticles, the fabrication and assembly of plexcitonic systems was greatly simplified. Furthermore, nanoparticles provide localized enhancements in electromagnetic fields, fostering intense interactions between light and matter compared to plasmonic films and arrays. Additionally, adjusting nanoparticle shapes and sizes enables straightforward control over electric field enhancements and resonance wavelengths, facilitating efficient coupling with different excitonic components.

The interaction between plasmonic nanocavity modes and excitons from both semiconductors and molecules has been extensively studied. These explorations have provided insights into the advantages and limitations associated with selecting different excitonic components. Among these components, J-aggregates have gained significant attention due to their intriguing photophysical properties, such as their sharp and narrow spectral signature, a significantly small Stokes shift, or a high oscillator strengh. These characteristics render J-aggregates highly attractive as excitonic components, offering unique insights into light-matter interactions at the nanoscale.

In the present thesis, we opted to utilize gold (Au) nanoparticles as our preferred cavity and molecular aggregates (J-aggregates) as the excitonic component for establishing plexcitonic systems. Our objective was mainly, to conduct thorough

studies and analyses aimed at understanding plexcitonic systems, and subsequently, to showcase their photophysical properties and potential for photocatalytic applications. Furthermore, we present robust design principles for constructing strongly coupled plexcitonic systems, laying the groundwork for future applications in this domain.

This thesis progresses by initially conducting a detailed analysis of the excitonic component alone, specifically focusing on J-aggregates of S2275 and JC-1 dyes. Subsequently, we chose Au bipyramids as our plasmonic component and explored two independent interactions to reliably assemble a colloidally stable dispersion of plexcitonic systems. To achieve this, we synthesized a series of Au bipyramids having different aspect ratios to obtain longitudinal surface plasmon resonance (LSPR) responses ranging from 560 to 980 nm. This diverse range of Au bipyramids is crucial for conducting controlled and sequential detuning studies, enabling the estimation of coupling strengths between the plasmonic and excitonic components. Following the synthesis of Au bipyramids, two independent interactions (namely electrostatic interactions and dye intercalation) were employed to drive the formation of the plexcitonic systems with S2275 and JC-1 dyes. After the successful formation of the plexcitonic system, we carried out comprehensive photophysical studies to estimate the coupling strengths in both systems. Later, we examined the effect of strong coupling on the photophysical and photochemical properties of the system, specifically focusing on photostability. Remarkably, we observed significant improvements in the photostability of the dyes when strongly coupled to the plasmonic nanoparticles. The research presented in this thesis lays a strong foundation for future studies exploring the effects of strong coupling for photocatalytic and sensing applications. In subsequent paragraphs, a comprehensive summary of the thesis is provided, outlining the research conducted in each chapter.

The second chapter examines the Frenkel excitons' coherence length (N_{coh}) in two different J-aggregate systems. N_{coh} is one of the most critical parameters governing many key features of supramolecular J-aggregates. However, experimentally determining the value of N_{coh} is a non-trivial task since it is sensitive to the technique/method applied, causing discrepancies in literature data even for the same chemical compound and aggregation conditions. To pursue this analysis, we applied a combination of different experimental techniques including UV-Vis, fluorescence emission, time-resolved photoluminescence, and transient absorption spectroscopies, and estimated N_{coh} values for J-aggregates for both S2275 and JC-1 dyes. We found that the method based on absorption spectroscopy alone - a widely used technique- fails in determining correct N_{coh} values. We observe that a better approach is based on the analysis of the modification of photoluminescence lifetime, the nonlinear response upon aggregation, and careful study of the Stokes shift and electron-phonon coupling strengths. The average value of N_{coh} for both dyes was estimated to be 4 molecular units, taking into account the estimations made from every applied method. To complete this analysis, we estimated the value of the exciton oscillator strength for both J-aggregates since this parameter is related to achieving the strong coupling regime in plexcitonic systems.

After analyzing the excitonic components, our investigation transitioned to ex-

amining the properties of plexcitonic systems incorporating Au bipyramids.

In the third chapter, we present the results of a study on a hybrid system formed by electrostatically binding TMA-coated Au bipyramids (positively charged) with J-aggregates of S2275 dye (negatively charged). Here, we demonstrate the enhanced photochemical properties of the plexcitonic system compared to standalone J-aggregates. Our analysis includes UV-vis-NIR and photoluminescence characterization of the system, revealing the remarkable plexcitonic interaction and pronounced coupling effect. Detailed UV-vis analysis involving decoupling of plasmon response to the absorbance of J-aggregates enabled the investigation of the coupling strength (g). Additionally, the photoluminescence response of both J-aggregates and coupled systems reveals the impact of the plexcitonic coupling on the emission properties. We employed fluorescence lifetime imaging microscopy (FLIM), to explore the effect of plexcitonic coupling on the photoluminescence lifetime components of J-aggregates within the plexcitonic system. Finally, we conducted a comparative analysis to study the photodegradation of J-aggregates in the presence and absence of plexcitonic hybrids. Our results demonstrate that plasmon-enhanced interactions notably enhance the photostability of J-aggregates, extending their stability to 2.5 hours within the plexcitonic hybrids. While this improvement is significant, the colloidal stability of the particles represents a big limitation within this system. We anticipate even greater enhancements in the photophysical properties of J-aggregates with stronger coupling strengths, alongside the fabrication of highly stable plexcitonic hybrids.

To overcome the above-mentioned limitation, we developed a second plexcitonic system utilizing Au bipyramids and J-aggregates of JC-1 dye. The fourth and fifth chapters of this thesis focus on analyzing the photophysical properties of the plexcitonic system formed using JC-1 dye and exploring its potential for fabricating stimuli-responsive systems.

In this part of the work, we developed a hybrid system consisting of CTAB-coated Au bipyramids as the plasmonic component. The ability of JC-1 molecules to intercalate between surfactant bilayers was used as the driving force to initiate the formation of a plexcitonic system. Both plasmonic nanoparticles and JC-1 dyes were suitably chosen to interact and couple with each other. After establishing the interaction between plasmonic and excitonic components, pH was used to induce the formation of J-aggregates with JC-1 dye and initiate the subsequent plexcitonic coupling of the system. Here, CTAB bilayers played a crucial role in trapping molecular chains, creating a favorable environment for strong coupling interaction. Subsequently, we conducted a comprehensive analysis using UV-Vis-NIR and photoluminescence characterization to characterize the plexcitonic system. Next, we used systematic detuning studies to determine the coupling strength of the system. This involved synthesizing a series of bipyramids with different LSPR peaks to systematically manipulate the plasmonic response according to the J-aggregates response at 600 nm. Through systematic experimentation, we estimated parameters confirming that the prepared plexcitonic system operates within the strongly coupled regime.

Interestingly, the photoluminescence spectra of this system at room tempera-

ture exhibited significant modifications too due to plasmon-exciton interaction, an uncommon observation. Specifically, we observed a doublet feature in the photoluminescence spectra of the plexcitonic system, in parallel with UV-vis spectra modification. Next, we used a reported theoretical model and analyses of the modified photoluminescence spectra to confirm strong coupling interactions. Finally, we investigated the effect of strong coupling on modifying the properties of J-aggregates, particularly their photostability. Impressively, while J-aggregates of JC-1 dye typically photodegrade in less than 1 hour, we observed negligible degradation in the strongly coupled system even after 1 day. This superior photostability demonstrates the potential of strong coupling interactions in modifying the photochemical and photophysical properties of excitonic systems.

Finally, in the last chapter, we extended our investigation into a new domain. While most plexcitonic systems reported are static and cannot be altered once formed, we aimed to create a switchable plexcitonic system by controlling the aggregation of JC-1 dye. Here, we successfully demonstrate pH-responsive modulation of coupling strength between the plasmonic and excitonic components in the plexcitonic system. Given the sensitivity of the J-aggregates in our plexcitonic system to pH, we explored the possibility of using pH to switch between a fully coupled and uncoupled state. JC-1 formed J-aggregates at high pH, resulting in a strongly coupled plexcitonic system with Au bipyramids. Conversely, at lower pH, the disassembly of J-aggregates disrupted the plexcitonic system. Notably, we achieved complete reversibility in the assembly and disassembly of the system and the corresponding formation and destruction of strong coupling in the plexcitonic system respectively. Importantly, this reversibility in the assembly as well as strong coupling was demonstrated for three cycles. Throughout the reversibility cycles, detailed time-dependent UV-Vis and photoluminescence studies were conducted to analyze assembly/disassembly kinetics and assess coupling strength under varying pH conditions. As a result, we observe a slow decoupling with decreasing pH and fast reverse coupling with increasing pH respectively. These sluggish kinetics allowed for the estimation of coupling strength at each stage using a theoretical model of coupled oscillators. Finally, a comprehensive examination of the effect of pH on the plasmonic and excitonic components allowed us to study in detail the mechanism of reversibility. Since the influence of pH on the JC-1 molecule was critical for establishing a reversible plexcitonic system.

Resumen

El estudio de la interacción de la luz con la materia ha captado la curiosidad de los científicos desde hace mucho tiempo, remontándose a la época en que se iniciaban las primeras investigaciones científicas. Con el paso del tiempo, esta fascinación ha evolucionado de simples observaciones básicas de fenómenos naturales a investigaciones más complejas que permitan la comprensión de los principios subyacentes que rigen estos procesos. Al principio, la curiosidad científica se centraba en analizar fenómenos fundamentales como la reflexión, refracción, dispersión, absorción o emisión de la luz. Y de esto se adquirieron los conocimientos fundamentales que, más tarde, sirvieron de base para profundizar en procesos más complejos como la transferencia de energía fotoinducida, la transferencia de electrones fotoinducida o el calentamiento fototérmico.

El progreso de la investigación científica ha permitido el cambio de la observación pasiva y la explicación de los fenómenos naturales hacia la manipulación activa de las interacciones de la luz con la materia para aplicaciones prácticas. Este cambio de paradigma ha conducido al desarrollo de diversas tecnologías y metodologías, como los metamateriales, los circuitos fotónicos integrados y los avances en campos como la desalinización solar del agua, la fotocatálisis y la fotosíntesis artificial. Sin embargo, en todos estos procesos se ha mantenido la identidad de los componentes materiales, limitando así las propiedades del sistema a las características inherentes de los materiales implicados. Por ejemplo, un fotocatalizador altamente eficiente fabricado a partir de materiales inestables en el agua no sería el indicado para las reacciones fotocatalíticas acuosas. Además, a pesar de los notables avances, muchas aplicaciones de la luz se han visto limitadas por su papel como mera fuente de energía o mediador, ya que carecen de la capacidad de alterar las propiedades fundamentales de los materiales.

Para hacer frente a esta limitación, los investigadores empezaron a investigar nuevos enfoques que permitiesen que la luz pudiera inducir cambios transformadores en las propiedades de los materiales. Lo cual condujo a la propuesta y posterior confirmación de un proceso fundamentalmente nuevo y, con esto, un cambio de paradigma en la comprensión de las interacciones la luz con la materia. Los sistemas desarrollados en este contexto implicaban el uso de una cavidad que interactúa con

componentes excitónicos, alterando potencialmente sus identidades fundamentales.

A finales del siglo XX, la exploración del acoplamiento entre la luz y los estados materiales inauguró una nueva era de descubrimientos científicos. Los marcos teóricos sugerían que, en tales sistemas híbridos, los componentes excitónicos podrían exhibir propiedades distintas de sus comportamientos convencionales, como una mayor fotoestabilidad, selectividad catalítica, mejor conductividad, etc. La demostración inicial de lo que se conoce como acoplamiento fuerte se realizó con un conjunto de átomos de Rydberg en una cavidad milimétrica. Después de esto, la aplicación del acoplamiento fuerte se extendió a distintos tipos de cavidades, como Fabry-Perot, reflectores de Bragg, micropilares o microdiscos, que permitían su acoplamiento con una amplia variedad de emisores, tales como puntos cuánticos, moléculas de pigmentos, átomos individuales y pozos cuánticos. Más tarde, estos fenómenos de acoplamiento se ampliaron al uso de cavidades plasmónicas (como las matrices plasmónicas) para llevar a cabo el acoplamiento con transiciones electrónicas. Es entonces cuando los plasmones surgen como una atractiva opción para el acoplamiento con excitones, esto debido a su capacidad única de confinar la energía electromagnética en dimensiones en la nanoescala.

Se han llevado a cabo numerosas investigaciones para estudiar las interacciones del acoplamiento fuerte entre modos de cavidades plasmónicas y excitones, con el fin de explotar estas interacciones únicas entre luz y materia en diversas aplicaciones. Los estudios iniciales tenían como objetivo demostrar la viabilidad de lograr un acoplamiento fuerte utilizando cavidades plasmónicas y excitones en diversos sistemas materiales, incluyendo moléculas orgánicas, puntos cuánticos y materiales 2D. Este acoplamiento se consiguió llevando a cabo un diseño preciso de la geometría de la cavidad y las propiedades del excitón, que a su vez permitió obtener interacciones resonantes. Posteriormente, los investigadores han desarrollado varias técnicas para ajustar la intensidad del acoplamiento entre las cavidades plasmónicas y los excitones. Estas técnicas consisten en modificar parámetros como el tamaño de la cavidad, las propiedades del material y estímulos externos como la temperatura o los campos electromagnéticos aplicados. De este modo se han conseguido ajustar la intensidad del acoplamiento entre la cavidad y el sistema excitónico. Además, se ha demostrado que estas interacciones de acoplamiento fuerte inducen modificaciones en los espectros de emisión y absorbancia, ampliando el rango de absorción de la luz y facilitando los procesos de transferencia de energía. Todos estos hallazgos resultan prometedores para una amplia gama de potenciales aplicaciones en el campo de la detección y la catálisis.

La aplicación de nanopartículas plasmónicas individuales, como nanocavidades, representa un esfuerzo paralelo en el desarrollo de sistemas que demuestren un fuerte acoplamiento con los estados electrónicos de energía. El aprovechamiento de la capacidad de sintonización de la respuesta plasmónica en las nanopartículas, ha simplificado enormemente la fabricación y ensamblaje de sistemas plexcitónicos. Además, estas nanopartículas proporcionan mejoras locales en los campos electromagnéticos, originando interacciones intensas entre la luz y la materia. Esto en comparación al desempeño de películas y matrices plasmónicas. Asimismo, el ajuste de la forma y el tamaño de las nanopartículas permite un control directo sobre estas mejoras del

campo eléctrico y las longitudes de onda de resonancia, facilitando un acoplamiento eficaz con distintos componentes excitónicos.

La interacción entre los modos plasmónicos de las nanocavidades y los excitones de semiconductores y moléculas ha sido objeto de numerosos estudios. Estas investigaciones han permitido comprender las ventajas y limitaciones asociadas a la selección de distintos componentes excitónicos. Entre estos componentes, los J-agregados han sido objeto de gran atención debido a sus interesantes propiedades fotofísicas, tales como su respuesta espectral definida y estrecha, un desplazamiento de Stokes significativamente pequeño o una elevada fuerza oscilatoria. Estas características hacen de los J-agregados unos componentes excitónicos muy atractivos, ofreciendo una perspectiva única de las interacciones de la luz con la materia en la nanoescala.

En la presente tesis, hemos optado por el uso de nanopartículas de oro (Au), como cavidad, y agregados moleculares (J-agregados), como componente excitónico, para establecer sistemas plexcitónicos. El objetivo principal consistió en realizar estudios y análisis exhaustivos para comprender el funcionamiento de los sistemas plexcitónicos y, posteriormente, mostrar sus propiedades fotofísicas y su potencial para aplicaciones fotocatalíticas. Además, presentamos unos principios de diseño robustos para construir estos sistemas fuertemente acoplados, sentando las bases para futuras aplicaciones en este campo.

Esta tesis inicia con un análisis detallado del componente excitónico, centrándose específicamente en los J-agregados de los pigmentos S2275 y JC-1. Posteriormente, tras elegir a las bipirámides de Au como nuestro componente plasmónico, se exploran dos interacciones independientes para constituir de forma fiable la dispersión coloidalmente estable de sistemas plexcitónicos. Para lograrlo, sintetizamos una serie de bipirámides de Au, variando su longitud, para obtener respuestas de resonancias plasmónicas superficiales longitudinales que oscilan entre 560 y 980 nm. Esta diversidad de tamaño en las bipirámides de Au es crucial para llevar a cabo estudios de dispersión de resonancias controlados y secuenciales, permitiendo la estimación de las fuerzas de acoplamiento entre los componentes plasmónicos y excitónicos. Tras la síntesis de las bipirámides de Au, se emplearon dos interacciones independientes (interacciones electrostáticas e incrustación de moléculas de pigmento) para impulsar la formación de los sistemas plexcitónicos con los pigmentos S2275 y JC-1. Tras conseguir formación del sistema plexcitónico, se han llevado a cabo estudios fotofísicos exhaustivos para estimar la fuerza de acoplamiento en ambos sistemas. Posteriormente, se ha examinado el efecto del acoplamiento fuerte sobre las propiedades fotofísicas y fotoquímicas del sistema, centrándonos específicamente en la fotoestabilidad. Sorprendentemente, se observaron mejoras significativas en la fotoestabilidad de los colorantes al acoplarse fuertemente a las nanopartículas plasmónicas. La investigación presentada en esta tesis sienta unas bases sólidas para futuros estudios que exploren los efectos del acoplamiento fuerte en aplicaciones fotocatalíticas y de sensores. En los párrafos siguientes se ofrece un resumen exhaustivo de la tesis, en el que se esboza la investigación realizada en cada capítulo.

El segundo capítulo se ha dedicado al estudio de la longitud de coherencia del

excitón de Frenkel (N_{coh}) en dos sistemas diferentes de J-agregados. N_{coh} es uno de los parámetros más críticos que rigen muchas características clave de los J-agregados supramoleculares. Sin embargo, determinar experimentalmente el valor de N_{coh} no es una tarea trivial debido a la sensibilidad de este parámetro a la técnica/método aplicado. Lo cual puede causar discrepancias en los datos presentados en la literatura, incluso para los mismos compuestos químicos e idénticas condiciones de agregación. Para llevar a cabo este análisis, se ha aplicado una combinación de diferentes técnicas experimentales, incluyendo UV-Vis, emisión de fluorescencia, fotoluminiscencia de resolución temporal y espectroscopias de absorción de transición. Tomando en cuenta esta información, se realizó la estimación de los valores de N_{coh} para los J- agregados, tanto para el pigmento S2275 como para JC-1. Como resultado, se descubrió que el método basado únicamente en la espectroscopia de absorción, una técnica ampliamente utilizada, no provee los valores correctos de N_{coh}. También se observó que existe un enfoque mejor, el cual está basado en el análisis de la modificación del tiempo de vida de la fotoluminiscencia, la respuesta no lineal derivada de la agregación y el estudio cuidadoso del desplazamiento de Stokes y las intensidades de acoplamiento electrón-fonón. El valor promedio de N_{coh} para ambos pigmentos se estimó en 4 unidades moleculares, teniendo en cuenta los cálculos llevados a cabo a partir de cada método aplicado. Para completar este análisis, también se estimaron los valores de la fuerza del oscilador excitónico para ambos J-agregados, ya que este parámetro está relacionado con la obtención de un sistema plexcitónico en el régimen de acoplamiento fuerte.

Tras el análisis de los componentes excitónicos, nuestra investigación pasa al estudio de las propiedades de los sistemas plexcitónicos que incorporan bipirámides de Au.

En el tercer capítulo, se presentan los resultados del estudio realizado sobre un sistema híbrido formado por la unión electrostática de bipirámides de Au recubiertas de TMA (cargadas positivamente) con J-agregados del pigmento S2275 (cargados negativamente). En este contexto se demuestran las propiedades fotoquímicas mejoradas del sistema plexcitónico en comparación con los J-agregados independientes. Este análisis incluye caracterización UV-vis-NIR y de fotoluminiscencia del sistema, revelando la notable interacción plexcitónica y el pronunciado efecto de acoplamiento. Mediante la dispersión de las respuestas de resonancia de las nanopartículas de oro con respecto a la respuesta excitónica, se ha investigado el valor de la fuerza de acoplamiento (g) en este sistema. Además, la fotoluminiscencia, tanto de los J-agregados como de los sistemas acoplados, revela el impacto del acoplamiento plexcitónico en las propiedades de emisión. Para esto, se ha empleado microscopía de imagen de tiempos de vida de la fluorescencia, que permite explorar el efecto del acoplamiento plexcitónico en los componentes de los tiempos de vida de la fotoluminiscencia de los J-agregados dentro del sistema plexcitónico. Por último, se ha realizado un análisis comparativo para estudiar la fotodegradación de los J-agregados en presencia y ausencia de híbridos plexcitónicos. De lo cual se obtuvo que las interacciones potenciadas por plasmones mejoran notablemente la fotoestabilidad de estos J-agregados, ampliando su estabilidad a 2,5 horas dentro de los híbridos plexcitónicos. Aunque esta mejora es significativa, la estabilidad coloidal

de las partículas representa una gran limitación dentro de este sistema. Pero, prevemos mejoras aún mayores en las propiedades fotofísicas de los J-agregados con mayor fuerza de acoplamiento, junto con la fabricación de híbridos plexcitónicos altamente estables.

Con el objetivo de salvar la limitación dada por la estabilidad coloidal de las partículas, se ha desarrollado un segundo sistema plexcitónico. Para esto, también se han utilizado bipirámides de Au y, en este caso, J-agregados de pigmento JC-1. Los capítulos cuarto y quinto de esta tesis se centran en el análisis de las propiedades fotofísicas del mencionado sistema plexcitónico, formado con el pigmento JC-1, y en la exploración de su potencial para fabricar sistemas sensibles a ciertos estímulos.

En esta parte del trabajo, se ha desarrollado el sistema híbrido formado por bipirámides de Au recubiertas de CTAB como componente plasmónico. La capacidad de las moléculas de JC-1 para intercalarse entre las bicapas de surfactante se ha utilizado como desencadenante para iniciar la formación de este sistema plexcitónico. Tanto las nanopartículas plasmónicas como el pigmento JC-1 se eligieron cuidadosamente para que pudieran interactuar y acoplarse entre sí. Tras establecer esta interacción entre los componentes plasmónicos y excitónicos, se utilizó el pH para inducir la formación de J-agregados con el pigmento JC-1, e iniciar el posterior acoplamiento plexcitónico del sistema. En este proceso, las bicapas de CTAB desempeñan un papel crucial atrapando a las cadenas moleculares y creando un entorno favorable para una fuerte interacción de acoplamiento. Posteriormente, se ha realizado un análisis exhaustivo mediante UV-Vis-NIR y fotoluminiscencia para caracterizar el sistema plexcitónico. A continuación, se han utilizado estudios sistemáticos de dispersión de las resonancias plasmónicas para determinar la fuerza de acoplamiento del sistema. Lo cual implica sintetizar una serie de bipirámides con diferentes resonancias plasmónicas para manipular sistemáticamente esta respuesta plasmónica, de acuerdo con la respuesta de los J-agregados en 600 nm. Mediante la experimentación sistemática, se han estimado los parámetros que confirman que el sistema plexcitónico opera dentro del régimen de acoplamiento fuerte.

Curiosamente, los espectros de fotoluminiscencia de este sistema a temperatura ambiente también muestran modificaciones significativas debidas a la interacción plasmón-excitón, una observación que resulta poco común. En concreto, estos presentan una característica que consiste en un doblete (o división), paralelamente junto con la modificación de los espectros UV-vis. Después de esto, se ha utilizado un modelo teórico para el análisis de los espectros de fotoluminiscencia modificados para confirmar la existencia de la interacción de acoplamiento fuerte. Por último, se ha investigado el efecto del acoplamiento fuerte en la modificación de las propiedades de los J-agregados, en particular, respecto a su fotoestabilidad. Resultando que, mientras que los J-agregados del colorante JC-1 se fotodegradan normalmente en menos de 1 hora, en el sistema fuertemente acoplado observamos una degradación insignificante incluso después de 1 día. Esta fotoestabilidad superior demuestra el potencial de las interacciones de acoplamiento fuerte para modificar las propiedades fotoquímicas y fotofísicas de los sistemas excitónicos.

En el último capítulo de este trabajo, se amplía nuestra investigación a un nuevo

ámbito. Mientras que la mayoría de los sistemas plexcitónicos son estáticos y no pueden modificarse una vez formados, nuestro objetivo era crear un sistema plexcitónico reversible, controlando la agregación del pigmento JC-1. En este capítulo se demuestra con éxito la modulación sensible al pH de la fuerza de acoplamiento entre los componentes plasmónicos y excitónicos en el sistema plexcitónico. Dada la sensibilidad de los J-agregados en nuestro sistema plexcitónico al pH, exploramos la posibilidad de utilizar el pH para cambiar entre un estado totalmente acoplado a otro desacoplado. El JC-1 tiene la capacidad de formar J-agregados a un pH alto, dando lugar a un sistema plexcitónico fuertemente acoplado con bipirámides de Au. Por el contrario, a un pH más bajo, el desensamblaje de los J-agregados trunca el acoplamiento que da lugar a este sistema plexcitónico. En particular, se ha logrado una reversibilidad completa en el ensamblaje y desensamblaje del sistema y la correspondiente formación y destrucción del acoplamiento fuerte en el sistema plexcitónico, respectivamente. Es importante destacar que esta reversibilidad en el ensamblaje y en el acoplamiento fuerte se demostró durante tres ciclos. A lo largo de estos ciclos de reversibilidad, se realizaron estudios detallados mediante espectros de UV-Vis y fotoluminiscencia en función del tiempo. Esto ha permitido analizar la cinética de ensamblaje/desensamblaje y la evaluación de la fuerza de acoplamiento en condiciones de pH variables. Como resultado, se ha observado un lento desacoplamiento al disminuir el pH y un rápido acoplamiento al aumentar el pH, respectivamente. Las cinéticas lentas, durante el desacoplamiento, han permitido la estimación de la fuerza de acoplamiento en cada etapa utilizando un modelo teórico de los osciladores acoplados. Por último, un examen exhaustivo del efecto del pH sobre los componentes plasmónico y excitónico ha permitido estudiar en detalle el mecanismo de reversibilidad. Dado que la influencia del pH sobre la molécula de JC-1 es fundamental para establecer este sistema plexcitónico reversible.

List of Abbreviations

NPs Nanoparticles
NIR Near InfraRed
PSP Propagating Surface Plasmon
LSP Localized Surface Plasmons
Au Gold
NRs Nanorods
BPs Bipyramids
QDs Quantum Dots
CTAB Cethyltrimethyl ammonium bromide
PL Photoluminescence
FLIM Fluorescence Lifetime Imaging Microscopy
SERS Surface-Enhanced Raman Scattering
HR Huang-Rhys
QY Quantum Yield
TRPL Time-resolved Photoluminescence
TAS Transient absorption spectroscopy
LPB Lower Polariton Branch
UPB Upper Polariton Branch

Contents

Chapter 1

Introduction

1.1 Light-matter interaction

Light acts as a central gear for life development on our planet. Its nature has been questioned through the ages to explain its role in the world that we know. The knowledge that we have established about light comes from Aristotle's first theories about light composition and color formation, then the next remarkable contribution was made by Newton who worked on light spectral decomposition. Three hundred years later, Maxwell established a set of equations that supported the prediction of electromagnetic waves and originated the classical electrodynamics field [1, 2]. Beyond this, science research activity was also concentrated on the analysis of light-matter interaction, from bulk materials to molecules and atoms. The study of light-matter interactions holds paramount importance in physics due to its foundational role in understanding essential principles of nature and its wide-ranging implications for various scientific and technological applications. Several key reasons underscore the significance of investigating light-matter interactions, being remarkable the unique window into the fundamental principles of quantum mechanics and electrodynamics that it provides. Studying how photons (a quantum of light) interact with atoms, molecules, and materials allows physicists to unravel the intricacies of the quantum world, contributing to a deeper comprehension of the nature of matter and energy. The study of light-matter interactions played a pivotal role in the development of quantum mechanics. Experiments and theories related to light-matter interactions, such as the photoelectric effect, provided crucial insights that laid the groundwork for the quantum revolution in the early 20th century. The wave-particle duality of light, as described by quantum theory, fundamentally altered our perception of particles and waves. Also, understanding how light interacts with materials is essential for characterizing their properties. Techniques such as spectroscopy, which involves the interaction of matter with different parts of the electromagnetic spectrum, allow scientists to deduce information about the composition, structure, and behavior of

substances. This knowledge is indispensable in fields ranging from chemistry and biology to materials science. The light-matter interactions study, in material science, comprises a myriad of technological applications. In optics and photonics, for example, understanding how light propagates, refracts, and diffracts enables the design of lenses, lasers, and other optical components. In telecommunications, the transmission of information through optical fibers relies on a precise understanding of light behavior. Advances in the study of light-matter interactions are crucial for the burgeoning field of quantum information science. The unique properties of light-matter systems hold promise for developing quantum computers, secure communication protocols, and other quantum technologies from the generation of quantum states of light. We can also notice the importance of this field in biophysics and medical imaging because understanding how light interacts with biological tissues allows for the development of non-invasive imaging techniques. Technologies like fluorescence imaging and photoacoustic imaging rely on the principles of light-matter interactions to visualize structures within living organisms. Also, we can remark on the role of the study of light-matter interactions in environmental and energy applications. In solar energy, for instance, understanding how light is absorbed and converted into electricity by materials is critical for the development of efficient solar cells. Additionally, remote sensing technologies for environmental monitoring depend on the interaction of light with the Earth's atmosphere and surface. In essence, the study of light-matter interactions is foundational to physics and serves as a pillar for advancing our understanding of the natural world, driving technological innovation, and addressing societal challenges across various scientific domains.

1.2 Motivation and objectives

The interaction of light with materials serves not only as an analytical tool but also as a versatile resource for accomplishing various challenging tasks. For instance, light can be used as the source of energy for powering heating applications through the photothermal effect, facilitating electron and energy transfer processes, and even driving useful chemical transformations. Nature itself demonstrates the remarkable ability of utilizing light, as seen in photosynthesis where it splits water and converts carbon dioxide into sugars. Drawing inspiration from nature, scientists have developed molecular, semiconductor, and plasmonic materials to mimic these processes using inorganic components, which often offer greater stability compared to enzymes. However, fully realizing the feats observed in nature with inorganic components remains a challenge. Here, the selective conversion of carbon dioxide into desired products, while inhibiting competing hydrogen evolution reactions is particularly daunting [3]. One promising approach lies in exploiting light-matter strong coupling interaction to fundamentally alter the reactivities of molecules [4,5], where plexcitonic systems—combinations of plasmonic and excitonic components—emerge as a key player. Building upon these insights, this work aims to explore the potential of carefully chosen chemical interactions to form robust plexcitonic systems and study their photophysical properties. Thereby, contributing to the advancement of their possible applicability in photocatalysis.

The primary aim of this thesis is to establish reliable protocols for creating plexcitonic systems, utilizing gold (Au) nanomaterials and emissive molecular chains. These protocols enable the coupling of nanoscale-confined light with carefully chosen excitonic components. Additionally, we endeavor to conduct thorough experiments and analyses to unveil the photophysical and photostability properties of the resulting hybrid states. Through this effort, we seek to uncover fundamental insights that will provide a robust foundation for exploring and ultimately utilizing plexcitonic systems across a wide range of impactful applications.

The thesis begins with a comprehensive introduction to light-matter interaction, followed by a brief review of the general concepts and theory related to individual plasmonic and excitonic interactions. Later, the plasmon-exciton coupling interaction will be summarized, remarking on the theory explaining this phenomenon. In Chapter 2, the focus shifts to the excitonic component of plexcitonic nanohybrids, specifically, the molecular chains known as J-aggregates. This chapter includes a thorough characterization of the photophysical properties of two distinct J-aggregates, along with an estimation of their exciton coherence lengths. Then, Chapters 3 and 4 detail the formation of hybrid systems incorporating both types of J-aggregates and gold nanoparticles (NPs) and showcasing two independent strategies for forming a plexcitonic system. Here, detailed studies were carried out to estimate the strength of coupling between the plasmon and excitonic components. Moreover, we studied the impact of coupling on the photophysical properties of the J-aggregates. To close, Chapter 5 presents a first demonstration of reversible plexcitonic systems under chemical stimulus (pH) showcasing a new approach to the development of dynamic plexcitonic systems under a strong coupling regime.

1.3 Plasmonic nanoparticles

This section is devoted to the review of the key attributes of gold nanoparticles. An understanding of the basic optical properties is important for several reasons. The most important one is that, spectroscopic measurements are often the simplest method for monitoring surface processes on metal nanocrystals and assessing the colloidal stability of nanoparticles. For example, in the later parts of this thesis, we shall discuss the formation of hybrid plexcitonic systems based on AuNPs (see Chapters 3 and 4) and their long-term stability under the action of external stimulus. Taking advantage of spectroscopic measurements, one can easily assess and draw conclusions on nanoparticles' state by monitoring their optical response.

In general, the field of plasmonics is focused on the analysis of the electromagnetic field confinement in dimensions similar to the wavelength or smaller. The triggered interactions between electromagnetic fields and the conduction electrons, present in metallic interfaces or nanostructures, give rise to collective electronic oscillations called plasmons. The plasmons are classified according to their origin [6]. Here we can distinguish between two fundamental plasmonic excitations: Propagating Surface Plasmon (PSP) and Localized Surface Plasmons (LSP). PSP originates in the interface of a dielectric and conductor material. They propagate over the

surface as electromagnetic excitations and decay evanescently with decay lengths on the order of 200 nm (see Figure 1.1(**a**)). On the other hand, the Localized Surface Plasmons (LSP) arise from the electronic oscillations that take place when an electromagnetic field interacts with metallic nanoparticles with a size smaller than the incident wavelength [6, 7] (Figure 1.1(**b**)). This phenomenon occurs in a variety of metals, but the most commonly used are copper, silver, and Au since they are chemically more stable and show resonances in the visible spectral range. In simple terms, the formation of a localized surface plasmon can be seen as follows: the electric field of the incoming radiation induces the formation of a dipole in the nanoparticle, and there is a restoring force that tries to compensate it so that a unique resonance frequency matches this electron oscillation within the nanoparticle (see Figure 1.1(**b**)). [7] This resonance frequency can be directly observed by UV-Vis-NIR spectroscopy and shows a characteristic plasmon band.

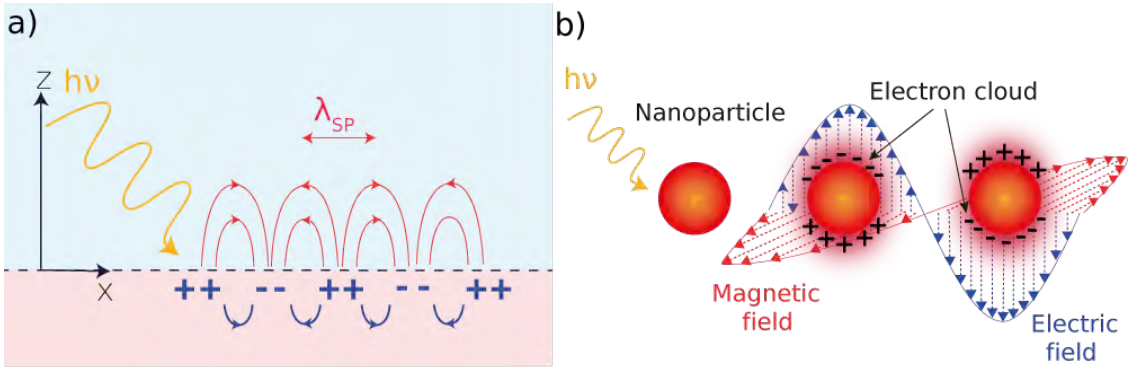

Figure 1.1: Fundamental plasmonic excitations. (**a**) Propagating surface plasmon originated at the interface of a dielectric and a metallic material. (**b**) Localized surface plasmon derived from the light interaction with a metallic nanoparticle.

Controlling the size, shape, and composition of plasmonic nanoparticles is essential for tailoring their plasmonic responses, offering opportunities for designing materials with customized optical characteristics [6]. For the purpose of the present thesis, we shall focus on metallic nanoparticles that exhibit plasmonic response, in particular gold nanostructures with dimensions below 200 nm. AuNPs possess certain characteristics that make them a unique nanomaterial with a performance in the visible and near-infrared (NIR) spectral ranges and also because of their chemical stability under ambient conditions [8].

The resonance frequency in gold nanoparticles depends on the shape and the nature of the surrounding medium, among others [7, 9, 10]. For particles, such as rod-like or bipyramids, the resonance wavelength depends on the orientation of the electric field relative to the particle, and thus, oscillations either along (longitudinal) or across (transversal) the rod or bipyramids are possible (see Figure 1.2 **(a)**) [11–13]. Because of the dimensionality of anisotropic shapes, the frequencies associated with the various resonance modes can be quite different and, thus the optical properties can be largely affected (see Figure 1.2**(b)**, **(c)**) [7, 10, 14].

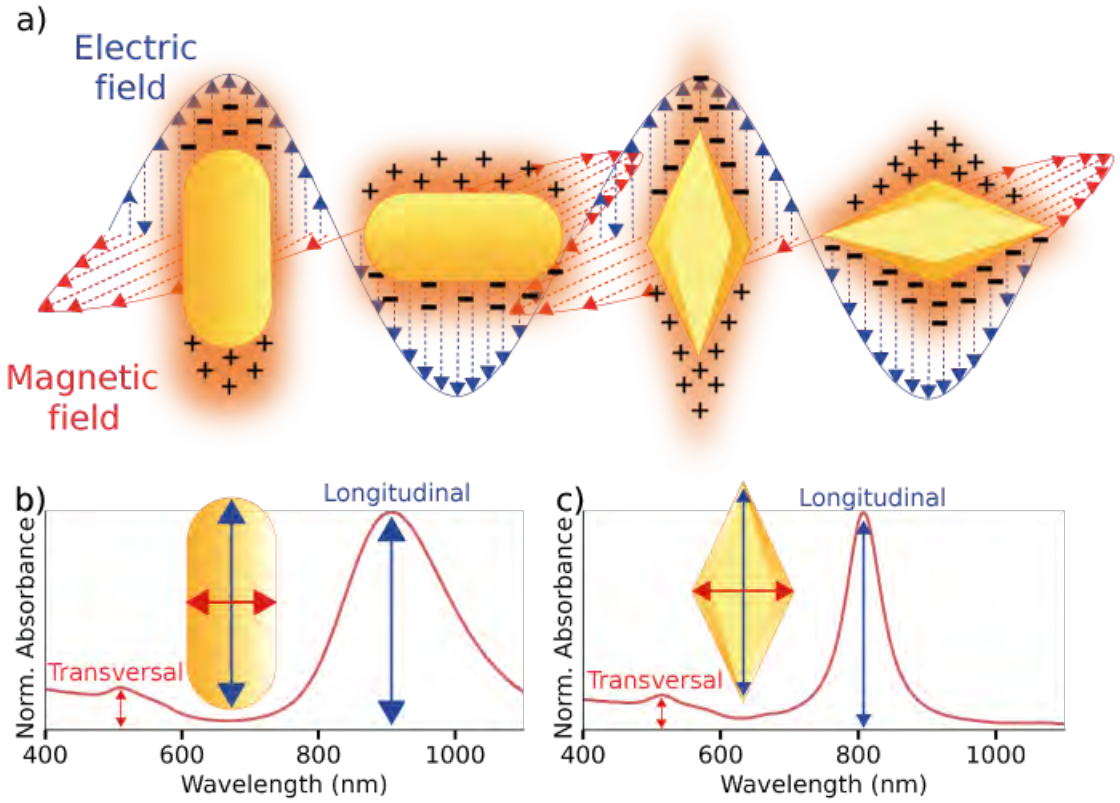

Figure 1.2: Plasmonic for different NPs geometry: nanorods and bipyramids. **(a)** Schema of the electromagnetic field interaction with the electrons of the plasmonic NPs surface (NRs and BPs). This interaction originates the electrons' collective oscillations known as plasmons. **(b)** UV-vis-NIR spectral signature of colloidal NRs, the features present in the spectrum come from the electronic oscillations along and across the nanostructure (inset image) that are labeled as 'longitudinal' and 'transversal' responses. **(c)** In the case of BPs the presence of sharp tips and edges (inset image) results in a narrower longitudinal plasmonic response in the UV-vis-NIR spectra (red line).

A detailed inspection of LSPR in AuNRs and BPs shows that the latter exhibit a much narrower longitudinal surface plasmon band (red line in Figures 1.2**(b)** and **(c)**). That is, while for typical AuNRs the linewidth of LSPR is around 150-200 nm, for AuBPs it can be as narrow as 70 nm. The reason behind such a well-defined plasmon band is the presence of narrow tips (small volume) that can strongly concentrate the electric field [15,16], the intense electric field is generated at their edges and tips. This anisotropy contributes to heightened local field enhancement, surpassing those observed in other morphologies, resulting in a notably narrow extinction feature. Liu et al. [17] have extensively explored the unique properties of AuBPs, emphasizing their unique crystal structure and the manifestation of a distinctive narrow and intense localized longitudinal LSPR response in comparison to gold nanorods. Overall, the narrow plasmon band has important implications, especially in the context of the formation of hybrid systems with quantum emitters, such as J-aggregates, which exhibit narrow spectral emission (vide infra). Therefore, it is expected that the Au nanoparticles of bipyramidal shape are a better choice when designing hybrid

plexcitonic nanosystems.

1.3.1 Origin of plasmon resonances

The surface plasmon resonance of small spherical particles of a radius R can be predicted by Mie theory, through expressions for the extinction cross-section C_{ext}. For small particles with a complex dielectric function, $\varepsilon = \varepsilon' + i\varepsilon''$, embedded in a medium of dielectric constant ε_m, C_{ext} can be expressed as:

$$C_{ext} = \frac{24\pi^2 R^3 \varepsilon_m^{3/2}}{\lambda} \frac{\varepsilon''}{(\varepsilon' + 2\varepsilon_m) + \varepsilon''^2} \tag{1.1}$$

Note that C_{ext} scales as R^3, while the number density decreases as R^3 for a given amount of material. The origin of color changes displayed by small particles lies in the denominator of Equation 1.1, which indicates the existence of an absorption band when

$$\varepsilon' = -2\varepsilon_m \tag{1.2}$$

In a small metal particle, the dipole created by the electric field of light induces a surface polarization charge, acting as a restoring force for the free electrons. The net result is that, when the condition from Equation 1.2 is fulfilled, the long wavelength absorption by the bulk metal is condensed into a single surface plasmon band.

The situation becomes more complex when taking into consideration non-spherical NPs. Considering gold nanorods, the orientation with respect to the oscillating electric field must be taken into account (Gans approximation) to calculate the spectra of these NPs:

$$C_{ext} = \frac{8\pi^2 R^3 \varepsilon_m^{3/2}}{3\lambda} \sum_j \frac{\left(1/P_j^2\right) \varepsilon''}{\left(\varepsilon' + \frac{1-P_j}{P_j}\right)^2 + \varepsilon''^2} \tag{1.3}$$

where P_j represents the depolarization factors for the NR axes ($a > b = c$), defined as

$$P_a = \frac{1-r^2}{r^2}\left[\frac{1}{2r}\ln\left(\frac{1+r}{1-r}\right) - 1\right] \; ; \; P_b = P_c = \frac{1-P_a}{2} \tag{1.4}$$

and the parameter r is related to the aspect ratio:

$$r = \sqrt{1 - \left(\frac{b}{a}\right)^2} \tag{1.5}$$

Gans predicted this behavior for very small ellipsoids. The surface plasmon mode would split into two distinct modes (transversal and longitudinal), which indeed one

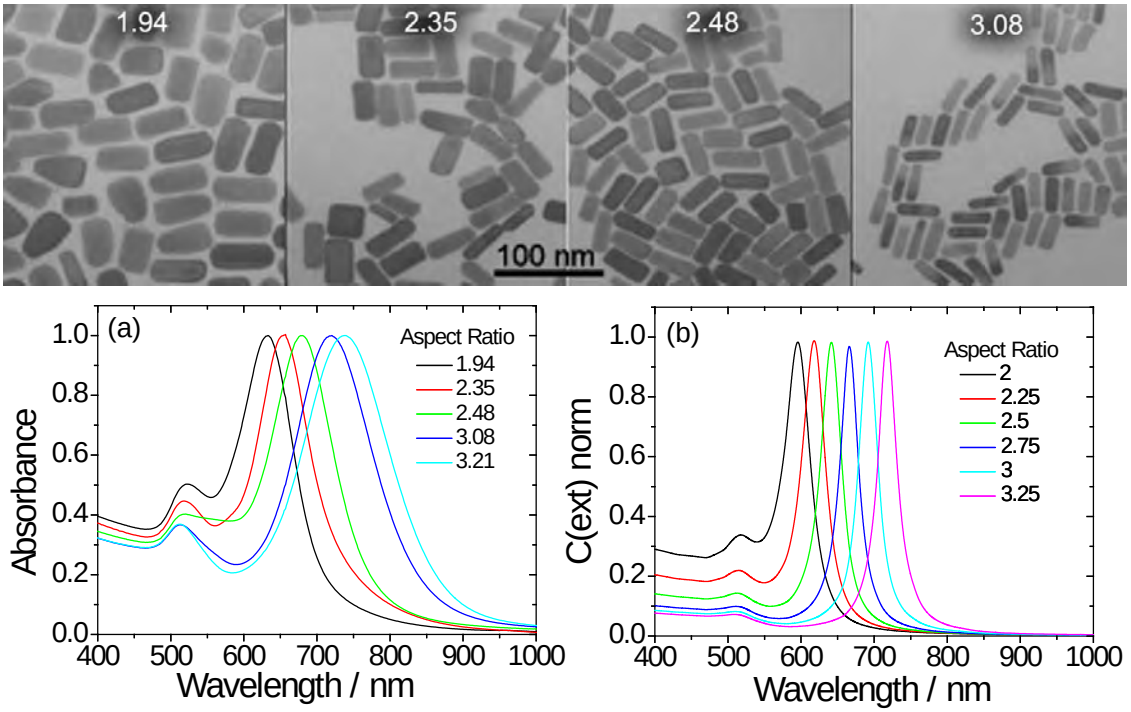

Figure 1.3: TEM micrographs of gold nanorods with variety of aspect ratio. **(a)** UV-Vis spectra of gold nanorods form TEM images. Note that increasing aspect ratio position of longitudinal plasmon band red-shift. **(b)** Calculated UV-Vis spectra of gold nanorods based on the ellipsoidal model, shifting of plasmon band as a function of aspect ratio is with good agreement of experimental spectra. Reproduced from [18, 19].

can observe by UV-Vis-NIR spectroscopy (Figure 1.3 **(b)**). This is a consequence of the surface curvature, which determines classically the restoring force or depolarization field that acts on the confined conduction electron population.

According to Equation 1.5, the ellipsoid geometry can be characterized by the aspect ratio (between the length and the width). Small changes in the aspect ratio of experimental AuNRs lead to drastic changes in the position of the longitudinal plasmon band (Figure 1.3 **(a)**. As clearly shown, by increasing the aspect ratio from 1.94 to 3.08, the maximum position of the longitudinal plasmon band shifts to a higher wavelength. That variation of optical response can be confirmed by TEM characterization, which shows changes in the aspect ratio of corresponding samples. Of course, similar behavior holds also for gold bipyramids as will be shown in Chapter 3. Moreover, obtaining exact modeling of optical properties in Au BPs requires numerical methods since the ellipsoid geometry is insufficient to approximate tiny features such as tip curvature.

1.3.2 Chemical Synthesis of gold nanoparticles

In the present thesis, the gold nanoparticles are a central component of new hybrid plexcitonic systems. Although the mechanistic understanding of the growth process in these nanoparticles is not critical to our aim, it is convenient to mention briefly the main chemical mechanisms behind the growth of metal nanocrystals.

Wet chemical synthesis of gold nanoparticles is usually classified according to two mechanisms: nucleation/growth, and seeded-growth (Figure 1.4).

Figure 1.4: Main mechanisms for the synthesis of AuNPs. In the nucleation and growth mechanism, a strong reducing agent reduces metal ions followed by growth into nanoparticles. In the seeded-growth process, the reduction of metal ions takes place exclusively on the surface of preformed seeds to produce particles of the desired shape and size. Reproduced from [20]

In the first approach, a strong reducing agent reduces metal salt to produce NPs covered with organic molecules (stabilizing agents) on their surface, thus preventing aggregation. [20] The size of nanoparticles can be controlled by tuning the molar ratio between the stabilizing agent and the metal precursor.

The seeded-growth model involves nucleation and growth stages separated in time. The seeds are usually obtained through the nucleation and growth process and later are used in overgrowth to obtain desired nanoparticles. The main advantage of this process is that its autocatalytic nature allows controlling the number of final NPs in the solution, which simply depends on the amount of added seeds. Another advantage of this process is its slow reduction kinetic that allows for chemical inhibition of given crystal facets during growth, resulting in the obtention of non-spherical NPs, such as AuNRs or BPs.

As mentioned above, the gold bipyramids are expected to exhibit narrower plasmon bands as compared to gold nanorods, making them more suitable for plexcitonic constructs. Thus, from now we will center mainly on the synthesis of BPs, which will be briefly discussed.

The BPs are obtained through the seeded-growth method in the presence of cationic surfactant (CTAB), silver nitrate, hydrochloric acid, and preformed gold seeds. [21] Studies have shown that the seeds determine the final quality of bipyramids. The seeds are obtained through the addition of a strong reducing agent to the solution containing gold salt in the presence of surfactant to produce small clusters (1-2 nm in diameter) stabilized by a bilayer of cationic surfactant. [22] Due to the small size of seeds, no surface plasmon is observed, thus their absorption spectra are characterized by a maximum in the UV range, which originates from inter-band transitions (Figure 1.5 - brown) [23]. In the next step, the solution of seeds is subjected to thermal treatment at 80 °C for 90 minutes. [21] This process is accompanied by a gradual color change of the solution from brown to red, suggesting the formation of larger NPs, as they exhibit LSPR (Figure 1.5 - red). These seeds are 6 nm in diameter, featuring surface faceting and defects, the so-called twin planes. [12, 21, 22]

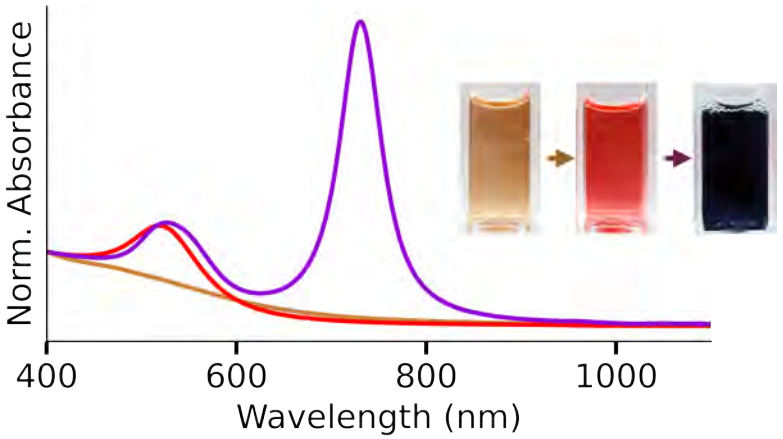

Figure 1.5: Optical properties of gold bipyramids and seeds nanoparticles used to synthesize them. The absorbance spectra of as-prepared gold seeds (brown line) and after thermal treatment (red line), indicate the emergence of a plasmon band located at 505 nm. The final gold bipyramids exhibit two plasmon bands (violet). All spectra are normalized at 400 nm for better comparison. Inset image: visual inspection of sample colors at each stage of the synthesis of gold bipyramids.

The formation of bipyramid takes place during the growth stage, where the seeds act as a catalyst. That is, gold seeds catalyze the oxidation of the reducing agent (e.g., ascorbic acid) and serve as a reactive spot for the exclusive reduction of metal precursor on their surface. In general, the process is slow (2-3 hours), leading to the formation of gold bipyramids that feature two characteristic plasmon bands (Figure 1.5 - violet). The control of the aspect ratio in AuBPs is achieved by changing the concentration of the seeds. That is, with the decrease of Auseed the aspect ratio increases as reflected in the progressive redshift in the longitudinal LSPR. The width of the BPs remains constant despite the length increase induced by higher seed concentrations, resulting in an unaltered wavelength for the transversal plasmon mode.

To close this section, the current state-of-the-art in nanochemistry offers experimental tools to modulate gold nanoparticles' dimensions and associated optical properties. These tools, however, are often insufficient to adapt the plasmonic nanoparticles in a way to achieve the desired plexcitonic system, especially if one is limited to commercially available molecular dyes that are of specific chemical composition and optical features. To overcome such a limitation, one needs often explore post-synthetic processing of as-prepared nanoparticles including oxidative etching to further tune the position of plasmon band (see Appendix 5.7) or ligand exchange to make surface composition compatible with molecular quantum emitters (see Chapter 3).

1.4 Quantum emitters

Quantum emitters (QEs) are described as nanostructures with the capability of emitting light, or photons, one by one. An incident photon having the same energy as the discrete internal electronic energy level difference can originate resonant light-matter interactions in these materials. One of the QEs' main characteristics is the single-photon level control, meaning that their blinking can be manipulated [24].

The QEs can be categorized into several groups, depending on the material or morphology of the materials used (Figure 1.6). Typical examples are organic dye molecules **(a)**, semiconductor quantum dots (QDs) and other nanostructures **(b)**, and impurity centers in wide-bandgap semiconductors and dielectrics **(c)** [25].

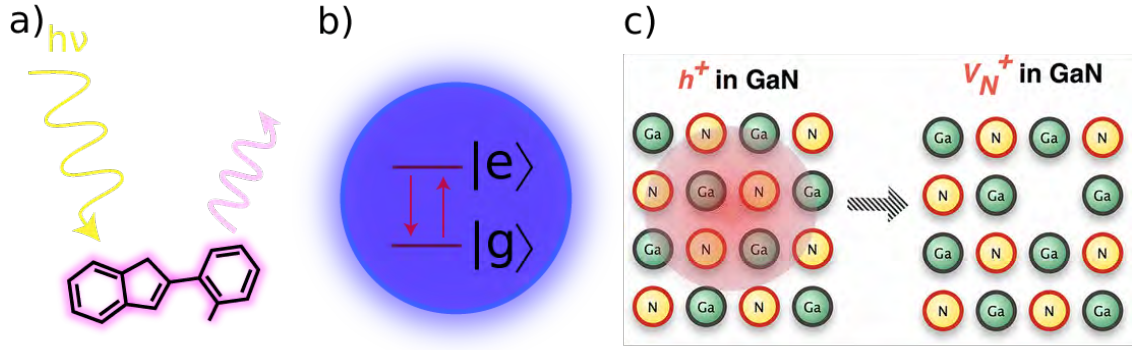

Figure 1.6: Quantum emitters. (**a**) Fluorescent organic molecule, (**b**) quantum dot, and (**c**) gallium nitride doped wide band semiconductor (reproduced from Walsh et al. [26]).

Semiconductor QDs possess a high photoluminescence (PL) quantum yield and their response can be tuned by controlling the size or composition. On the other hand, in wide-band gap semiconductors, it is possible to manipulate the crystal lattice to obtain vacancy centers and rising luminescence response from the material [26, 27].

1.4.1 Fluorescent molecules

Luminescence phenomena take place when a material emits light from electronically excited states. We can distinguish two luminescence categories according to the excited state nature: fluorescence (from excited single states) and phosphorescence (from triplet excited states) [28].

Fluorescent molecules are a diverse class of compounds that exhibit light emission after having absorbed light or other electromagnetic radiation [28]. The fluorescence process involves three key steps: the absorption of a photon by the fluorescent molecule, followed by internal conversion to the lowest vibrational energy level of the excited electronic state, and the emission of a photon at a longer wavelength than the absorbed light. [25]

In biological imaging, fluorescent molecules play a crucial role in visualizing cellular structures and processes. For example, the green fluorescent protein from

jellyfish is widely used as a marker for gene expression and protein localization in living cells. [29] In chemistry and materials science, fluorescent molecules are used as probes to study the behavior of molecules and materials at the molecular level. In medical diagnostics, fluorescent molecules are used as contrast agents in imaging techniques such as fluorescence microscopy and in vivo fluorescence imaging. Overall, fluorescent molecules are versatile tools that have revolutionized our ability to study and manipulate biological systems and materials at the molecular level [30].

1.4.1.1 Cyanines dyes

Within the field of fluorescent molecules, cyanine dyes constitute a versatile class of organic molecules widely employed in various scientific and technological applications, owing to their unique optical properties and chemical flexibility [31]. These dyes are characterized by a polymethine backbone, consisting of a series of conjugated double bonds, which imparts them with an extended π-electron system (see Figure 1.7) [32, 33]. This structural feature contributes to their remarkable absorption and emission properties across the visible and near-infrared regions of the electromagnetic spectrum. Cyanine dyes can exist in different forms, including monomeric, dimeric, and aggregated states, each influencing their spectroscopic behavior and potential applications [31, 34].

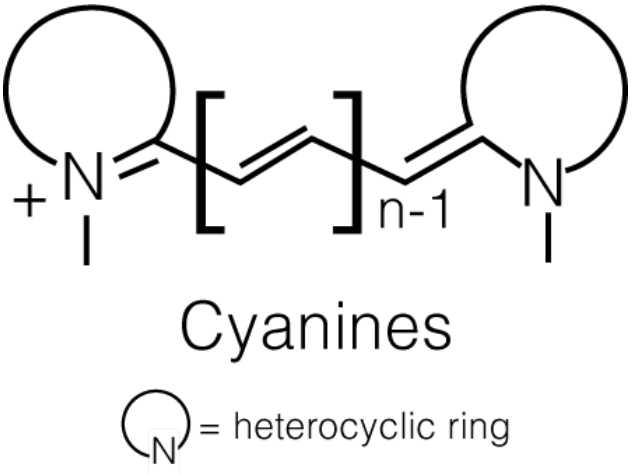

Figure 1.7: Schematic representation of the general chemical structure of cyanine dyes [35].

The tunable nature of cyanine dyes makes them valuable tools in fluorescence imaging and labeling applications [31]. Their absorption and emission wavelengths can be easily adjusted by modifying the length of the polymethine chain or by introducing substituents on the molecule [36]. This tunability allows researchers to select specific cyanine dyes tailored to their experimental needs, such as minimizing spectral overlap in multicolor imaging or optimizing compatibility with certain biological samples. Moreover, the high molar extinction coefficients of cyanine dyes make them particularly useful for enhancing signal brightness in fluorescence-based assays and imaging techniques [37, 38].

In addition to their role in fluorescence applications, cyanine dyes find utility in the field of biophysics and biochemistry. Their propensity to interact with biomolecules, such as proteins and nucleic acids, has led to their use as probes for studying molecular interactions, conformational changes, and dynamic processes within biological systems. Cyanine dyes have also been employed in the development of contrast agents for imaging modalities like photoacoustic imaging, where their strong absorbance in the near-infrared region facilitates deeper tissue penetration [39].

Beyond biological applications, cyanine dyes have been explored in the realm of materials science, specifically in the fabrication of optoelectronic devices. Their favorable photophysical properties, such as high quantum yields and photostability, make them suitable candidates for use in organic light-emitting diodes (OLEDs) and dye-sensitized solar cells [31, 40]. As research in the field of molecular engineering continues, cyanine dyes remain an intriguing area of exploration for scientists seeking to harness their unique properties for diverse technological advancements.

For the purpose of the present work, two dyes were selected, namely a cyanine dye, JC-1 (5,5',6,6'-Tetrachloro-1,1',3,3'-tetraethyl-imidacarbocyanine iodide, 5,5',6,6'-Tetrachloro-1,1',3,3'-tetraethylbenzimidazolocarbocyanine iodide) and S2275 (5-Chloro-2-[3-[5-chloro-3-(4- sulfobutyl)-3H-benzothiazol-2-ylidene]-propenyl]-3-(4-sulfobutyl)-benzothiazol-3-ium hydroxide) (Figure 1.8). These molecules exhibit characteristic absorption and emission in the visible and near-infrared spectral range and are widely used in live science as biomarkers.

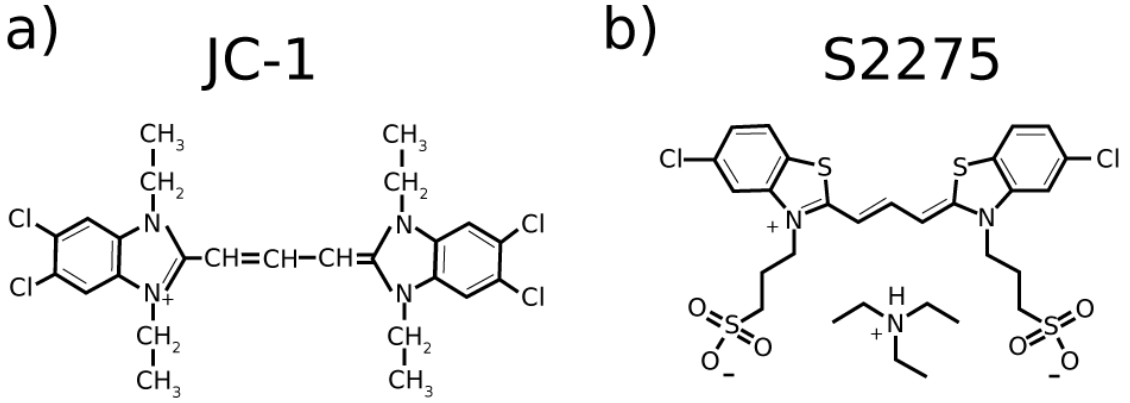

Figure 1.8: Chemical structure of cyanine dyes used in the present work.

One of the notable features of JC-1 is its ratiometric behavior, which allows researchers to obtain quantitative information about mitochondrial membrane potential. By measuring the ratio of red to green fluorescence, scientists can infer the status of the mitochondrial membrane potential in a given cell or tissue [41]. This characteristic makes JC-1 particularly advantageous for live-cell imaging and flow cytometry applications, providing dynamic insights into mitochondrial function and allowing the assessment of conditions such as apoptosis, drug-induced toxicity, or other cellular stress responses. The versatility of JC-1 has positioned it as a widely employed fluorescent probe in diverse biological research contexts, contributing to

a deeper understanding of cellular processes and pathologies associated with mitochondrial dysfunction.

S2275 dye is a synthetic fluorophore widely used in biological and chemical research [42–44], and is soluble due to the presence of triethylammonium salt, facilitating its use in aqueous biological environments. Its excitation and emission wavelengths in the NIR region minimize interference from background autofluorescence and light scattering, allowing for improved sensitivity and resolution in fluorescence imaging.

1.4.1.2 J-aggregates

J-aggregates are self-assembled molecular aggregates with unique optical properties that arise from the strong coupling between individual chromophores [45]. This phenomenon is often observed in certain classes of dyes, such as cyanine dyes, when assembled in a specific form, typically in a one-dimensional arrangement [46]. The most notable property of J-aggregates is their intense absorption (J-band), which is significantly red-shifted compared to the monomeric form of the dye (see Figure 1.9). This red shift arises from the strong electronic coupling between the chromophores in the aggregate, leading to coherence (or delocalization) of excitons and a lower energy gap between the ground and excited states. [47, 48]

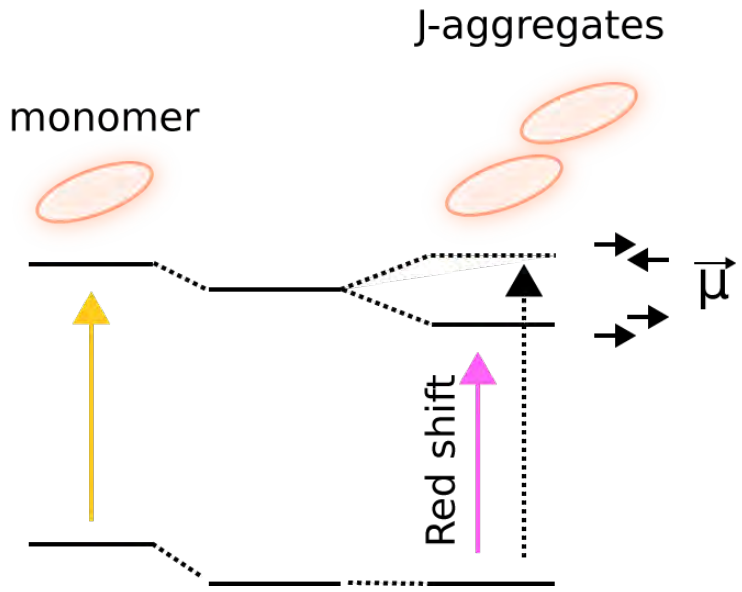

Figure 1.9: Schematic representation of monomer and J-aggregates, together with their corresponding energy levels.

J-aggregates usually present a small or unexistent Stokes shift, defined as the difference between the absorbance and emission maxima of a chromophore, coming from the energy losses in the system [28]. The small Stokes shift in J-aggregates can be explained by the high degree of self-organization present in the J-aggregates' molecular quantum transitions. Furthermore, this phenomenon arises from the nuclear environment reorganization and the excited electronic state spontaneous loos-

ening [49]. Since J-aggregates constitute molecular building blocks their formation is often conditioned by the way these building blocks interact with the environment. That is, being a supra-molecular system, J-aggregates form under conditions that compromise the full solvation of molecular dyes, leading to progressive aggregation. There are many experimental factors controlling the formation of J-aggregates including the concentration of the dye, the type of solvent, temperature, and ionic strength.

J-aggregates gain value when combined with other systems. For example, in the context of the present Thesis, it will be shown that J-aggregates can reach a strong coupling regime when combined with plasmonic nanoantennas, as will be discussed in detail in Section 1.6.

1.5 Frenkel Excitons, J-aggregates and Coherence Length in Molecular Chains

An exciton is defined as the result of an electron and a hole pair bound, this bonding originates an uncharged electronic excitation [50, 51]. Since it has no electric charge they are not involved in electrical conduction, but they are responsible for the energy transport processes through their mobility [51]. The excitons are related to many optical properties of solids, such as absorption of light and luminescence. They are classified according to the chemical bonding:

- Frankel excitons present in organic crystals due to the Van der Waals intermolecular bonding
- Warnier-Mott excitons in inorganic semiconductors with ionic or covalent bonding [51].

In the context of the present Thesis, we will focus on Frenkel excitons to describe the optical properties of J-aggregates.

1.5.1 Frenkel Excitons

Frenkel excitons are fundamental quasiparticles that play a pivotal role in understanding the optical and electronic properties of molecular crystals and organic semiconductors [52]. Named after the physicist Yakov Frenkel, who first introduced the concept in the early 20th century, Frenkel excitons arise from the collective electronic excitation of tightly bound electron-hole pairs within a single molecule [53]. Unlike Wannier-Mott excitons, which involve charge carriers spatially separated across neighboring molecules, Frenkel excitons are localized on a single molecular unit. This localization is a consequence of the strong electron-electron and electron-nucleus interactions within the molecule, leading to a distinct set of optical and transport properties that differentiate Frenkel excitons from other excitonic species [50]. The Frenkel excitons are characterized by the short separation between electron and hole

because they occur in the same molecule so they present a high binding energy, about 1 eV [51].

In the realm of molecular excitations, typically the lowest singlet excited state within a molecule yields authentic Frenkel excitons, whereas higher excited states often exhibit adequate charge overlap, permitting a non-negligible separation between the electron and hole. Despite the inherent confinement of the electron and hole within the same molecule in a Frenkel exciton, they can travel together through the crystal lattice, and the electrostatic interactions between electrons residing on distinct molecules establish a center of mass for the motion. The main contribution comes from the interactions between the transition dipoles associated with individual molecular transitions. Consequently, a long-range $(1/r^3)$ excitation transfer interaction between molecules ensues and raises the establishment of an exciton band [50].

In microscopic theory, Frenkel excitons can be described through a two-level molecule Hamiltonian, enclosing all electrons' kinetic energy and nuclei, and the Coulombic coupling coming from these particles. Also, it is required to assume known adiabatic eigenstates and a nondegenerate ground state ($|g\rangle$). We will describe just vibrationally relaxed electronic states, avoiding in this work the analysis of vibronic states. The contributions to the molecule's linear optical response come from all possible transitions from the ground state. Then, the Hamiltonian describing the basic properties of Frankel exciton can be written as follows:

$$\widehat{H}_{mol} = \hbar\omega_g|g\rangle\langle g| + \hbar\omega_e|e\rangle\langle e| \tag{1.6}$$

Where ω_g is the frequency of the ground state, and ω_e is the frequency of the excited state $|e\rangle$ which dominates the others. From this, the molecular dipole operator $\widehat{\mu}$ [50] can be written as:

$$\widehat{\mu} = \mu(|e\rangle\langle g| + |g\rangle\langle e|) + \mu_g|g\rangle\langle g| + \mu_e|e\rangle\langle e| \tag{1.7}$$

Here μ is used to refer to the states transition dipole, and the states-related permanent dipoles are μ_g and μ_e.

In recent years, advancements in experimental techniques, such as ultrafast spectroscopy and high-resolution microscopy, have provided unprecedented insights into the dynamics and spatial distribution of Frenkel excitons [48, 54, 55]. Additionally, theoretical models and simulations have been developed to elucidate the complex interplay between electronic and vibrational states, offering a deeper understanding of the underlying physics. This comprehensive investigation of Frenkel excitons is driving progress in the design and optimization of organic materials for a new generation of optoelectronic devices with enhanced performance and efficiency [56]. As researchers continue to unravel the intricacies of Frenkel excitons, their potential impact on technology and fundamental science becomes increasingly apparent.

1.5.2 Exciton Coherence Length

Exciton coherence length is a crucial parameter in the study of excitonic systems, representing the spatial extent over which excitons maintain phase coherence [56]. Excitons, being bound electron-hole pairs with quantum-mechanical characteristics, exhibit both particle and wave-like behaviors [50]. The coherence length tells about the number of molecules of an aggregate over which the exciton wave function is coherent, the dipole momentum, oscillator strength, and the radiative lifetime of the exciton transition. The coherence length also has some implications for the nature of long-distance exciton migration and transport - whether coherent or incoherent [57]. The coherence length of excitons is influenced by various factors, including material properties, temperature, and external perturbations [58]. Manipulating the coherence length can be achieved through engineering the electronic and structural properties of the material. For instance, controlling the degree of disorder, crystal structure, or incorporating specific molecular configurations can impact exciton coherence [59,60]. The ability to extend or limit exciton coherence length allows researchers to tailor the material for specific applications, optimizing charge transport in solar cells or enhancing the efficiency of exciton transfer in organic electronic devices. As exciton coherence continues to be a focal point in research, advancements in material design and understanding of excitonic dynamics are poised to contribute significantly to the development of next-generation optoelectronic technologies. A more detailed discussion on exciton coherence length is discussed in Chapter 2.

1.6 Plexcitonic Systems

Plexcitonic systems are hybrid structures that involve the coupling of plasmonic excitations in metallic nanostructures with excitonic transitions in semiconductor quantum dots or organic molecules. This coupling leads to the formation of new electronic hybrid states known as plexcitons, which exhibit unique optical properties. In this field, several systems have been reported and analyzed like the interaction of an excitonic layer (organic molecules or semiconductor) conjoined with a metallic film, either the surface plasmonic response from nanostructures or a lithographically patterned array interacting with semiconductor or molecular excitons [61,62].

The interaction between a plasmonic nanoparticle and a molecular excitonic system is presented in Figure 1.10, also describing schematically the formation of such a hybrid state with a typical doublet feature as a result of the strong coupling.

Since quantum emitters like molecules and quantum dots possess the property of supporting an exciton formation upon a photon absorption and exhibit a single photon emission [63], they are presented as a perfect candidate to form plexcitonic systems. From these quantum emitters, quantum dots and J-aggregated molecules are mainly used to couple to plasmonic nanostructures due to their narrow emission bands. The plasmonic excitations in the metallic nanostructures can enhance the absorption and emission properties of the excitonic transitions [61]. Also, it has been shown that plexcitonics systems exhibit improved stability under environmental stressors such as elevated temperature, a wide range of pH, or intense light [63].

The physical properties of plexcitonic systems, such as their absorption and emission spectra, can be tuned by adjusting the size, shape, and material composition of the metallic nanostructures and the semiconductor or organic molecules.

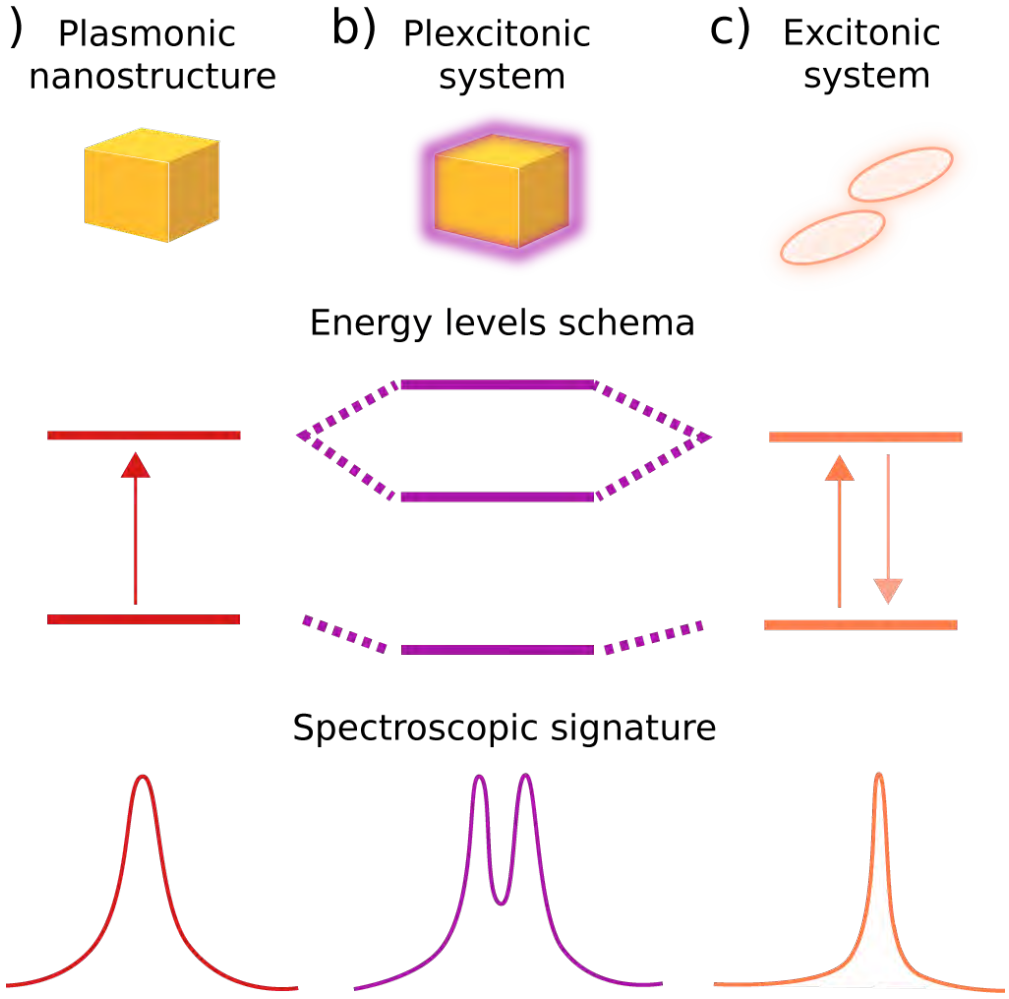

Figure 1.10: Plexcitonic system and its components. (**a**) Plasmonic nanostructure: gold nanocube, plasmon energy diagram, and the characteristic LSPR UV-vis-NIR signature (from top to bottom). (**b**) The hybrid system originated from the plasmon and exciton interaction, the energy level diagram showing the formation of two hybrid states, and the associated spectroscopic signature showing a doublet feature. (**c**) The molecular excitonic system molecular structure, the associated energy diagram where it is considered a two-level system, and its spectroscopic signature.

Importantly, the nature of the interaction between plasmons and excitons in a hybrid system can be classified according to the strength of this interplay, namely weak and strong coupling depending on the energy exchange rate (Figure 1.11) [64]. The weak coupling regime is characterized by an energy exchange rate slower than each system component's dissipation rates. This leads to the formation of a hybrid system, that can present enhanced or suppressed optical response coming from an altered exciton radiation efficiency (Purcell effect) [64]. In this case, both components preserve their original properties [65, 66]. However, when the energy

exchange rate is faster than the photon leakage rate and the non-radiative losses of the emitter, the system's interaction is in the strong coupling [63, 67].

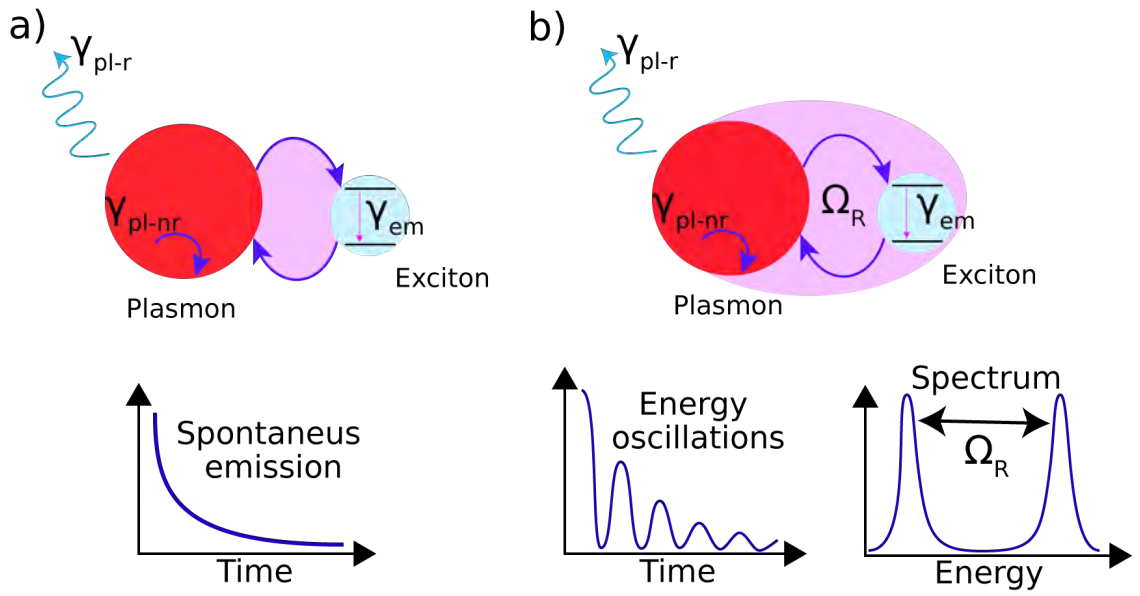

Figure 1.11: Plexcitonic system of different coupling regimes. (**a**) Weak coupling: the energy transfer rate is smaller than the dissipation rates (γ_{pl-r} for the radiative decay rate and γ_{pl-nr} for the non-radiative decay rate of the plasmonic system, and γ_{em} for the decay rate of the excitonic system). (**b**) Strong coupling: the energy transfer rate is higher than the dissipation rates (γ_{pl-r}, γ_{pl-nr} and γ_{em}). This phenomenon originates the Rabi oscillations at the Rabi-energy Ω_R.

In the present work, an emphasis is put on developing a plexcitonic system exhibiting a strong coupling regime. These types of systems are desirable for a variety of applications including sensors or light-harvesting materials. Thus, in the following paragraphs, we will discuss the characteristics of a strong coupling regime.

In general terms, the strong coupling light-matter regime raises the modification of the energy levels related to the resulting emission linked to the local optical environment levels [68]. A widely used model to describe the strong coupling between an emitter and plasmonic metal nanoparticles consists of taking a two-level single emitter and a single resonant mode from the NPs. This can be depicted by the Jaynes-Cummings Hamiltonian, taking quantized plasmon field in terms of boson operators ($\widehat{a}$, $\widehat{a}^{\dagger}$) [67].

$$\widehat{H} = \hbar\omega_{SP}\widehat{a}^{\dagger}\widehat{a} + \hbar\omega_e x\widehat{\sigma}^{\dagger}\widehat{\sigma} + \hbar g(\widehat{a}^{\dagger}\widehat{\sigma} + \widehat{\sigma}^{\dagger}\widehat{a}) \tag{1.8}$$

In this equation, it is taken into account the two-level system Pauli raising operator with $\widehat{\sigma}$, the plasmon resonance frequency as ω_{SP}, the transition frequency of the emitter as ω_{em}, the system coupling strength g. Within this model, the damping and decoherence are both neglected. [67] The case of multiple emitters coupling to a plasmonic nanostructure is covered in the Tavis-Cummings model [69].

However, since the quantum model solution requires computational calculations this problem can be simplified by applying the classical theory to describe our system as a coupled oscillator. If the Maxwell-Bloch equations are applied the results of the semiclassical model are considered close enough to the quantum ones [67,68]. Then, solving the coupled-oscillator equations we obtain the total extinction cross-section of the coupled system [70]:

$$C_{ext}(\omega) \propto \omega Im\left(\frac{(\omega_{exc}^2 - \omega^2 - i\omega\Gamma_{exc})}{(\omega^2 - \omega_{SP}^2 + i\omega\Gamma_{SP})(\omega^2 - \omega_{exc}^2 + i\omega\Gamma_{exc}) - \omega^2 g^2}\right) \tag{1.9}$$

Where the plasmon decay rate Γ_{SP}, and the emitter decay rate Γ_{exc} are present. This cross-section includes both responses from the system: absorption and scattering.

Analyzing the coupling strength in the plexcitonic systems requires estimating the Rabi-splitting energy (Ω_R). This parameter defines the separation between the hybridized plexcitonic resonances originated by the strong coupling interaction. The Rabi-splitting energy value can be estimated by fitting the dispersion curves coming from the upper and lower branches of the formed hybrid states, using equation 1.10 [64].

$$E_{\pm} = \frac{1}{2}(E_{ex} + E_{SP}) \pm \sqrt{\Omega_R^2 + \frac{1}{4}(E_{SP} - E_{ex})^2} \tag{1.10}$$

In this expression, $E_{\pm}$ refers to the upper and lower plexcitonic resonances, E_{ex} is the exciton energy given by the J-band spectral position, and E_{SP} corresponds to the plasmonic response.

Since Ω_R is related to the system coupling strength (g) [64,67], we can estimate this parameter as follows:

$$g = \frac{1}{2}\sqrt{\Omega_R^2 + \frac{1}{4}(\Gamma_{SP} - \Gamma_{exc})^2} \tag{1.11}$$

Where Γ_{SP} and Γ_{ex} represent the line widths of plasmon and exciton absorbance responses. The hybrid light-matter modes originated from plasmon-polariton partially store their energy in the kinetic motion of the free carriers and, therefore, an inevitable dissipative loss occurs. Consequently, the energy in the LSPR is deposited into an adsorbed molecule, which can lead to its chemical transformations [71].

1.6.1 Switchable plexcitonic systems

Over the last two decades, much effort has been put into understanding the plexcitonic system either on a single particle level or in an ensemble state. For these structures, the two limiting regimes (weak and strong coupling) can be an exciting playground to develop a system undergoing a reversible transition from one regime to another. Furthermore, reversibly controlling the strength of coupling between the cavity and excitons is a versatile handle to switch between the emergent properties of the plexcitonic states and properties of the individual components [65].

The reversibility inherent in plexcitonic systems engenders promising applications in the realms of sensors where in response to specific environmental variations one can create switches within nanophotonic apparatuses. Within the domain of energy harvesting and conversion, the exploration of reversible plexcitonic systems gains traction for their potential to augment light absorption and energy transfer. Investigations into the dynamic tuning of coupling strength bear relevance to the efficiency of pivotal processes such as exciton transfer and charge separation, particularly pertinent in technologies like solar cells.

A careful analysis of the literature shows only a few recent studies where the authors focused on building actively manipulated hybrid systems [66]. In the following paragraphs we provide a brief overview of the current state-of-the-art switchable plexcitonic systems.

Baudrion et al. have proposed a system based on silver NPs arrays and photochromic molecules that exhibited switchable properties (see Figure 1.12**(a)**). These authors used photochromic spiropyran molecules that underwent isomerization to merocyanine under UV irradiation. Thus the switching mechanism from weak to strong coupling originated in the modification of the spectral position of the molecular absorption band with respect to the fixed plasmonic resonance. When the system reaches the strong coupling regime it has an estimated Rabi splitting energy value of 294 eV [72].

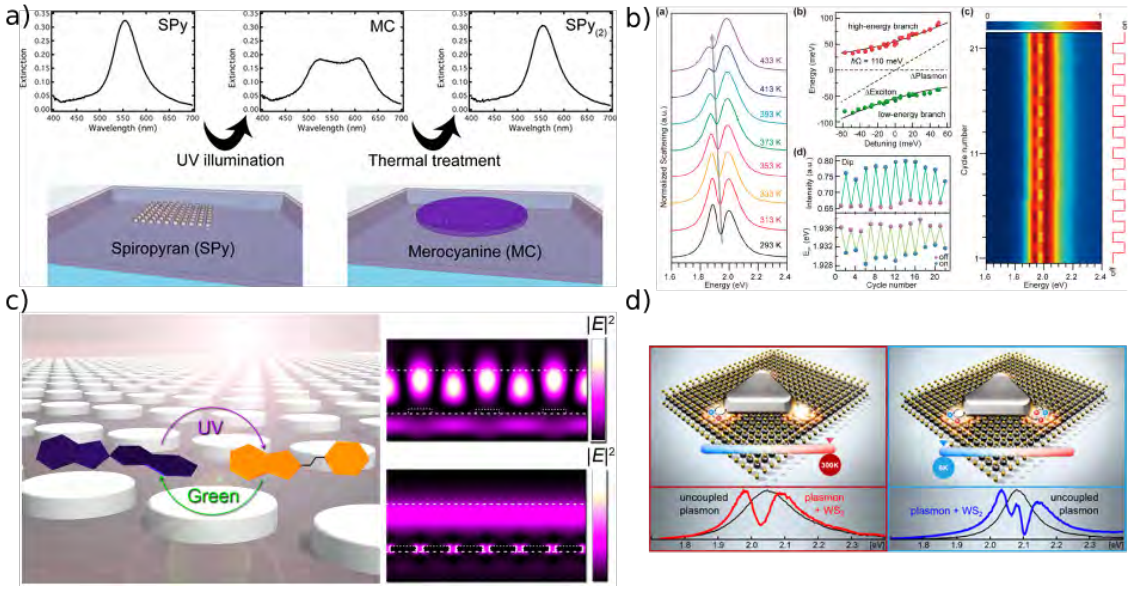

Figure 1.12: Reversible plexcitonic systems. (**a**) A reversible strong coupled system based on silver NP arrays using photochromic molecules (image taken from [72]). (**b**) Temperature dependant tunable charged exciton in a hybrid monolayer WS2-Plasmonic nanoantenna system (image taken from [73]). (**c**) A temperature-sensitive hybrid system based on a single plasmonic nanorod coupled with two-dimensional atomic crystals (image taken from [74]).(**d**) A photoswitchable rabi splitting hybrid system constituted by plasmon–waveguide modes interaction (image taken from [75]).

In other studies, there have been proposed switchable systems based on the

interaction of a single plasmonic nanostructure and a semiconductor layer. In this line, Wen et al. have studied a single Au nanorod coupled to a WS_2 monolayer where the coupling interaction was tuned by electrostatic gating or temperature (see Figure 1.12**(b)**). This system enables the change between the weak and strong coupling regimes, which was witnessed by reaching Rabi splitting energy up to 106 meV [74]. Another photoswitchable system was proposed by Lin et al. [75] The system was based on the coupling of hybrid plasmon–waveguide modes, where an aluminum nanodisks array interacted with photochromic molecules. The authors reached Rabi splitting of 572 meV (see Figure 1.12**(c)**). Similar results have been reported by Cuadra et al. [73], where the authors coupled a semiconductor monolayer to a single silver nanoparticle. The plasmon-exciton coupling was controlled through temperature change between 6 to 300 K Figure 1.12**(d)**. The reported strongly coupled system had a Rabi-splitting energy value of 120 meV at room temperature.

Some other studies have explored the interaction of QDs with plasmonic structures by changing the coupling strength through the distance between plasmonic nanoparticles and emitter [76, 77]. For example, May et al. [76] have proposed a precisely controlled system by using a plasmonic tip and a QD. The strong coupling regime was reached ($\Omega_R = 150$ meV) when the tip was close enough to the emitter because it acted as a tightly confined cavity through interaction with the QD and substrate. An alternative system has been presented by Gross et al. [77], where a nanoresonator placed on a scanning probe apex interacted with single QDs.

Furthermore, a NO_2 sensitive plexcitonic system able to switch from weak to strong coupling regime (130 meV) was presented by Berrier et al. [78] In the authors' design, the control of the oscillator strength depended on the exposure to nitrogen dioxide that changes the oscillator strength in the dye layer (porphyrin).

The discussed-above works clearly show that the ability to regulate reversibly the system's coupling strength holds promise for the development of innovative devices geared towards information storage, processing, and communication, predicated on manipulating light at the nanoscale. Also, this inherent reversibility can be harnessed for sensitive biological and chemical sensing, wherein the design of systems exhibiting reversible responses to specific molecular or environmental alterations affords the creation of versatile and responsive platforms for analyte detection and dynamic process monitoring. In this context, we shall discuss in Chapter 5 experimental results on how to control coupling strength in a colloidal plexcitonic system by the pH of the solution.

1.6.2 Enhanced photo-stability in plexcitonic systems.

The study of photostability in a plexcitonic system is crucial for several reasons, primarily driven by the potential applications and functionality of these systems in various fields such as optoelectronics, biology (sensing and imaging), and fundamental understanding [79]. Since the plexcitonic systems are nowadays of interest for applications in optoelectronic devices, such as light-emitting diodes (LEDs) and solar cells [61]. Understanding the photostability of these systems is essential to ensure the longevity and reliability of device performance under continuous or inter-

mittent exposure to light. The photostability studies help assess the durability of plexcitonic materials in practical device applications. And on a fundamental level, the investigation of the photostability of plexcitonic systems contributes to a deeper understanding of the underlying processes and mechanisms.

The photo-degradation and the consequent instability of potential photocatalysts can be mitigated by strong coupling. For example, it was reported that the resistance J-aggregates (JC-1) to degradation under pH and light was possible when these molecules were strongly coupled to gold nanorods [80] or silver triangles [81]. It was reasoned that improved stability of chromophores in the strong coupling regime was attributed to their proximity to the metal surface, which caused charge transfer processes and HOMO-LUMO gaps re-normalization [82]. We can also mention the P3HT chromophores strongly coupled to an FP cavity, where photo-degradation is reduced, and the key role of this decrease is attributed to the singlet oxygen mechanism [83].

The strong coupling is able to influence the chemical reactivity of molecules when they are coupled to a plasmonic nanosystem since it changes their photophysical properties by the formation of hybrid states [82]. The affected molecular properties are emission quantum yields, intersystem crossing, singlet fission, and lifetimes. But, also resonant Rayleigh scattering was reported to be enhanced due to the collective delocalized nature of the polaritonic states [84].

Chapter 2

Cross Determination of Exciton Coherence Length in J-Aggregates

2.1 Introduction

As mentioned in the introduction (Section 1.4.1.2), J-aggregates are supramolecular structures constituting organic molecules. They are organized into quasi-1D chains [85]. Strong in-line dipole-dipole coupling in these systems leads to the Frenkel excitons delocalization (Section 1.5.1). The coherence of the exciton wave function across several interconnected monomer units [86] renders a narrow absorption band (redshifted concerning the monomer) - the so-called J-band. [46, 87] The long-range exciton migration [57] can be quantified through the determination of exciton coherence length N_{coh} (Section 1.5.2). It is well-agreed that quantifying N_{coh} is critical for further advancement in developing J-aggregates-based hybrid systems. However, such quantification is challenging, as witnessed by the discrepancies in reported values even for J-aggregates of the same compound (see Appendix Table 1). This spread may be due to the different experimental conditions during sample preparation, as well as the issues and errors related to different analysis and measurement techniques. Therefore, there is a need to systematize the experimental means for the determination of N_{coh} among the different molecular systems.

The actual methods used in estimating N_{coh} involve: absorbance [58], transient absorption [88], and PL time-resolved [48] spectroscopies. A less common method implies the measurements of the Stokes shift between the maxima of the absorption and PL bands and the scaling of the Huang-Rhys (HR) parameter [89]. This parameter was derived to characterize the electron-phonon coupling strength in a crystal [90] but also can be applied in the description of the interaction of the molecular vibrations with electronic excitations [91].

The present Chapter deals with the determination of N_{coh} in two systems pre-

senting J-aggregation, namely JC-1 and S2275 dyes (both molecular systems were briefly introduced in Section 1.4.1.1). Four spectroscopic techniques are explored to estimate exciton coherence length. The first method involves the estimation of the N_{coh} determining the line width of the J-band and comparing it to the width of the monomer band. The second method requires the measurement of the absorbance and emission spectra, to obtain N_{coh} by employing the evaluation of the HR factor from the difference in position of the centers of the J-band absorbance and emission i.e. from Stokes shift. The third method involves the measurements of PL lifetime where N_{coh} can be estimated from the ratio between the monomer and J-aggregates emission rates. The last applied method, although applied to JC-1 dye only, is based on pump-probe (transient absorption) measurements. This method allows determining the difference between the one-exciton bleaching peak and two-exciton-induced absorption to find a value for the exciton wave function spread in the J-aggregates.

The formation of J-aggregates is a dynamic process taking place upon the chemical modification of the medium that allows the monomeric molecules to form larger structures. In the case of JC-1, this change is triggered by the increase in pH leading to the progressive formation of J-aggregates. In the case of S2275, it is the increased concentration of salt in the solution. Therefore, from the experimental point of view, the formation of J-aggregates is specific to a given dye. For JC-1, the N_{coh} was determined across a wide range of pH to determine its evolution under chemical stimulus. For S2275, we determined N_{coh} for fully-formed J-aggregates. This is due to the technical difficulties in monitoring the change of optical properties of this dye since the J-aggregates phase can be easily separated once they reach a certain aggregation (for more details see Chapter 3).

The coherence length of the Frenkel excitons (N_{coh}) is considered a critical parameter, it governs many key features of supramolecular J-aggregates. To determine experimentally the value of N_{coh} results is a non-trivial task since it is sensitive to the technique/method applied, causing discrepancies in literature data even for the same chemical compound and aggregation conditions. As mentioned above we use a combination of different experimental techniques including UV-Vis-NIR, fluorescence emission, time-resolved PL, and transient absorption spectroscopic to determine N_{coh} values for J-aggregates.

2.2 Materials and methods

2.2.1 Materials

Both dyes JC-1 (5,5',6,6'-Tetrachloro-1,1',3,3'-tetraethyl-imidacarbocyanine iodide, 5,5',6,6'-Tetrachloro-1,1',3,3'-tetraethylbenzimidazolocarbocyanine iodide) and S2275 dye (5-Chloro-2-[3-[5-chloro-3-(4-sulfobutyl)-3H-benzothiazol-2-ylidene]-propenyl]-3-(4-sulfobutyl)-benzothiazol-3-ium hydroxide, triethylammonium salt) were purchased from FEW Chemicals. The dimethyl sulfoxide (DMSO, $\geq$ 99%), sodium hydroxide (NaOH, $\geq$ 98%), and sodium chloride were purchased from Merck. And, the hydrochloric acid (HCl, $\geq$ 37%) was purchased from Scharlab.

2.2.2 Characterization

The absorption spectra of the samples were taken using a Cary 3500 UV-Vis spectrophotometer, and the emission spectra were measured using a Cary Eclipse Fluorescence Spectrophotometer (Agilent Technologies). The PL decays were acquired using a time-resolved confocal fluorescence microscope MicroTime 200 and a laser excitation of 485 nm. Here, the PL response of monomer and J-aggregates were separated using two filters of 510 nm and 593 nm, respectively. The lifetimes of the JC-1 monomer and J-aggregates were estimated by fitting the PL decay curves with SymPhoTime 64 software. The analysis of the J-aggregates with pump-probe spectroscopy was done with a custom-built transient absorption spectrometer from Newport Inc. The Ti:Sa amplifier was operating at 1 kHz (Libra from Coherent Inc.) and it acted as a light source. An OPA system (Opera Solo from Coherent Inc.) generated the excitation beam with a spot diameter of 350 μm, a pulse duration of 100 fs, and typical excitation powers of 13-55 $\mu J/cm^2$. All these measures were performed under ambient conditions.

2.2.3 Formation of J-aggregates

The J-aggregates comprising JC-1 were obtained after dissolving the JC-1 monomer (20 μL, 250 μM DMSO solution) in Milli-Q water (2 mL) in a plastic recipient. After that, we add NaOH (20 μL, 0.1 M aqueous solution) to increase the pH. Once the solution reaches a pH value over 8, we can observe a light pink color due to the presence of the J-aggregates.

The J-aggregates comprising S2275 were obtained after dissolving monomer (100 μL, 1mM methanol solution) in Milli-Q water (2 mL) in a plastic cuvette. Then, a NaCl aqueous solution (150 μL, 4M) was added to the solution containing dye (50 μM) under magnetic stirring and left for 10 minutes. Once the J-aggregates are formed the solution acquires blue color.

2.2.4 Estimation of quantum yield

The Quantum Yield (QY) is defined as the relation between the absorbed and emitted photons. The QY ($\Phi_{f,st}$) value estimation can be done using a reference sample through Equation 2.1 [92].

$$\Phi_{f,st} = \Phi_{f,st}\frac{F_x}{F_{st}}\frac{f_x(\lambda_{exc})}{f_{st}(\lambda_{exc})}\frac{n_x^2}{n_{st}^2} \tag{2.1}$$

Where F is the spectrally integrated photon flux given by the integrated area under the emission spectra, f represents the absorption factor at the excitation wavelength (λ_{exc}), and n is the refractive index of the solvent [92]. The 'st' sub-index refers to the standard solution with known QY, and 'x' is for the sample with unknown QY.

To estimate F, we used the following equation [92]:

$$F = \frac{1}{hc_0} \int_{\lambda_1}^{\lambda_2} I_C(\lambda_{exc}, \lambda_{em}) \lambda_{em} d\lambda_{em} \tag{2.2}$$

The parameter $I_C(\lambda_{exc}, \lambda_{em})$ is the area under the emission spectrum that is corrected for blank emission and the wavelength dependence of the instrument's spectral responsivity [92].

And we obtained f by applying the following equation:

$$f(\lambda_{exc}) = 1 - 10^{-A(\lambda_{exc})} \tag{2.3}$$

where $A(\lambda_{exc})$ represents the absorbance value at the excitation wavelength and

The quantum yield of JC-1 dye was estimated via the photon emission comparison with Rhodamine 6G dye ($\Phi = 0.95$ [93]). We chose this dye due to the spectral overlap with the absorbance response of JC-1 in monomeric form. First, to obtain comparable solutions, we used the absorbance spectrum of both dyes and compared the spectral intensity at the excitation wavelength (laser 485 nm), see Figure 2.1 **(a)**.

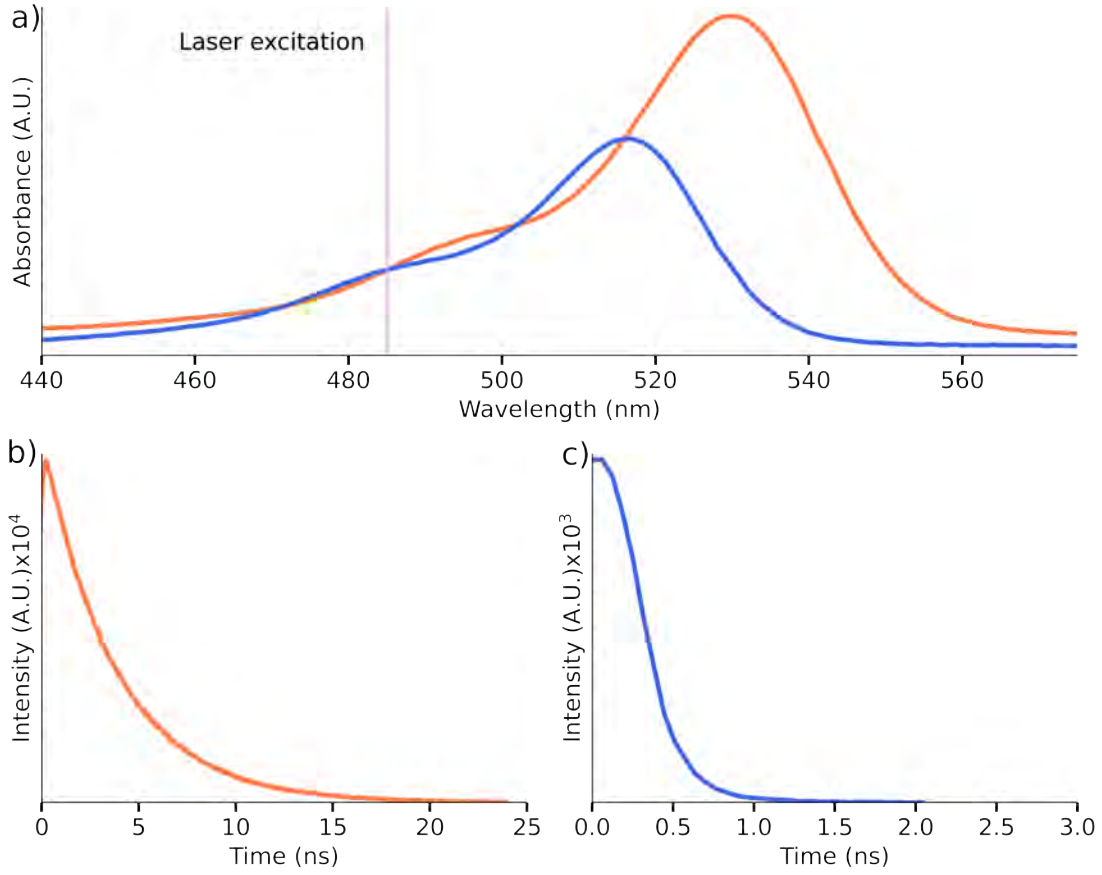

Figure 2.1: **(a)** JC-1 (blue) and Rhodamine 6G (orange) absorbance spectra in ethanol. The light purple line shows the used laser in PL measurements for the sample's excitation at 485 nm. **(b)** Photoluminescence decay measurement of Rhodamine 6G (orange) and **(c)** JC-1 monomer (blue) for photon emission count.

Then, the PL decay measurement of both solutions was performed (see Figure 2.1 **(b, c)**). Since the area under the decay curve represents the emitted photon, integrating both spectra allows us to quantify the emitted photons by each sample. Here, both PL measurements were performed under the same conditions and an equal absorbance intensity at 485 nm. We can ensure the absorbed photons quantity is the same in both cases and it is possible to relate $\Phi_{Rh6G} = 0.95$ and Φ_{JC1} and estimate the value for $\Phi_{JC1} = 0.05$.

However, to calculate J-aggregates QY we used Rhodamine 6G and a solution of core (CdSe)-shell (ZnS/CdS/ZnS) quantum dots. First, we estimated the QDs' quantum yield using the Rhodamine 6G and after this, we proceeded to estimate the J-aggregates QY. In this case, we used this middle step because there is no spectral overlap between the Rhodamine 6G and J-aggregates.

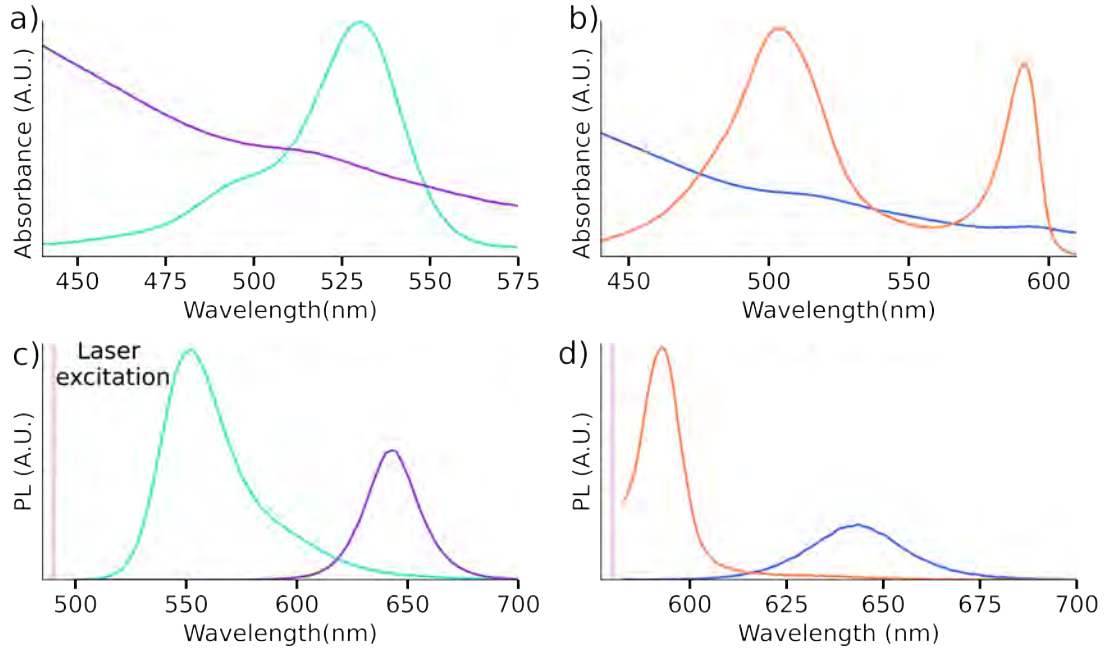

Figure 2.2: Absorption and PL spectra of Rhodamine 6G, QDs and J-aggregates. **(a)** Absorbance response of Rhodamine 6G (light blue) and QDs (violet). The red dotted line shows the excitation wavelength at 490 nm. **(b)** Absorbance spectra of J-aggregates and Quantum Dots. The light purple vertical line indicates the excitation wavelength at 580 nm. **(c)** PL response of Rhodamine 6G (light blue) and QDs (violet) with the excitation wavelength at 490 nm. **(d)** Photoluminescence spectra (excitation at 580 nm) of J-aggregates (orange) and Quantum Dots (blue).

Finally, we applied Equation 2.1 that allows the QY estimation using a reference sample [92]. Taking into account that Rhodamine 6G was in ethanol solution ($n = 1.36$), QDs were in hexane solution ($n = 1.37$), and J-aggregates in water ($n = 1.33$). The absorbance spectra of the solutions (Figure 2.2 **(a, b)**) were used to determine the parameter $A(\lambda_{exc})$. In the case of QDs' QY calculation, we choose the excitation wavelength 490 nm. For J-aggregates' QY the used excitation wavelength was 580 nm.

Once we established the excitation wavelength we measured the PL spectra (see Figure 2.2 **(c, d)**) to estimate parameter F (Equation 2.3) to later apply Equation 2.1. First, we obtained $\Phi_{QDs} = 0.4$, and then Φ_{Jagg}=0.3.

2.3 JC-1

As it was already introduced in Section 1.4.1.1, JC-1, a fluorescent dye, is widely utilized in cell biology and biochemistry assessing mitochondrial health and membrane potential [94,95]. This cationic carbocyanine dye is recognized for its ability to selectively accumulate in the mitochondria, where it undergoes potential-dependent aggregation. In healthy, polarized mitochondria, JC-1 forms aggregates with intense red fluorescence, while in depolarized or unhealthy mitochondria, the dye remains in its monomeric form, emitting green fluorescence. This property makes JC-1 a valuable tool for monitoring mitochondrial membrane potential changes, serving as an indicator of cellular health and function [94].

The JC-1 monomer molecule absorbance spectrum shows a maximum at 2.43 eV (510 nm) and a shoulder at 2.2 eV (563 nm). Its emission spectrum is almost a mirror image of the absorbance, however, with a maximum red-shifted by 0.11 eV (Figure 2.3 (**a**)). J-aggregates appear once NaOH is added to JC-1 in an aqueous solution due to an increase in the pH. The formation of aggregates can be perceived by the naked eye. Under UV light excitation the pale yellow solution becomes light pink (see inset in Figure 2.3 **(b)**). Importantly, the shift between the absorbance and PL response in J-aggregates is notably small and can even be considered nonexistent.

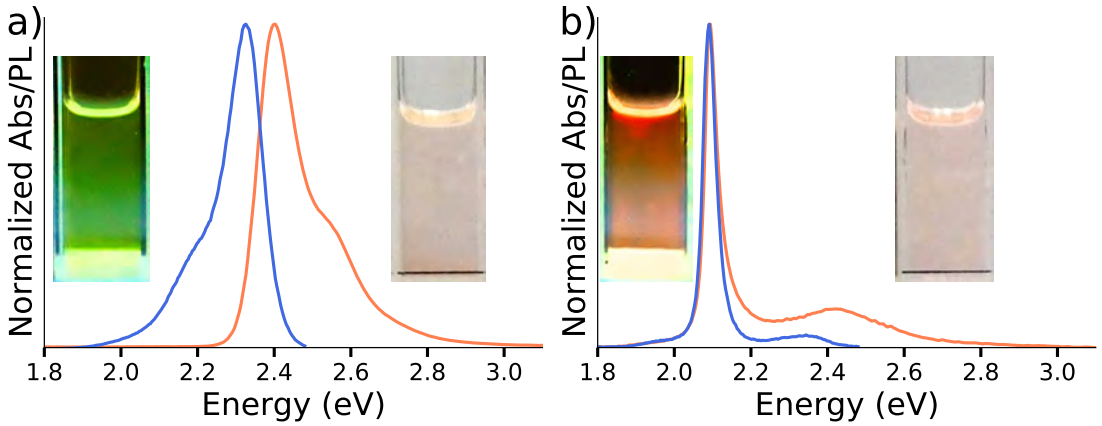

Figure 2.3: Monomer and J-aggregate absorbance and PL characterization. **(a)** Absorbance spectrum of the JC-1 monomer molecule (orange) with a maximum at 2.4 eV and a shoulder at 2.48 eV; emission spectrum (blue). Inset: digital images of the monomer's solution under UV illumination (left) and ambient light (right). **(b)** Absorbance (orange) and emission (blue) spectra of the J-aggregates, showing a narrow peak with a maximum near to 2.08 eV.

A more detailed insight on the J-aggregates was obtained through their optical characterization and this was performed for pH range from 8 to 11. The evolution

of the J-aggregates' absorbance and emission spectra as a function of solution pH is presented in Figure 2.4. In both spectra, at low pH, only the signature of the monomer is present. The signal from the J-band rapidly grows with increasing pH, becoming more intense and narrower than the monomer band. This behavior is due to molecular aggregation and the lower concentration of single molecules. However, while the absorbance saturates at pH > 11, the PL intensity reaches a maximum at pH=10.5 and then, it rapidly decreases.

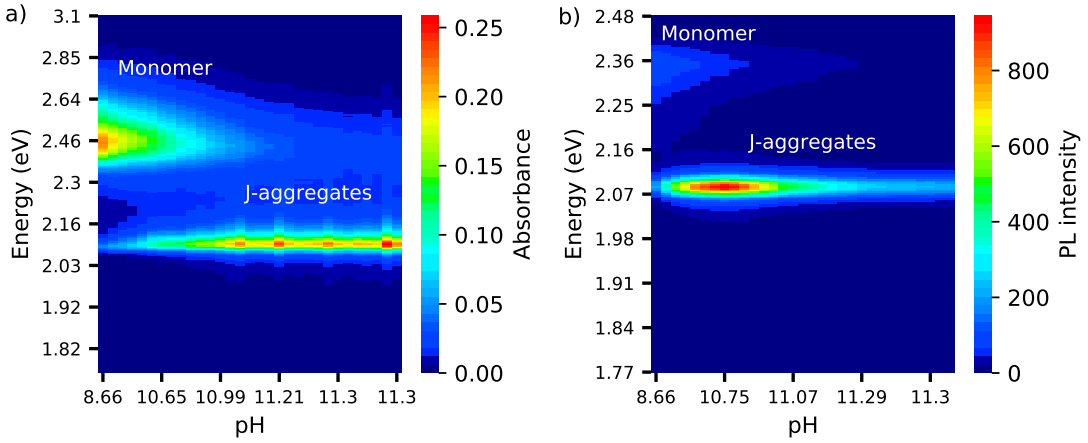

Figure 2.4: pH-dependent formation of J-aggregates. The pH was increased from 8.6 to 11.3 in sequential addition of NaOH (440 μL in 21 steps). a) Absorbance spectra. With increasing NaOH, the J-band progressively increases accompanied by a decrease in monomer band. b) Emission spectra. The emission from monomer decreases with pH while PL of the J-band appears immediately after the first addition of NaOH. The intensity of PL from J-aggregate decreases for pH > 10.5.

It has been shown that the line width modification of these bands is generally related to N_{coh} [96]. However, this approach for estimating N_{coh} was not seen as too accurate and precise because the bandwidth of the monomers forming J-aggregates may differ from that of monomers [97, 98]. Alternatively, Bakalis and Knoester have shown that the J-aggregate absorption bandwidth determines the energy separation between the two lowest states on one localization segment and related it to N_{coh}. They used numerical simulations to compare the results of both methods, concluding that in the best approach N_{coh} can be estimated by Equation 2.4.

$$N_{coh} = \sqrt{\frac{3\pi^2|J|}{W}} - 1 \tag{2.4}$$

This relation is established after analyzing linear molecular aggregates built by N molecules of two levels, considering static disorder, and in a regime where the coherence length is smaller with respect to the aggregate size. In our analysis, the width W of the JC-1 J-aggregates was obtained by fitting each absorbance spectra to a Voigt curve (Figure 2.5 a). This profile is a convolution of a Gaussian and a Lorentz distribution and was chosen because of the asymmetrical shape of the J-aggregate

spectra. The parameter J represents the dipole-dipole interaction strength in a molecular chain; it comes from the difference in maximum absorption wavelengths of J-band and monomer ((λ_{max}^{mon} and λ_{max}^{J})) and the following Equation 2.5 was implemented to estimate its value [96].

$$J = \frac{\lambda_{max}^{J} - \lambda_{max}^{mon}}{2.4} \tag{2.5}$$

This equation describes the molecular interaction in the chain. The value of 2.4 corresponds to the shift originated by the application of open boundary conditions and the inclusion of long-range interactions in the bottom exciton band [51, 99]. Here, the FWHM, λ_{max}^{mon} and λ_{max}^{J} were used in cm^{-1}.

The justification for Equation 2.4 arises from the increase in N_{coh} with the suppression of exciton-vibrational coupling and hence with a narrowing of the absorption band. However, the use of Equation 2.4 must be taken with caution because the correct measurement of the J value from the absorption shift of the J-band (Equation 2.5) requires accounting for the ground state level shift of the molecules [97].

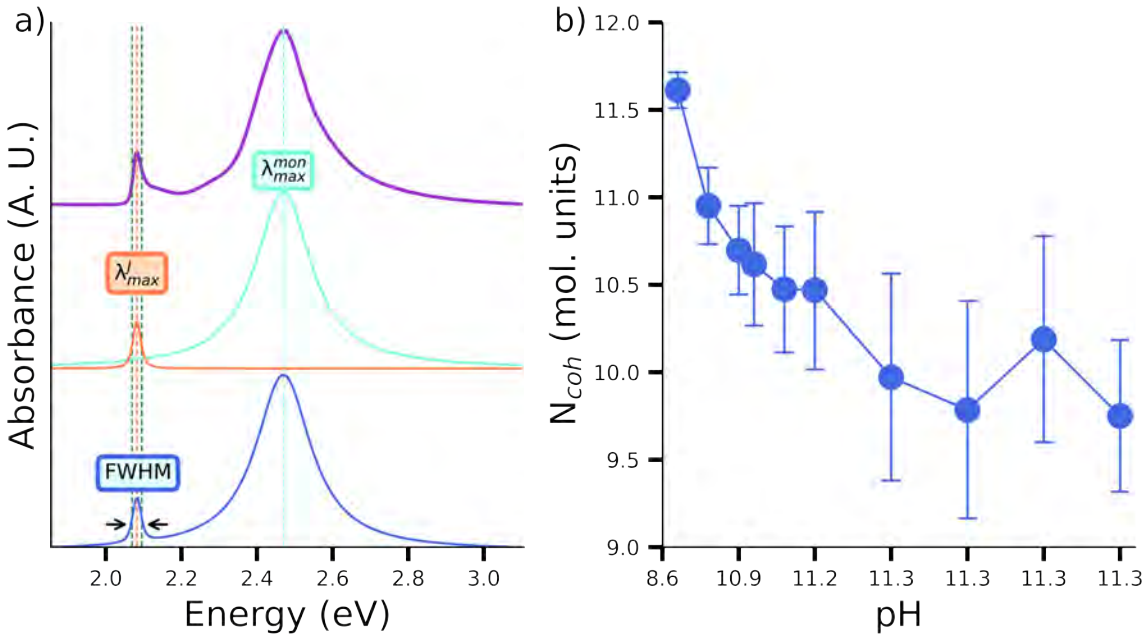

Figure 2.5: (a) Experimental absorbance spectrum of JC-1 in water taken at pH = 8.6 (violet). Voigt fits of the monomer absorbance (aquamarine), the J-band absorbance (orange), and the entire spectrum (blue). (b) pH-dependent N_{coh} estimated using Equation2.4 and the absorbance spectra. Each point corresponds to an exciton coherence value related to the pH of the solution.

Equations 2.5 and 2.4 allow us to obtain the value of N_{coh} using the analysis of the J-aggregates' absorbance spectrum. The average coherence length obtained using this method is 10.5. The evolution of this parameter is presented in Figure 2.5 b). In general, N_{coh} decreases with increasing pH, meaning that the exciton is coherent

over more molecules for lower pH values. The errors associated to N_{coh} in Figure 2.5 b stem from the difference between the fitted spectra and the measured ones and reflect the asymmetric shapes of the monomer and J-band responses.

Next, we move to determine N_{coh} based on PL measurements of J-aggregates for different pH values. The J-aggregates PL can provide information about the exciton coherence using the Stokes shift and radiative lifetime estimation. The Stokes shift is usually calculated as the difference between absorbance and emission maxima. It is related to the dimensionless HR parameter, which is a measure of the electron-phonon or electron–vibrational coupling strength [100]. Because of the ambiguity of the relationship between the Stokes shift and the HR parameter used in different articles, Jong et al. presented a more advanced analysis for the influence of thermal effects in the band maximum position and how to correct for possible errors due to these effects [91]. It is preferred to take the peak center of mass (E_{bc}) to solve the fitting problems derived from its asymmetric shape [101, 102]. The values of the energy barycenter (E_{bc}) can be estimated using the experimental absorption and emission spectra ($W(E)$) [91] as presented in the following equation:

$$E_{bc} = \frac{\int W(E) E \mathrm{d}E}{\int W(E) \mathrm{d}E} \tag{2.6}$$

Since the HR parameter (S) provides information about the microscopic details of the vibrational coupling, it can be related to the equilibrium position offset between the ground state and the excited state [91]. Equation 2.7 presents the relation between the difference in the energy barycenter of emission and absorbance spectra ΔE_{bc} and the value of S.

$$\Delta E_{bc} = 2S \tag{2.7}$$

The coherence length can be obtained using the scaling relation [89]:

$$N_{coh} = \sqrt{\frac{S(1)}{S(N)}} \tag{2.8}$$

where $S(1)$ represents the monomer Huang-Rhys parameter and S(N) the J-aggregates' HR parameter. This latter equation allows us to determine N_{coh} values from monomer and J-aggregate absorbance and emission data. The rationalization of this equation is that the shape of the spectral lines and the linewidth (which in turn is defined by the value of N) depends on the vibrational coupling strength and hence on S [100].

The estimated value of ΔE_{bc} for the JC-1 monomer is 0.20 eV, which is five times greater than the maximal value for the J-aggregates of $\Delta E_{bc} = 0.04eV$ (Figure 2.6 **(a)**. The value of the coherence length obtained from S is 3 molecular units on average. Figure 2.6 (**b**) shows N_{coh} value in function of pH and is can be noticed that this value decreases with J-aggregate concentration (higher pH value). Even when the absorbance spectra reveal the maximal J-aggregate concentration at pH

11.2 (see Figure 2.4 (**b**)), the first value of N_{coh} is the highest (5.2 at pH = 8) and the lowest is the final one (2.6), reached at the highest pH (11.3). Conversely, the first ΔE_{bc} value is the lowest (7 meV), increasing up to almost 35 meV. Evolutions of these quantities are shown in Figure 2.6 **(b)**.

The dispersed N_{coh} values found in this analysis could be due to the effect of pH changes induced by the step-wise addition of NaOH to the J-aggregate absorbance and emission spectra. However, we must take into account that in the model used to link the Huang-Rhys parameter with the coherence length value, we consider the line shapes of absorbance and PL spectra to be mirror-image symmetric. In general, this is not completely correct for J-aggregates, as these spectral observables result from different excitonic properties. While the absorbance response is related to the exciton bandwidth, the PL is associated with the exciton coherence length N_{coh} [103].

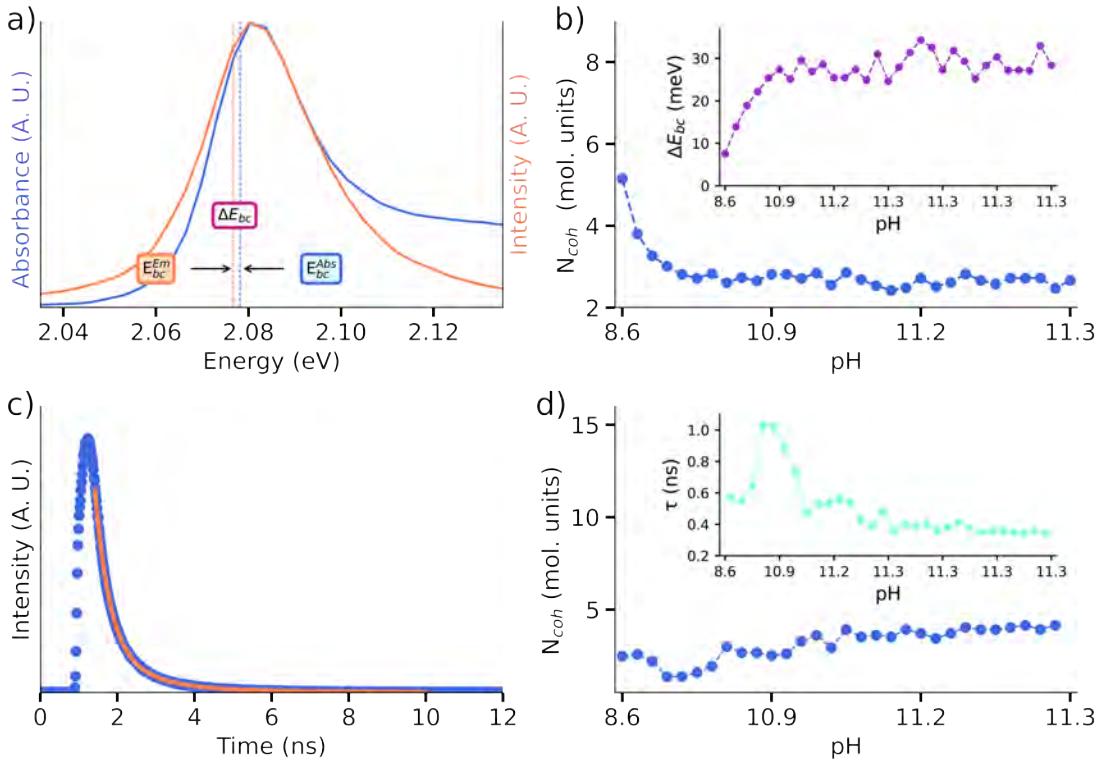

Figure 2.6: Results of analysis of J-aggregate absorption and PL to calculate the exciton coherence length: (a) Stokes shift Δ E_{bc} estimation using energy barycenters of absorbance (blue) and emission (orange) spectra, b) Evolution of the coherence length (estimated from Huang-Rhys parameter) with pH, c) PL intensity decay (blue circles) and the result of the double exponential fitting (orange line) of JC-1 solution with pH = 8.6, and d) PL lifetimes (τ) of J-aggregates (aquamarine dots) and N_{coh} calculated from radiative decay rates of monomer and J-aggregates in function of pH.

Another selected technique to estimate N_{coh} is Time-Resolved Photoluminescence (TRPL) spectroscopy. TRPL is considered an advanced spectroscopic technique employed to study the temporal evolution of photoluminescent signals, in contrast to

traditional PL measurements, which provides information about the emitted light's intensity and spectral distribution. TRPL goes a step further by offering insights into the dynamics of electronic processes occurring on timescales ranging from picoseconds to microseconds. This temporal resolution is crucial for understanding phenomena such as carrier recombination, migration, or trapping.

In practice, in a typical TRPL experiment, a sample is excited with a short pulse of light, often generated by a pulsed laser, initiating the creation of electron-hole pairs. The subsequent emission of PL is then monitored as a function of time with a high-speed detector. Then, by precisely tracking the decay of the luminescent signal, one can extract valuable information about carrier lifetimes, radiative and non-radiative recombination processes, and the overall efficiency of light-emitting materials.

To analyze the PL decay signal we used SymPhoTime software. It allows applying the multiexponential model expressed in Equation 2.9 to estimate the lifetime values:

$$y(t) = \sum_{i=0}^{n-1} A[i] e^{-\frac{t-t_0}{\tau[i]}} + bkgr_{dec} \tag{2.9}$$

where n is the number of the model parameters (we used n=1 for monomer and n=2 for J-aggregates), t represents the variable time, t_0 is the extrapolated reference point for scaling the exponential prefactors, A gives the exponential prefactors (amplitudes), τ represents the exponential decay times (lifetimes) and the background in the measurement is given by bk_{dec}.

The radiative and non-radiative rates determine the ratio of emitted and absorbed photons, they are constant and independent. In this analysis, we use the relation between the coherence length value and the radiative rate due to the dipole moment enhancement in the molecular chains [54]. The quantum yield (Φ) for JC-1 monomer and J-aggregates estimation was previously shown in Section 2.2.4. We obtained $\Phi = 0.05$ for the monomer and, in the case of J-aggregates $\Phi = 0.3$. On the other hand, the lifetime (τ_{Av}) of J-aggregates resulted in 0.5 ns and 0.18 ns for the monomeric form.

The scaling relation of the radiative lifetime [89] was applied to obtain the coherence length using Equation 2.10. According to the seminal work of Kasha [104,105], the dipole moment of a linear chain of molecules (i.e. J-aggregates) increases as $\mu_J = (\mathrm{N}_{coh})^1/2\ \mu_J$, where μ_J and μ_{mon} are the dipole moments of the aggregate and monomer, respectively. Since the radiative rate constant for the dipole-allowed transition can be expressed as $\mathrm{k}_{rad} = 4\mu^2/3\hbar^3\lambda^3c^3$, N_{coh} can be found using radiative rate constants of the exciton and monomer based on the measurement of emission decay.

$$N_{coh} = \frac{k_r(N)}{k_r(1)} \left(\frac{\lambda_J}{\lambda(1)} \right)^3 \tag{2.10}$$

Equation 2.10 shows the relation between the coherence length, the radiative rates of J-aggregates $k_r(N)$ and the monomer $k_r(1)$, and the emission wavelengths of J-band λ_J and monomer $\lambda(1)$. To obtain the radiative rate of monomer and J-aggregates from the lifetime value, we applied Equation 2.11 [106].

$$k_r = \frac{\Phi}{\tau} \tag{2.11}$$

The applicability of Equation 2.10 can be limited by warping affecting the molecules in general. Such deformation can oppose the coherence of exciton [107].

From these equations, we estimated the coherence length of J-aggregates, in the case of measured lifetime analysis, resulting $N_{coh} = 3$ molecular units. The corresponding values are presented in Figure 2.6 (**d**). The results in both estimations exhibit a similar average value and can be considered close to the ones obtained using the emission spectra (Figure 2.6 **(b)**) from the Huang-Rhys parameter, which was expected as they are also related to J-aggregate PL.

After the estimation of N_{coh}, taking into account the pH's variation in the solution and using absorbance and PL analysis, we established that the coherence length decreases with pH value. Also, it is important to point out that the intensity of the PL response (see Figure 2.4) dropped after a certain pH value. Both phenomena can be related to non-diagonal and diagonal J-aggregate disorder [108].

Next, we move to another experimental technique - Transient absorption spectroscopy (TAS) - to estimate N_{coh} in J-aggregates comprising JC-1. TAS is a powerful and versatile technique used to investigate the dynamics of photo-excited states in materials. This spectroscopic method provides valuable information about the time-dependent changes in absorption following the excitation of a sample with a short laser pulse. By measuring how the absorption spectrum evolves, one can unravel electronic relaxation, energy transfer, and chemical reactions. TAS is particularly well-suited for studying ultrafast phenomena on timescales ranging from femtoseconds to milliseconds.

In a typical transient absorption experiment, a pump laser pulse initiates the photoexcitation of the sample, and a probe laser pulse monitors the changes in absorption at different delay times after the excitation. The resulting transient absorption spectrum reveals the dynamics of excited states and their relaxation pathways.

The J-aggregates pump-probe spectra (Figure 2.7 **(a)**) are characterized by two peaks: one corresponding to the J-band response (where ΔOD is negative) at 2.1 eV, and a second one (ΔOD is positive) in the range of 2.13-2.25 eV. The last is due to a cascaded biexcitonic transition that causes photo-induced absorption at higher energies [109]. The negative contribution in the spectra comes from the transition of the excited singlet exciton to two exciton states, and it produces ground-state bleaching and stimulated emission.

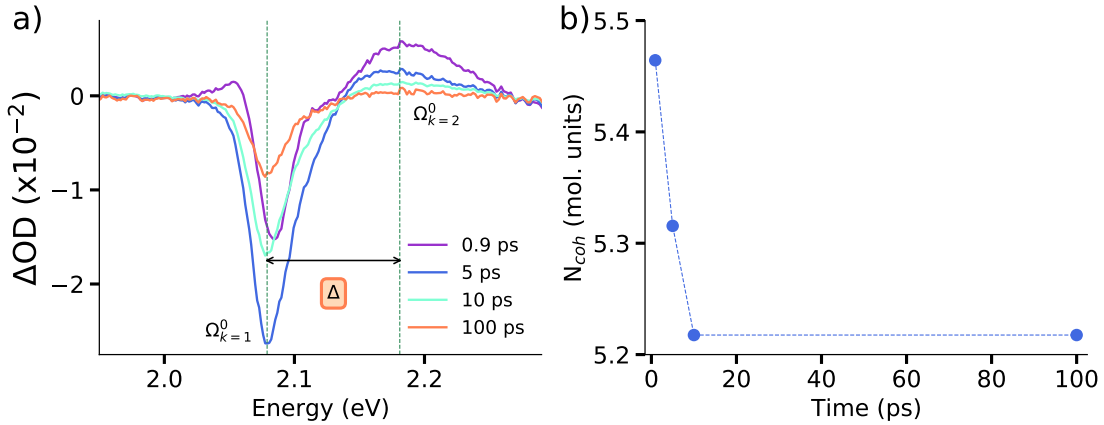

Figure 2.7: Estimation of N_{coh} from transient absorption measurements (a) Pump-probe spectra of J-aggregates for different delay times between probe and pump laser and the spectral separation Δ for the spectrum taken at 5 ps delay time. (b) N_{coh} values determined for the spectra presented in (a).

The pump-probe spectra of J-aggregates show a separation Δ (Figure 2.7 **(b)**), which is the blueshift between the two dominant transitions ($\Omega^0_{k=1}$ corresponding to the single exciton bleaching peak and $\Omega^0_{k=2}$ the one- to two-exciton induced absorption) in the pump-probe spectrum [59]. Equation 2.12 relates this value to the nearest-neighbor transfer interactions J and N_{coh} [60].

$$N_{coh} = \sqrt{\frac{3\pi^2|J|}{\Delta}} - 1 \tag{2.12}$$

The following relation defines the term Δ:

$$\Delta = \Omega^0_{k=2} - \Omega^0_{k=1} \tag{2.13}$$

The limits of application of Equation 2.12 are given by spectrum saturation: the pump-probe spectrum shape is dominated by homogeneous line width. The origin of this saturation is the overlap of bleaching and induced absorption contributions due to further disorder decrease. [60] Then, Δ is related to the saturation length [59].

Equations 2.12 and 2.13 allowed us to estimate the coherence length of the J-aggregates (Figure 2.7 **(b)**). The obtained value of N_{coh} on average is 5.3. It was estimated from the results of each spectrum taken at different delay times between the pump and probe laser.

The data acquired above through the analysis of the absorption, PL, lifetimes, and transient absorption measurements are summarized in Table 2.1.

The value of N_{coh} can be established as 4 molecular units for JC-1 J-aggregates. In the case of the J-band linewidth-associated calculation, the obtained values are higher than the other estimated ones that were found using different methods. This difference can be attributed to the direct influence of the irregular band shape in the absorbance spectra. Looking at some reported values of coherence length for

J-aggregates of other molecules [34, 47, 48, 88, 107, 110–132], one can deduce the concordance in the coherence length values with those obtained for JC-1.

If we compare this value with the already reported for different J-aggregates, we found that the closest values are the estimated for TDBC [34], DMDC [111], and PIC [110]. $N_{coh} = 4$ (molecular units) was reported for all three, also a coherence length value of 6 molecular units was found for TDBC [115] (using PL decay analysis) and for Thyacarbocyanine [119].

Table 2.1: Table summarizing the applied methods for JC-1 J-aggregates N_{coh} determination: N_{coh} value, advantages, shortcomings and references.

Technique	**N_{coh}**	**Advantages**	**Shortcomings**	**Ref.**
Absorbance J-band's linewidth	10.5	Only requires absorbance spectrum.	Error estimation from J-band.	[58]
Huang-Rhys parameter	3	Avoids thermal effects influence.	Considers absorbance and PL line shapes mirror-image symmetric.	[91, 103]
PL lifetimes	3	Only PL is analyzed: lifetimes, QY and emission wavelengths.	Warping effects on the molecules.	[89, 104] [54, 105]
Transient absorption	5.3	Only requires TA spectrum.	Spectrum saturation and sophisticated equipment is required.	[59, 109]

The pH relation with the exciton coherence length of J-aggregates can be explained by their oxidation. The J-aggregates become oxidized in acidic environments (small pH values), which leads to a drop in absorbance and fluorescence. This makes acidic conditions inherently disruptive for the coherence length. In contrast, oxidation becomes no longer possible under basic conditions (up to about pH 10), where we found that the N_{coh} value stabilizes.

Next we asked whether having the knowledge of N_{coh} value one can estimate the concentration of the exciton in the solution. The importance of the exciton concentration relies upon its influence on the luminescence efficiency [133], the mainly leveraged property of J-aggregates in applications. Also, knowing the concentration of exciton in the solution can be important information while designing a photocatalytic system based on J-aggregates. The concentration of monomer molecules in the original solution (n_m) was $\sim 1.24 \times 10^{18}$ [monomer molec./m^{-3}] and that the exciton extends over ~ 4 monomer molecules. With these data, we found that there are 3.1×10^{17} excitons per m^{-3} in our solution.

Finally, to complete the analysis one can also estimate the value of the exciton oscillator strength, a value that was, in fact, never reported for JC-1. For this purpose, we can use the exciton's absorption cross-section (σ_J) and the following

equation:

$$\sigma_J = \frac{2.3DN_{coh}}{n_m l} \tag{2.14}$$

where D is the J-band absorption maximum and l is the light path length (1 cm). Taking $N_{coh} = 4$ in Equation 2.14, we obtain $\sigma_J = 1.05\times10^{-19}$ [cm ^{2}] (using the mean value of the J-band maximum). Then, we can calculate the transition dipole moment with σ_J, the vacuum permittivity ϵ_0, the Planck constant h, the FWHM of the J-band (using the mean value of the estimated FWHM), and the resonance wavelength λ:

$$\mu = \sqrt{\frac{3}{4\pi^3} h\sigma_J \epsilon_0 \gamma_0 \lambda} \tag{2.15}$$

Using $\mu = 8.5\times10^{-59}$ $[Cm]$ obtained from the latter equation, the mass of the electron m, the frequency of the J-band absorption maximum ν, and the electron charge e it is possible to estimate the oscillator strength applying Equation 2.16:

$$f = \frac{8\pi^2 m\nu|\mu^2|}{e^2 3h} \tag{2.16}$$

We found $f = 0.04$ for JC-1 with $N_{coh} = 4$, which is a comparable value with the reported oscillator strength for PIC J-aggregates ($f_{PIC} = 2.94$ with N_{coh}^{PIC}=347) since they present an absorbance maximum at a similar wavelength [55]. The ratio $\frac{f}{N_{coh}}$=0.008 (for JC-1 and PIC) helps to illustrate this comparison.

2.4 S2275 molecule

As mentioned in the introduction section 1.4.1.1, S2275 is a dye characterized by its high molar absorptivity and strong fluorescence emission in the near-infrared (NIR) region. The presence of chlorine groups, sulfobutyl functionalities, and triethylammonium salt contribute to its solubility and stability. Its excitation and emission wavelengths in the NIR region minimize interference from background autofluorescence and light scattering, allowing for improved sensitivity and resolution in fluorescence imaging.

The S2275 dye presents its monomeric form in a methanol solution, with an absorbance maximum of 566 nm. Figure 2.8 **(a)** shows the absorbance and PL response coming from the monomer. The maxima of both responses ($\lambda_{max}^{abs} = 566$ nm and $\lambda_{max}^{PL} = 582$ nm) are separated by a 14 nm Stokes shift.

On the other hand, the formation of J-aggregates results in the appearance of a sharp absorbance J-band at 650 nm (see Figure 2.8 **(b)**). The J-band is narrower and red-shifted with respect to the monomeric response in this case and it is located at 651 nm (absorbance) and 662 nm (PL). The Stokes shift is 11 nm, shorter than the one shown by the monomer solution. The intensity of the J-band increases with increasing concentrations of NaCl.

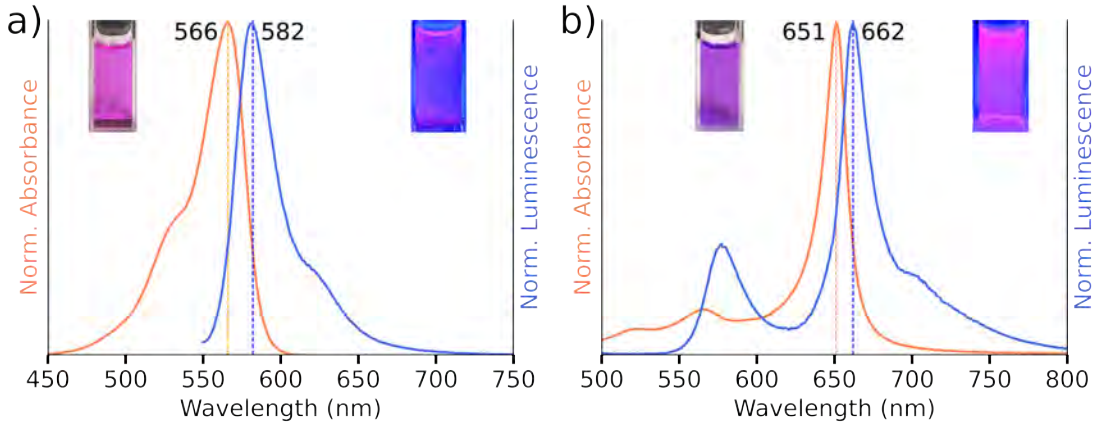

Figure 2.8: **(a)** Optical properties of monomer. Absorbance spectrum (orange line) and the PL spectrum (blue) of the S2275 monomer. The maxima of both bands are separated by the Stokes shift of 16 nm. Excitation wavelength: 550 nm. **(b)** Optical properties of J-aggregates. The absorbance (orange line) and PL (blue line) responses of J-aggregates reflect the narrower and shifted band.

The coherence length of the J-aggregates excitons in S2275 dye was estimated using some of the previously applied methods for JC-1 molecular chains. First, to apply Equation 2.4, we need to estimate the value of J using Equation 2.5.

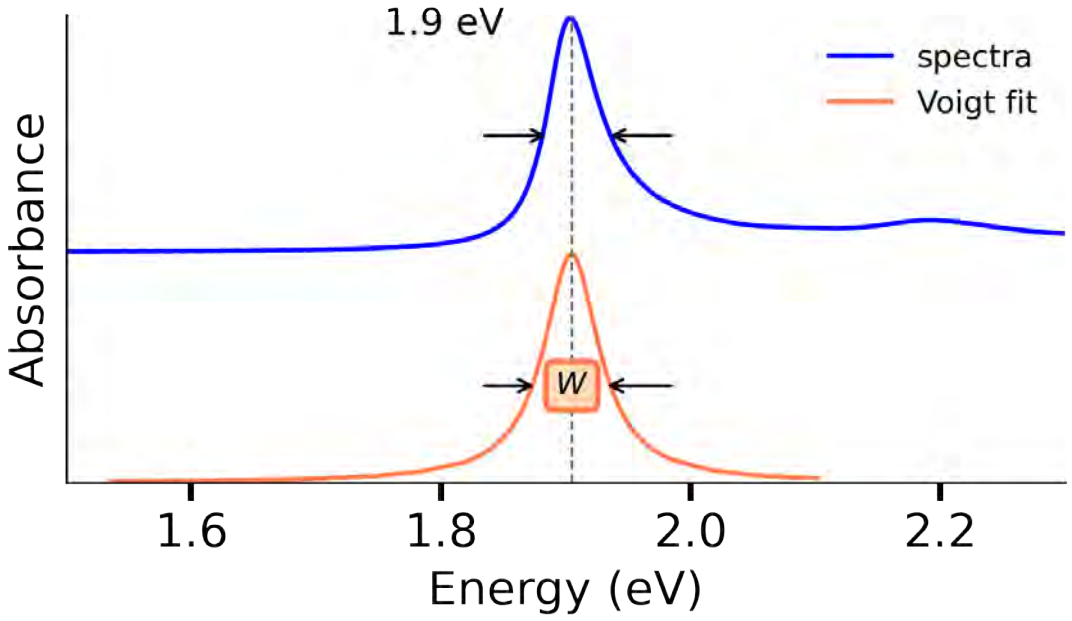

Figure 2.9: Analysis of dye J-aggregates absorbance response to estimate N_{coh}. The J-band absorbance (blue line) was fitted using the Voigt model (orange line), to calculate the spectrum linewidth.

From the absorbance response data obtained for the monomer and J-aggregates (Figure 2.8), we have $|J| = 0.12$ eV. Then, we estimated the W of the J-band applying

a Voigt fitting (Figure 2.9), and the value obtained for the exciton coherence length applying Equation 2.4 is 7 molecular units.

The use of both absorbance and PL response of J-aggregates allows us to estimate the value of N_{coh} by the Huang Rhys parameter relation (Equation 2.8). First, we calculated the energy barycenter for the monomer and J-aggregates using the measured absorbance and PL responses (see Figure 2.10) $S(1) = 0.09$, $S(N) = 0.03$. The obtained value applying the Huang Rhys parameter criteria for N_{coh} is 2 molecular units.

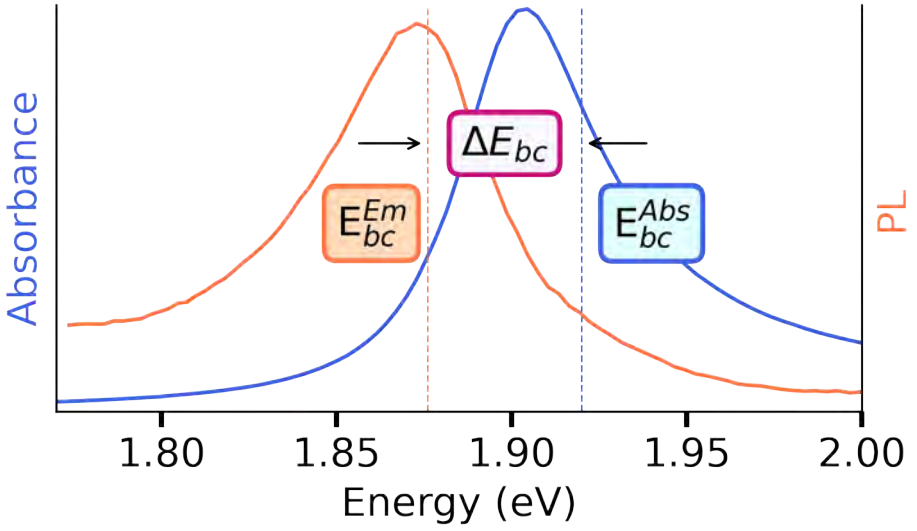

Figure 2.10: Analysis of the energy barycenter for dye j-aggregates. The absorbance E_{bc}^{Abs} and PL E_{bc}^{Em} values were estimated using Equation 2.7 to evaluate ΔE_{bc}.

The absorbance and PL of J-aggregates were analyzed to estimate the exciton coherence length, we obtained similar results to the JC-1 J-aggregates. For the absorbance linewidth analysis, we obtained a larger value in comparison to the combined analysis provided by the HR criteria, where it was related to the energy barycenter value of the spectral response. From this, we will take the value of 4 molecular units, as the representative value of our analysis.

The exciton concentration for S2275 J-aggregates solutions was estimated from the monomer molecules concentration in the initial solution ($n_m = 3 \times 10^{22}$ [monomer molec./m^3]) and exciton coherence length equal to 4 molecular units. Using these numbers, we can estimate the exciton concentration that results in 7.5×10^{21} excitons per m^3.

The value of the oscillator strength depends on several parameters as the exciton's absorption cross-section (σ_J) and the transition dipole moment (μ). Applying Equation 2.14 we obtained $\sigma_J = 2.14 \times 10^{-20}$ [cm^2], and through Equation 2.15 we have $\mu = 7.5 \times 10^{-20}$. Finally, through Equation 2.16 we were able to find $f = 0.6$ for S2275 J-aggregates. This value is higher than the obtained for J-aggregates comprising JC-1, but similar to the f value of PIC dye J-aggregates: 2.94 (see Table 1).

However, the obtained exciton coherence lengths' values for JC-1 and S2275 dyes are close according to the analyzed spectroscopic properties.

2.5 Conclusions

The excitonic properties of two dyes forming J-aggregates were studied using several spectroscopic techniques: absorption, transient absorption, PL, and PL lifetimes. The results presented in this chapter show that a correct and reliable determination of the exciton coherence length requires a careful and comprehensive approach. In practice, it seems clear that this cannot be done using single-experimental analysis at fixed experimental conditions. The analysis of all the data obtained from each one of the mentioned techniques allowed us to build a better picture of the excitonic behavior in the monomer chains and in particular a better understanding of the aggregation process as shown for the effect of pH on the formation of J-aggregates from JC-1 dye. Also, it is important to stress that the quantification of parameters in complex supramolecular systems such as J-aggregates contributes to their current and future use in a variety of light-related applications.

Finally, the characterized systems of J-aggregates for both dyes will be further used in the following chapters in which we shall use them to construct plexcitonic systems and study their optical properties and their eventual suitability in targeted applications.

Chapter 3

Plexcitonic System based on J-aggregates strongly coupled to TMA Capped Gold Nanoparticles

3.1 Introduction

In the rapidly advancing field of nanoscience and nanotechnology, the exploration of novel hybrid systems has garnered significant attention, paving the way for innovative applications in photonics, sensing, and energy harvesting [61, 62]. Plexcitonic systems are based on the coupling of plasmons and excitons. This interdisciplinary convergence of plasmonics and excitonics holds immense promise for manipulating and harnessing light-matter interactions at the nanoscale [134, 135]. To build these systems plasmonic NPs can be used to couple to excitons originating from either inorganic [136–141] or organic materials [61, 67, 80, 142–144]. In the context of organic materials, a plexcitonic system can be established using dyes [72, 145] or dye aggregates. These aggregates can be categorized into J-aggregates and H-aggregates, each presenting distinct properties compared to the non-aggregated dyes. These properties arise from the interaction of molecular transition dipole moments that interact upon the formation of molecular chains. [52] Here, J-aggregates are characterized by a sharp and red-shifted absorption and emission response [146], while H-aggregates exhibit a broad and blue-shifted absorption and emission response [147] in comparison to the monomer. Among these, J-aggregates are frequently employed in constructing plexcitonic systems [61, 67, 80, 142–144] due to their sharp absorption and emission features as well as the small or negligible difference between the absorption and emission maxima (Stokes shift). These distinct features emerge from the exciton coherence length that takes place in the J-aggregates [146, 148].

Among the previously described systems, plexcitonic systems which integrate

plasmonic excitations in metallic nanoparticles with excitonic states in molecular aggregates, stand out as a compelling avenue of research [63, 149]. Gold nanoparticles, renowned for their exceptional optical properties related to their localized surface plasmon resonance (LSPR) [15, 150], seamlessly combined with J-aggregates, molecular assemblies with distinctive excitonic characteristics [35, 151], form the crux of this study. Understanding and manipulating the intricate dynamics within plexcitonic systems not only unravel fundamental insights into the nature of light-matter interactions but also pave the way for the development of advanced nanophotonic devices and efficient energy conversion platforms. In this chapter, we delve into the contextual significance of studying plexcitonic systems, elucidating their underlying principles, and highlighting their potential impact on emerging technologies.

This chapter provides a comprehensive examination of hybrid fluorescent gold bipyramidal-like hybrid nanostructures. The chemical synthesis of these gold bipyramids, coupled with fluorescent J-aggregates utilizing a cost-effective and affordable non-cyanine dye, is detailed along with an exploration of their photophysical properties. Another important aspect is the use of electrostatic interactions to reliably form plexcitonic systems. For this, interaction with negatively charged molecules was required and it was crucial to develop a surface functionalization strategy to make BPs positively charged by a ligand exchange process. We not only demonstrate a new plexcitonic system comprising gold bipyramids (AuBPs) and S2275 dye J-aggregates but also show the impact of this coupling in enhancing the photostability of the J-aggregates and expanding the absorption spectral range of the plexcitonic system when compared to bare J-aggregates. The advantages of our system arise not only from the unique characteristics of the components but also from their coupling. For instance, the absorption and emission response of J-aggregates in the NIR region renders them suitable for biological applications. Furthermore, AuBPs are anisotropic sharp gold nanostructures that display intriguing characteristics, attributed to the potent electric field generated at their edges and tips. They exhibit narrow and intense LSPR responses and have only recently gained attention for building plexcitonic systems. To the best of our knowledge, there exists a limited number of studies involving AuBPs/J-aggregates of cyanine dyes [8, 152]. However, it is worth noting that despite the common use of TDBC in strong coupling experiments [153], its stability in J-aggregate morphology is rather compromised, as is the case with most cyanine dyes. Most notably, we demonstrate the fabrication of the plexcitonic system in the solution state, enabling the simultaneous production of multiple homogeneously coupled AuBP/J-aggregates nanosystems.

3.2 Materials and Methods:

3.2.1 Materials:

The chosen dye for this work was 5-Chloro-2-[3-[5-chloro-3-(4-sulfobutyl)-3H-benzo thiazol-2-ylidene]-propenyl]-3-(4-sulfobutyl)-benzothiazol-3-ium hydroxide, inner salt, triethylammonium salt (S2275 dye) and was purchased from FEW Chemicals. To form the J-aggregates we used Sodium Chloride (NaCl)from Sigma Aldrich. For

the particle stabilization we used Cetyltrimethylammonium Bromide (CTAB), (11-Mercaptoundecyl)trimethylammonium bromide (TMA), and poly(diallyldimethyl ammonium chloride) (PDDA) that were purchased from Sigma Aldrich, and 11-Mercaptoundecane-1-sulfonic acid sodium salt (MUS) that was purchased from Prochimia. Borosilicate cover glass (thickness 0.13 - 0.16 mm) was used to prepare solid-state samples and was purchased from VWR International.

3.2.2 Formation of J-aggregates

The S2275 dye presents its monomeric form in a methanol solution, with an absorbance maximum of 566 nm (see Figure 2.8). However, to observe the formation of J-aggregates a NaCl aqueous solution is required. The formation of J-aggregates results in the appearance of a sharp absorbance J-band at 651 nm (see Figure 2.8**(b)**). The intensity of the J-band increases with increasing concentrations of NaCl. More details about this dye J-aggregates are provided in Chapter 2, section 2.4.

3.2.3 Synthesis of AuBPs

AuBPs were synthesized through a well-established experimental protocol [21]. The seeds were prepared by adding NaBH4 (250 μL, 25 mM) to the mixture containing gold salt (50 μL, 50 mM), citric acid (50 μL, 1M) and CTAC (10 mL, 50 mM). Finally, the seeds solution was thermally treated (80 °C, 90 min).

Later, the AuBPs were grown from the gold seeds, these were added to a solution of CTAB (100 mL, 100 mM), $HAuCl_4$ (5 mL, 10 mM), $AgNO_3$ (1 mL, 10 mM), HCl (2 mL, 1M) and AA (0.8 mL, 100 mM). The solution was incubated at 30 °C for 2 hours under magnetic stirring, and UV-Vis-NIR spectra showed us spectral signature correspondent to AuBPs given by their characteristic plasmonic resonances. The amount of seeds in the growing solution allows us to control the AuBPs plasmon response: using a volume smaller than 3 mL we will obtain an LSPR $\geq$ 700 nm, for greater volumes, the plasmon response will be lower than 700 nm. The final solution was stored in CTAB 15 mM.

3.2.4 Ligand exchange Au-TMA

First, the AuBPs were functionalized using TMA to obtain positively charged particles. To begin with, AuBPs-CTAB were centrifuged (10 mL, [Au]=0.5 mM, 1 mM CTAB), and redispersed in Milli-Q water (8 mL). To this solution, TMA (2 mg/mL, 2mL) was added dropwise under magnetic stirring. After incubation for 1 hour, the functionalized particles were centrifuged and redispersed in water. This purification step was repeated two times.

3.2.5 Ligand exchange Au-MUS

The influence of electrostatic interactions on the formation of the plexcitonic system was tested by functionalizing the AuBPs with a negatively charged molecule.

Here, MUS and a functionalization strategy similar to what was used for TMA were employed.

3.2.6 Hybrid systems

The synthesis of gold nanoparticles - J-aggregates hybrid systems was carried out in solution. The hybrids were prepared by adding dye (1 mM, 70 μL) to AuBPs-TMA ([Au^0] = 0.5mM, 2mL). Subsequently, we added NaCl (4M, 25 μL) under magnetic stirring to initiate J-aggregates formation. Within 10 mins, we observed the spectroscopic signatures indicating the formation of a plexcitonic system, i.e. the formation of a doublet structure near the exciton and plasmon resonance position. A similar protocol was followed to study the formation of a plexcitonic system with AuBPs-TMA and AuBPs-MUS.

3.2.7 Substrate preparation

Also, a J-aggregate layer was deposited on a borosilicate cover glass for performing photophysical measurements. The cover glass was cleaned using acetone and ethanol and subsequently functionalized with a positively charged polyelectrolyte i.e. PDDA. To do this, the cleaned glass was covered with a thin layer of PDDA solution (1 mg/mL) and left undisturbed for 1 hour. The cover glass was then washed with water to remove the excess of PDDA. Finally, 100 μL drop of J-aggregates solution was placed over the functionalized glass surface for 1 day. Subsequently, the excess solution was removed with water, and the cover glass was dried under nitrogen flow. The same procedure was followed to deposit the hybrid systems on the glass substrate.

3.2.8 Photostability

Light irradiation experiments were performed to test J-aggregates and plexcitonic systems resistance to photo-oxidation. In those experiments we employed a G2V pico solar simulator, tuning the light wavelength to the range of 650 to 800 nm with 90.4 mW/cm2 power density.

The UV-Vis-NIR spectrum of the light used to probe the photosensitivity of J-aggregates is presented in Figure 3.1.

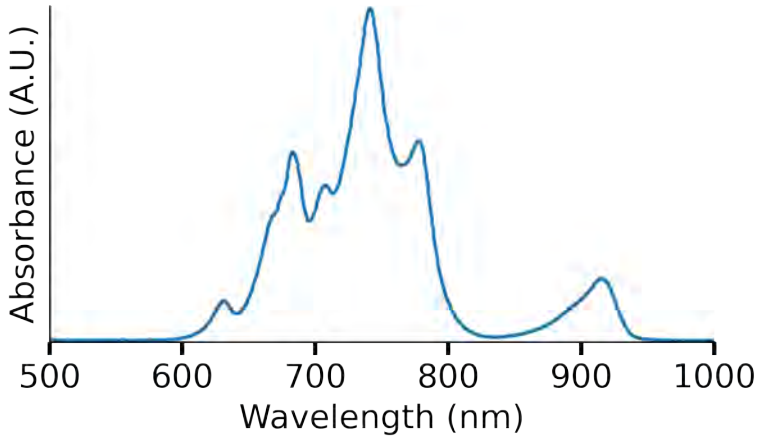

Figure 3.1: The spectrum of incident light from the solar simulator to study the photochemical stability of plexcitonic system.

All photo-stability measurements were performed under ambient conditions.

3.2.9 Characterization

The J-aggregates, bare AuBPs, and hybrid solutions were characterized using a Cary 3500 spectrophotometer to obtain their absorbance (UV-Vis-NIR) spectra. The emission spectra were measured through a Cary Eclipse Fluorescence Spectrophotometer (Agilent Technologies). For the PL decays and Fluorescence Lifetime Imaging Microscopy (FLIM) analysis, we used a time-resolved confocal fluorescence microscope system MicroTime 200 and a laser excitation of 485 nm. The PL response of monomer and J-aggregates were separated using two filters: one centered at 550 nm to obtain just monomeric response and the second at 651 nm for J-aggregates. The PL lifetime values were estimated by fitting the photoluminescence decay curves with SymPhoTime 64 software. It must be pointed out that all these measurements were performed under ambient conditions.

Also, in the case of J-aggregates and hybrid layers, the absorbance spectra allowed us to monitor the molecule's J-aggregation and their response to the NaCl concentration in the original solution. The UV-Vis-NIR response of glass substrates containing J-aggregates and plexcitonic systems was measured using Varian Cary 50 spectrophotometer. Optical images of liquid J-aggregates and hybrid AuBPs-J-aggregates samples were obtained using an optical microscope integrated with a confocal Raman microscopy setup (Alpha300, WITec) from a droplet of a liquid sample deposited on a microscope glass slide. Objectives of 20x (0.4 NA) and 100x (0.8 NA) were used for imaging J-aggregates and hybrids, respectively.

3.3 Optical Characterization

The overall objective of the present chapter is to study the formation of plexcitonic systems and demonstrate the effect of plexcitonic coupling on the photophysical and

photostability of S2275 dye.

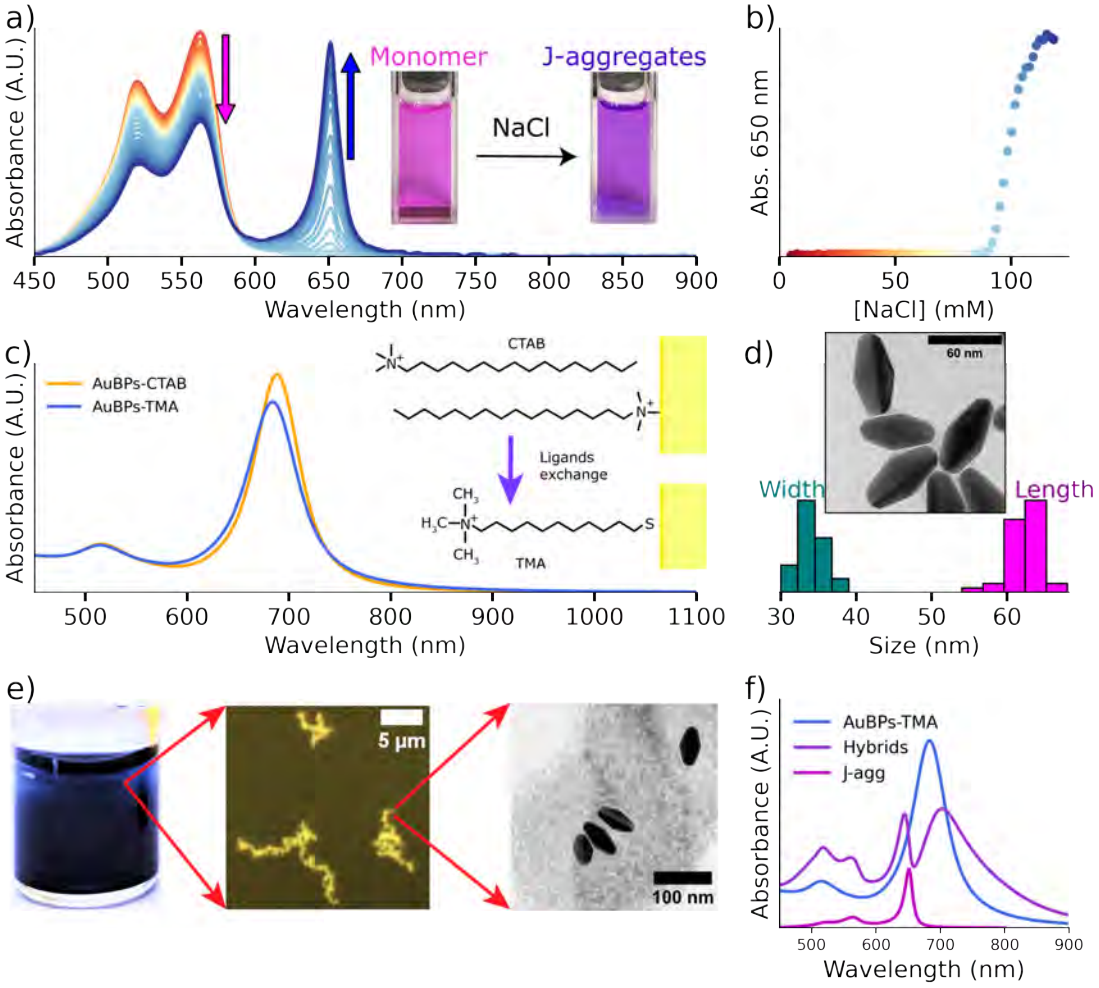

Figure 3.2: J-aggregates and gold nanoparticles characterization. **(a)** J-aggregates formation under NaCl effect, the absorbance spectra show the influence of NaCl molar concentration in the solution in the J-aggregates formation: an increasing J-band response and decreasing monomeric one. **(b)** J-band (651 nm) evolution as a function of NaCl concentration in the solution. **(c)** Ligands exchange: absorbance response of AuBPs in CTAB solution, after synthesis, (orange line) and after TMA functionalization (blue line). The right inset shows the molecules' structure on the gold surface. **(d)** TEM image of synthesized gold nanoparticles and the obtained TEM size statistics. **(e)** Hybrid systems at different scales: solution (macroscopic), optical image (micrometric), and TEM image (nanometric). **(f)** Hybrids formation: absorbance spectra of AuBPs (blue), J-aggregates (magenta), and hybrid systems (purple).

It is well-established that an increase in ionic strength, achieved through the addition of NaCl, induces the self-assembly of S2275 dye molecules into J-aggregates (see Chapter 2) [43, 154]. The UV-Vis-NIR response of S2275 dye shows an intense band in the 400-500 nm region as can be observed in Figure 3.2 **(a)** (red spectrum). Here, as the concentration of NaCl in the solution increases, a distinct band with an absorbance maximum at 651 nm emerges, signifying the J-aggregate response.

Figure 3.2 **(a)** also shows the simultaneous reduction in the UV-Vis-NIR response from dye monomers (indicated by a pink arrow), and growing response from J-aggregates (denoted by a blue arrow) with increasing ionic strength of the solution.

The effect of NaCl on the response of J-aggregates (absorption at 651nm) was analyzed by running two experiments. First, we performed an experiment to observe how the J-band grows by slowly raising the NaCl concentration in the solution. The maximum of the J-band was plotted concerning [NaCl]. A sigmoidal fitting was applied to estimate the minimum NaCl concentration required to obtain J-aggregates of S2275 dye (10 μM): ~97.4 mM. This can be seen in Figure 3.3 **(a)**.

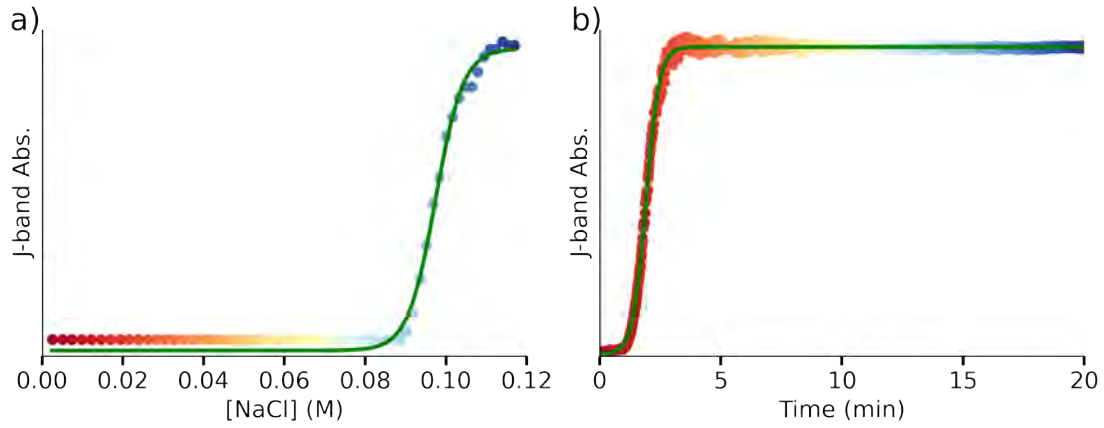

Figure 3.3: J-band evolution with NaCl concentration and time. **(a)** The J-band maxima value (colored dots) shows the J-aggregates formation with increasing NaCl concentration in the solution, and the green line shows the corresponding sigmoidal fitting. **(b)** The J-band evolution with time (colored dots) makes visible the J-aggregates formation with NaCl fixed concentration. The green line corresponds to the sigmoidal fitting.

Then, we inspected the time evolution of the J-band under constant dye (35 μM) and NaCl (100 mM). Using a sigmoidal fitting (Figure 3.3 **(b)**) we were able to determine that J-aggregates require at least 2 minutes to form. Also, this analysis allowed us to estimate J-aggregates' rate of formation: ~ 3.6 min^{-1}.

After demonstrating the formation of J-aggregates, we moved on to the second component of our plexcitonic system, i.e. plasmonic nanoparticles. In the present Chapter, we have chosen AuBPs because they show large optical cross-sections resulting in large local electric field enhancements. Also, they present narrower absorbance line widths, better shape, and size uniformity, and higher refractive index sensitivity than other gold nanoparticle morphologies [155].

Since the present work aims to establish plexcitonic systems using S2275 J-aggregates, it is crucial to select AuBPs with matching spectral properties. With this in mind, we used established literature protocols to synthesize AuBPs with LSPR maxima at 680 nm (see Figure 3.2 **(c)**), closely matching the UV-Vis-NIR maxima of J-aggregates. Figure 3.2 **(d)** shows the TEM images of the prepared AuBPs having an average length of 62 $\pm$ 3 nm and width of 34 $\pm$ 2 nm. Next, the zeta (ζ) potential of CTAB-coated AuBPs was measured to be +52.3 $\pm$ 20 mV,

indicating a high positive surface charge. Since J-aggregates formed using S2275 dyes demonstrate a negative surface charge [42, 156] (discussed vide infra), then, it was hypothesized to exploit electrostatic interactions to govern the formation of the plexcitonic system.

The formation of J-aggregates was tested in CTAB 1 mM solution. A high dye concentration (at least 80 μM) is required to observe the J-band response. For this, we used 10 mM NaCl concentration in the 1 mM CTAB solution. Figure 3.4 **(a)** shows the J-band formation in time after the NaCl addition. It must be remarked that the J-band maxima is reached after around 6.5 hours ($\sim$ 400 min) (Figure 3.4 **(b)**).

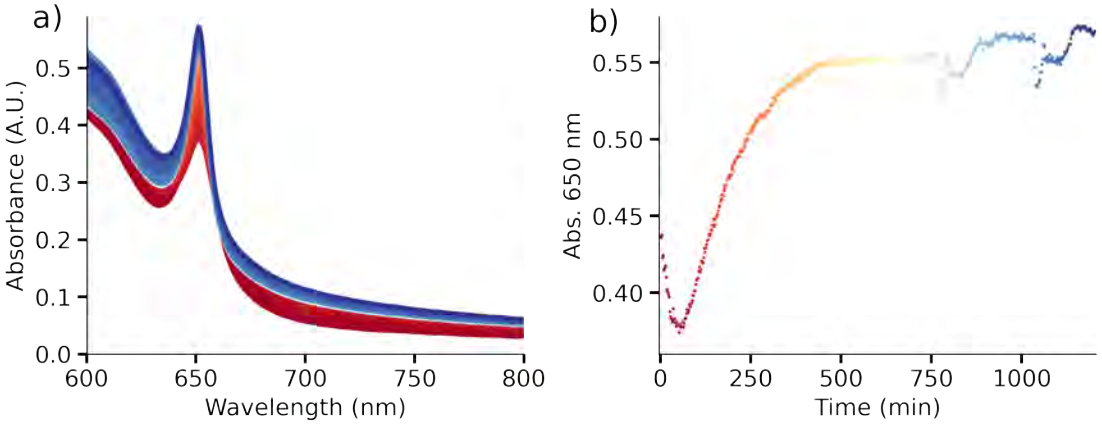

Figure 3.4: J-aggregates in CTAB: **(a)** absorbance spectra evolution of J-aggregates response after the addition of NaCl. The rise of the J-band in **(b)** shows how the maxima progress with time.

Since it is possible to form J-aggregates in a CTAB solution, we proceed with the plexcitonic system formation using AuBPs in CTAB.

Figure 3.5 **(a)** summarizes the response of the J-aggregates in the mixture of AuBPs CTAB 1 mM. The dye concentration was 80 μM in a 2 mL solution of [Au^0] = 0.5 mM AuBPs. Then NaCl was added under magnetic stirring to reach a final concentration of 10 mM. The spectrum taken (orange line) shows no clear signature of J-aggregates, possibly due to their low concentration.

In the second attempt, we decided to add a concentrated solution of AuBPs in CTAB (300 μL) to an aqueous solution of J-aggregates and salt solution to obtain [Au^0] = 0.5 mM and 80 μM dye. Figure 3.5 **(b)** shows the obtained results. In this case, the J-aggregates response can be appreciated superposing the AuBPs spectrum. Particle aggregation was also observed. After washing by centrifugation the system showed a decreased response of J-aggregates. The lack of spectroscopic signatures corresponding to the plexcitonic system indicates the inability of AuBPs-CTAB and J-aggregates to form hybrids. Furthermore, both the J-aggregates and AuBPs could be separated under centrifugation confirming the absence of any plexcitonic system. This absence of interaction is possibly due to the presence of free CTAB micelles in the solution. To circumvent this challenge, a ligand exchange reaction was employed

to replace the native CTAB on the AuBPs surface with positively charged thiolated molecules, TMA.

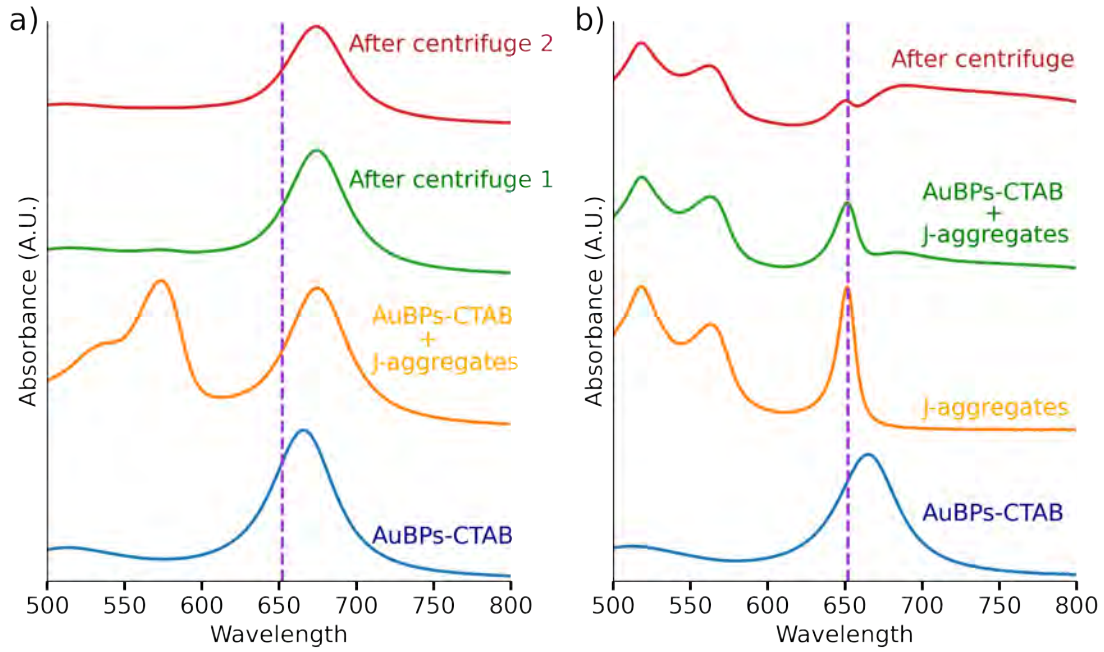

Figure 3.5: Interaction of J-aggregates with AuBPs in CTAB 1 mM. **(a)** To the initial solution containing AuBPs in CTAB(blue line) was added dye resulting in a strong monomeric response (orange line) with no J-band signature as also confirmed by centrifugation (green, red). **(b)** The second possibility to construct the plexcitonic system involved the addition of the AuBPs (blue line) to the solution of preformed J-aggregates (orange line). The spectrum shows the J-aggregates response superposed to the AuBPs (green line). In the purified system spectra (red line) we can appreciate that J-aggregates are in large part removed, indicating that no plexcitonic system was formed. Particle aggregation was also observed.

TMA was chosen due to its strong affinity towards Au through strong Au-S bonds [157], and its ability to impart permanent positive charge to AuBPs through quaternary ammonium headgroups. Figure 3.2 **(c)** demonstrates the UV-Vis-NIR spectra of AuBPs before and after the ligand exchange process. The slight blueshift of the LSPR peak after TMA functionalization [158] is due to the change in the refractive index of the medium from 1.46 (in CTAB) to 1.33 (in water) [159]. Crucially, ζ-potential measurements confirm the positive charge on AuBPs following TMA functionalization (ζ-potential: $+47.9 \pm 19$ mV). Functionalizing AuBPs with TMA circumvents the difficulties due to the presence of free micelles in the solution. Consequently, 35 μM of S2275 was introduced to $[Au^0] = 0.5$ mM AuBP-TMA in the presence of 50 mM NaCl, resulting in the formation of a plexcitonic system. Figure 3.2 **(e)** shows the optical and TEM images of the hybrid system at three different lengthscales: a macroscale view of the solution containing the plexcitonic system, an optical microscope image (microscale) of AuBPs comprising the plexcitonic system, and a TEM image (nanoscale) showcasing the particles embedded in a

net of aggregated dye. Finally, Figure 3.2 **(f)** shows the spectroscopic signatures of plexcitonic system in the UV-Vis-NIR spectrum i.e. appearance of two new peaks (at 651 nm, shown in purple). The origin of this doublet is due to the formation of new light-matter hybrid states [61]. Additionally, Figure 3.2 **(f)** shows the UV-Vis-NIR spectrum of plasmonic (shown in pink) and excitonic (shown in blue) components comprising the plexcitonic system.

Having successfully demonstrated the formation of a plexcitonic system, we aimed to gain quantitative insights into the underlying mechanism guiding its formation. We hypothesize that electrostatic attractions govern the creation of plexcitonic systems. To test this hypothesis more thoroughly, we prepared AuBPs and exchanged the native CTAB with a negatively charged ligand (MUS). Subsequently, with AuBPs-MUS ready, we introduced 70 μL of S2275 dye into a solution comprising [Au^0] = 0.5 mM of AuBPs-MUS and 50 mM NaCl. Over the course of 2h, we monitored the UV-Vis-NIR spectrum of the solution.

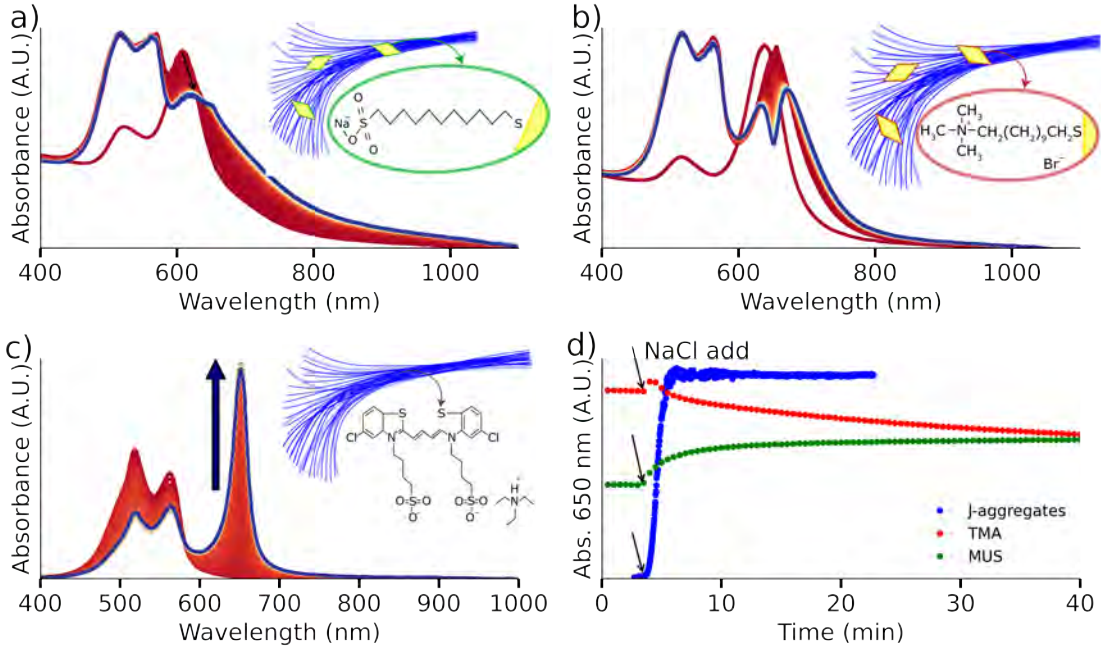

Figure 3.6: J-aggregates formation, their interaction with functionalized gold nanoparticles: with TMA (positive charge) and MUS (negative charge), and J-band evolution for hybrids' solution and J-aggregates solution. **(a)** AuBPs functionalized with MUS evolution after J-aggregates formation; the inset image shows a hypothetical structure of the system: particles over a net from the aggregated dye. **(b)** AuBPs functionalized with TMA evolution after J-aggregates formation, the inset exhibits a hypothetical structure of the obtained plexcitonic system: the aggregated dye forms a net, acting as particle's trap. **(c)** NaCl triggered J-aggregates form in solution after the addition of NaCl: the J-band grows with time, and monomer response decreases; the inset shows a hypothetical structure of aggregated dye elongated morphology. **(d)** The J-band interaction was monitored in three cases: for the J-aggregates alone we obtain the J-band growth, for the plexcitonic system it shows the dip evolution due to the doublet structure, and in the case of MUS functionalized particles, J-band response and particle aggregation is observed.

Notably, no spectroscopic signatures corresponding to the formation of a plexcitonic system were observed even after 2h. The variations in the UV-Vis-NIR spectrum of the system (shown in Figure 3.6 **a**)) are due to the screening of electrostatic repulsions and ultimately, the aggregation of AuBP-MUS at such high salt concentrations [160]. Contrastingly, upon repeating the experiment using AuBPs-TMA (Figure 3.6 **b**)), we observed a redshift after the addition of dye and the almost immediate appearance of a doublet structure in the UV-Vis-NIR spectrum within 3 mins. This dip in the UV-Vis-NIR spectrum, signaling the formation of a plexcitonic system, continued to intensify during the course of 2h. It is important to note that we observed distinctly different kinetics for the formation of J-aggregates in the presence and absence of AuBPs-TMA (Figure 3.6 **c**)), where J-aggregates formed within 2 mins in the absence of AuBPs-TMA.

Furthermore, the conditions for inducing J-aggregate formation in the presence and absence of AuBPs-TMA are distinctly different too. Most notably, the concentration of NaCl to induce the formation of J-aggregates in the absence of AuBPs-TMA is 100 mM (Figure 3.6 **d**)), i.e. twice of what is used during the formation of the plexcitonic system. This reduced need for NaCl indicates the active participation of AuBPs-TMA in the plexcitonic system formation.

On the other hand, the optical image of the J-aggregates solution allows us to observe the elongated morphology formed by the aggregated structures. Figure 3.7 presents the acquired image, where the blue-colored aggregate structures can be observed.

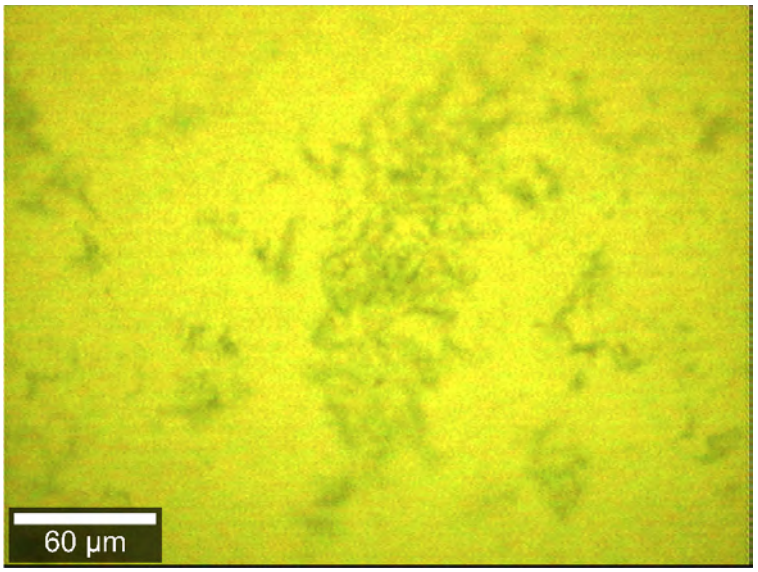

Figure 3.7: Bright field image of a J-aggregates solution.

A layer of J-aggregates was deposited on a previously functionalized glass substrate. After this, we also deposited a layer of hybrid systems.

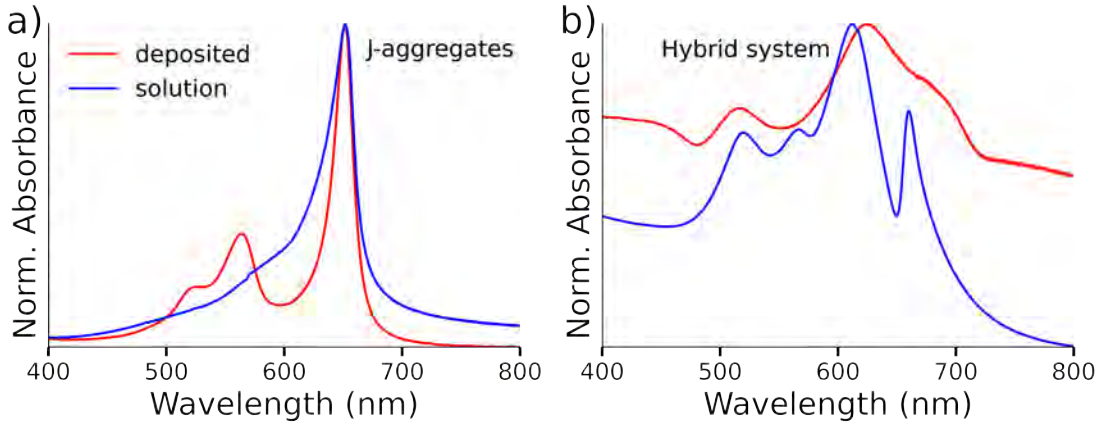

Figure 3.8: **(a)** J-aggregates response in solution and deposited on a glass substrate. The blue line shows the absorbance response measured from the J-aggregates solution, and the red one comes from the deposited layer on a glass substrate. **(b)** Plexcitonic system absorbance response in solution and from a deposited layer. The blue line shows the absorbance response measured from the hybrid systems solution, and the red one presents the spectra obtained from the system-deposited layer on a glass substrate.

The UV-Vis-NIR spectra show the response from the molecular chains in solution (blue line) and when they are deposited in the substrate in Figure 3.8 **(a)**. The J-band presents the same maxima in both cases, but this response is broader for the deposited J-aggregates. To analyze the behavior of a dried sample, we also deposited the hybrid system on a glass substrate. The absorbance response was measured to prove the presence of the plexcitonic system. Figure 3.8 **(b)** shows the UV-vis spectra of the hybrid system in solution (blue line) and the one obtained from the deposited layer (red line). The doublet structure can be appreciated in both spectra, and in the deposited system it is red-shifted due to the media change (from water to air).

3.3.1 System's Coupling Strength

Following the successful demonstration of a plexcitonic system formation, our focus was shifted to studying the nature and strength of interactions within these hybrid structures. With this in mind, we tuned the LSPR in the plasmonic systems comprising the plexcitonic hybrids. Specifically, we prepared six AuBPs samples with LSPR maxima ranging from 612 - 700 nm, and subsequently functionalized them with TMA. This variation in the position of plasmonic LSPR peaks allowed us to easily adjust the tuning in our plexcitonic system. This plasmonic range variation ensures thorough testing of the coupling strength in our plexcitonic system. Figure 3.9 **(a)** demonstrates the successful formation of plexcitonic systems with these six AuBPs having differing spectral mismatches.

The estimation of Ω_R and the coupling strength (g) of the plexcitonic system was done using Equation 1.11. Where Γ_{SP} (0.179 eV) and Γ_{ex} (0.0555 eV) represent the line widths of plasmon and exciton absorbance responses, using established literature

protocols [161]. The obtained coupling strength for this system is 72 meV, and from this estimated value it is possible to evaluate the coupling regime of the plexcitonic system.

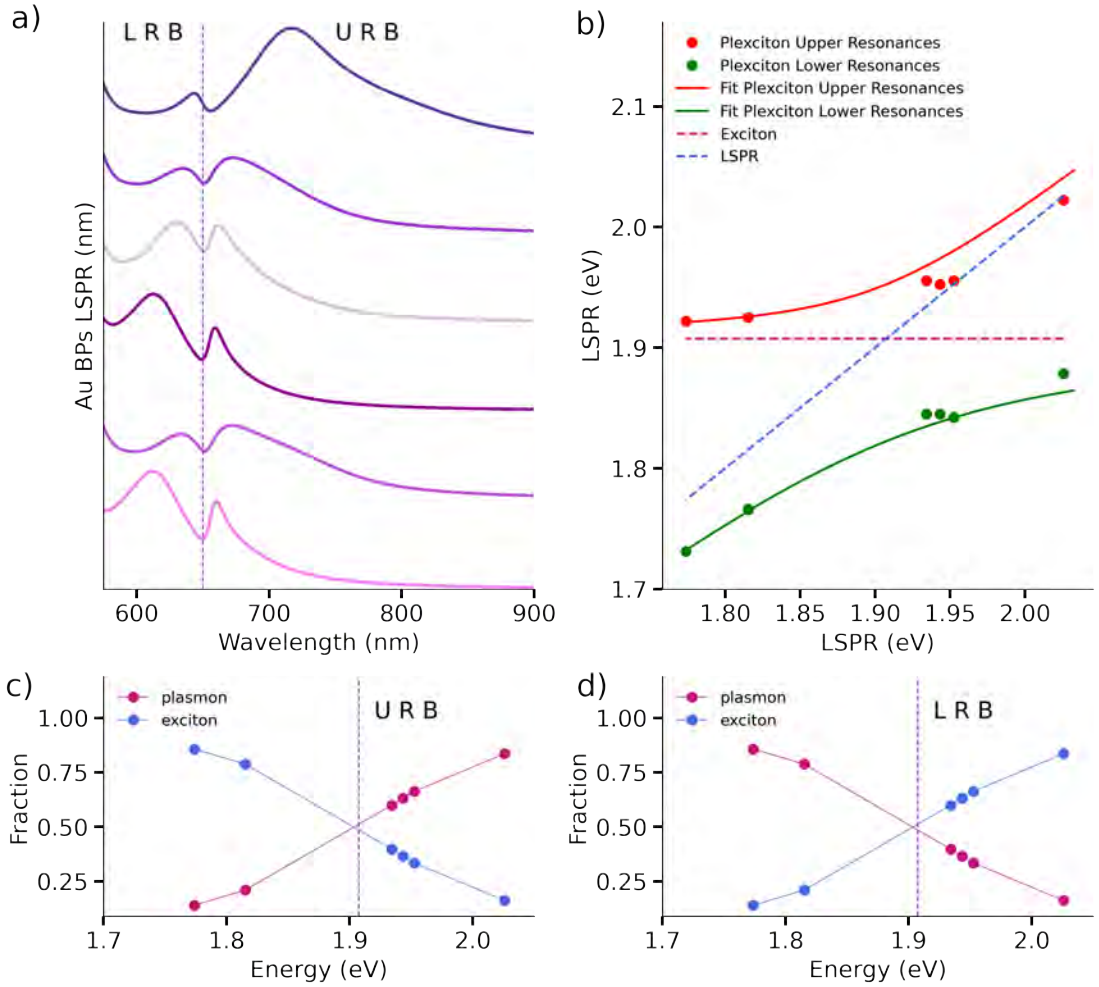

Figure 3.9: Hybrids of functionalized AuBPs with TMA and J-aggregates absorbance characterization. **(a)** The absorbance spectra of the plexcitonic systems show the two branches originated from the two new hybrid states in the system. Spectra are arranged (from top to bottom) in decreasing order of LSPR wavelengths (612 - 700 nm). **(b)** The dispersion curve was obtained by plotting the plexcitonic system's upper (red dots) and lower resonances (green dots) in comparison to the J-aggregates excitonic response (magenta dotted line) and the plasmonic response (blue dotted line). The fitted curves obtained by applying equation (1) to the plexcitonic upper and lower resonances are represented by the red and green continuous lines. **(c)** The estimated Hopfield coefficients show the plasmon (magenta dots) and exciton (blue dots) fractions in the plexcitonic system, according to the estimated Rabi-splitting energy.

The first condition to be satisfied involves the comparison of the coupling strength and the exciton and plasmon decay rates: $g > 1/2(\Gamma_{SP} - \Gamma_{ex})$ [67]. Also, since it is considered that at least one complete Rabi oscillation takes place for the strongly coupled system, the coupling strength should accomplish: $g > 1/4(\Gamma_{SP} + \Gamma_{ex})$ [67].

In our case, both criteria are fulfilled. As well as the relation: $4g^2 \gg \Gamma_{SP}\Gamma_{ex}$ [142, 143, 162, 163].

To conclude this part of the analysis, we present the Hopfield coefficients [164] estimation for the established plexcitonic system: for the Upper Resonance Branch (URB) in Figure 3.9 **(c)**, and the Lower Resonance Branch (LRB) in Figure 3.9 **(d)**. Through these coefficients, it is possible to quantify the exciton and plasmon fractions present in the plexcitonic system as a function of varying the LSPR energies. According to this analysis, the excitonic fraction decreases with transition energy from $\approx$ 83 % to 14 % in the Upper Resonance Branch, and the plasmonic fraction evolves from 16 % to 86 %.

3.3.2 Photoluminescence

One of the primary objectives of this study was to investigate the impact of plexcitonic coupling on the photophysical characteristics of J-aggregates. Some of these molecular chains are characterized by two lifetime components: a fast component interpreted as the result of the excitation quenching by the exciton-exciton-annihilation of the excited J-aggregate and a slow component related to the excited aggregate molecule [165, 166]. This multiexponential PL decay in J-aggregates has its origin in the exciton coherence length in the molecular chain [148, 167].

The PL decay of the S2275 dye was analyzed by estimating the monomeric and J-aggregate lifetimes. A one-exponential fitting was used for monomer decay and a bi-exponential function for J-band decay. We used the same analysis that was applied in Chapter 2 to estimate the lifetimes of monomer and J-aggregates applying Equation 2.9. The obtained values are presented in Table 3.1. The prevalence of τ_1 is shown through A_1 parameter.

Table 3.1: Estimated lifetimes of monomer and J-aggregates dye.

Sample	τ_1 **(ns)**	$\mathbf{A}_1$ (%)	τ_2 **(ns)**	$\mathbf{A}_2$ %	τ_{av} **(ns)**
Monomer	0.3	-	-	-	0.3
J-aggregates	0.2	99.7	2.3	0.3	0.4

The PL intensity decays were measured for the samples presented in this work in solution. Later, a bi-exponential fitting was applied to the obtained decay curves to estimate the lifetime components, using Equation 2.9. In Table 3.2, these results are summarized. These systems have also two lifetime components, where the shorter component τ_1 has a similar value as in pure J-aggregates, but the longer component, given by τ_2, is smaller for plexcitonic systems. Also, the A_2 parameter shows a notably higher value (in almost all samples of plexcitonic systems) in comparison to bare J-aggregates results.

Table 3.2: Estimated lifetimes of hybrid systems and their corresponding coefficients.

AuBPs LSPR (nm)	τ_1 **(ns)**	$\mathbf{A}_1$ (%)	τ_2 **(ns)**	$\mathbf{A}_2$ %	τ_{av} **(ns)**
612	0.3	98.3	1.8	1.7	0.4
635	0.2	98.6	1.3	1.4	0.4
638	0.3	99.6	1.7	0.4	0.4
641	0.3	99.4	1.7	0.6	0.3
683	0.2	97.3	1.5	2.7	0.9
700	0.3	97.4	1.8	2.6	0.5

Specifically, we employed both PL imaging and FLIM techniques for the complete photophysical characterization of our system.

These techniques allowed us to thoroughly assess the impact of plexcitonic coupling on PL intensity, lifetime components, and the spatial distribution of PL lifetimes of J-aggregates. Firstly, the PL response from J-aggregates was analyzed using a dried sample on a glass substrate. The Figure 3.10 **(a)** shows the PL intensity map of the glass substrate coated with J-aggregates. In the colormap, the PL response from J-aggregates is shown in more intense red colors. Next, we extracted the average PL lifetime decay of J-aggregates in the mapped region. Figure 3.10 **(c)** shows the biexponential PL decay belonging to J-aggregates with lifetime components τ_1 = 0.3 ns, and τ_2 = 2.3 ns, as it commonly observed [144, 161, 167]. Employing the FLIM analysis, we visualized the distribution of these lifetimes in the mapped area.

Figure 3.10 **(e)** shows the distribution of both lifetimes, demonstrating the prevalence of the shorter lifetime component. In contrast, we observe a weaker PL response from the plexcitonic system (see Figure 3.10 **(b)**, which was previously observed in gold nanoparticles' interaction with emitters [168, 169]. More specifically, we observe significantly lower photoluminescence intensity in the plexcitonic system (reduced by a factor of 100) compared to J-aggregates, where the PL intensity is around 1000. Finally, we used the PL decay belonging to the plexcitonic systems (shown in Figure 3.10 **(d)**, to map the distribution of lifetimes in the imaged area. We also obtained a biexponential PL decay with lifetime components τ_1 = 0.3 ns, and τ_2 = 1.7 ns. Interestingly, we observe a reduction in the longer lifetime component and an increment in the shorter one. An important point to note here is that the FLIM analysis of the plexcitonic system, depicted in Figure 3.10 **(f)**, reveals comparable amplitudes for both lifetime components.

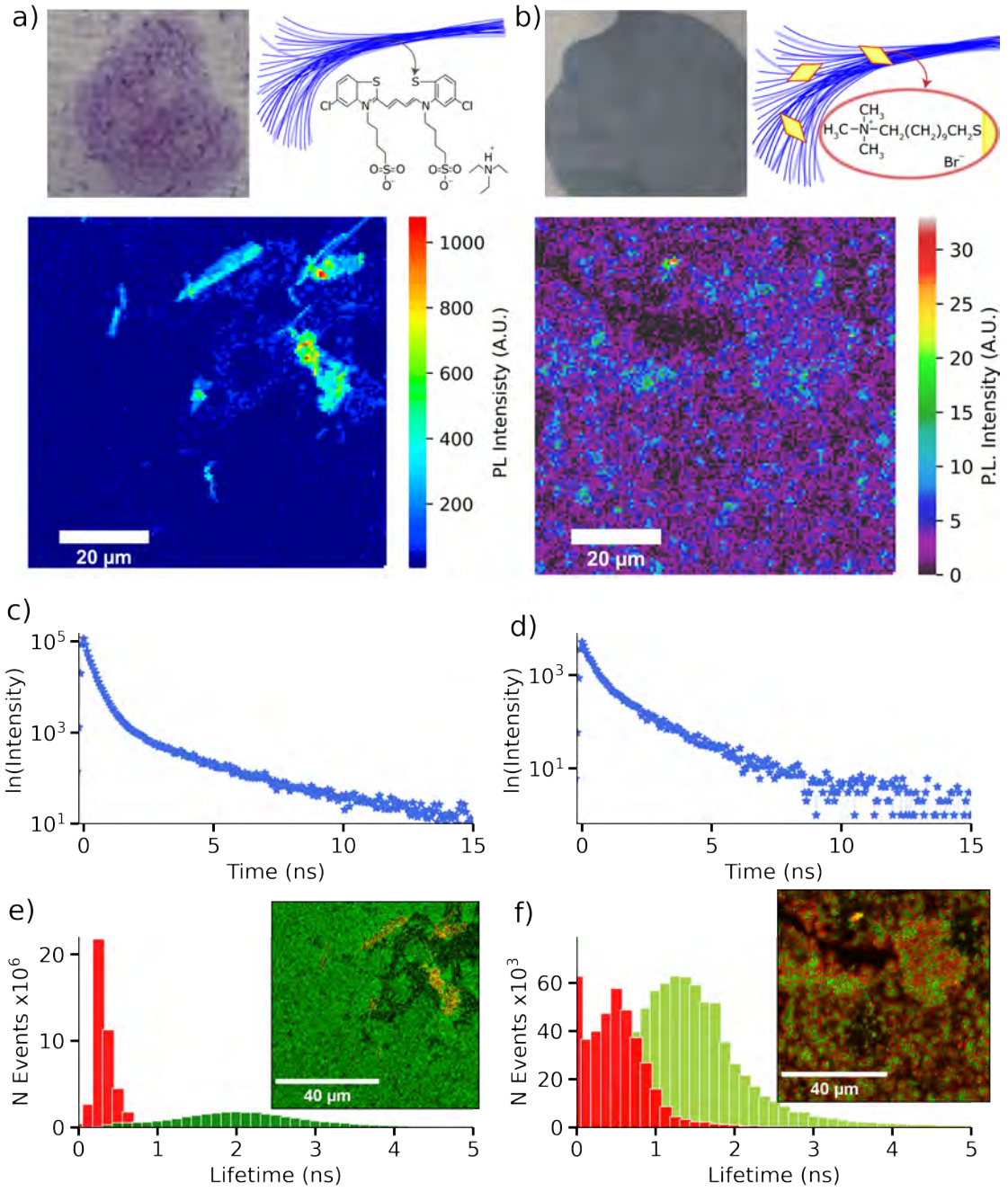

Figure 3.10: Photoluminescence characterization of deposited S2275 J-aggregates and hybrids systems on substrates. **(a)** On the top left side, we have the image of the deposited J-aggregates over a glass substrate and a hypothetical structure of aggregates elongated morphology on the right side. The lower image corresponds to the PL intensity image obtained after scanning an 80 x 80 μm zone of the J-aggregates deposited layer on the glass substrate. **(b)** On the top left side, we have the plexcitonic system layer deposited on a glass substrate and a hypothetical structure of the AuBPs on the aggregates' elongated morphology on the right side. The lower image corresponds to the photoluminescence intensity colormap of the sample. **(c)** The average PL decay was obtained from the photoluminescence colormap for J-aggregates. **(d)** The photoluminescence decay corresponds to the colormap PL intensity for the hybrid system. **(e)** The J-aggregates lifetimes histogram obtained from the FLIM analysis applied to the PL colormap, the inset shows the lifetime colormap according to the estimated lifetime components. **(f)** The plexcitonic system lifetimes histogram was obtained from the FLIM analysis applied to the PL colormap, and the inset image shows the lifetime colormap according to the estimated lifetime components.

The change in lifetime components can be attributed to J-aggregates' chain size variation since a decreased lifetime was reported for an increased J-aggregates length [170]. With this, our hypothesis lies on the J-aggregates' size increase when they interact with particles to explain the measured shorter lifetime. Also, we can point out that J-aggregates formation requires less salt concentration when using gold particle solution so AuBPs could act as aggregation centers for the molecules due to their charge interaction.

3.4 Photostability of plexcitonic system

Finally, we investigate the impact of plexcitonic coupling on the photochemical characteristics of J-aggregates. More specifically, we examine the photodegradation of dye J-aggregates both in the presence and absence of AuBPs under illumination with a solar simulator (wavelength range: 650 - 800 nm).

This examination enables us to secure the stability and conservation of electronic states and optical transitions within hybrid nanostructures, against the influence of the surrounding environment [80]. The variations in the UV-Vis-NIR spectrum of plexcitonic systems under illumination are shown in Figure 3.11 **(a)**.

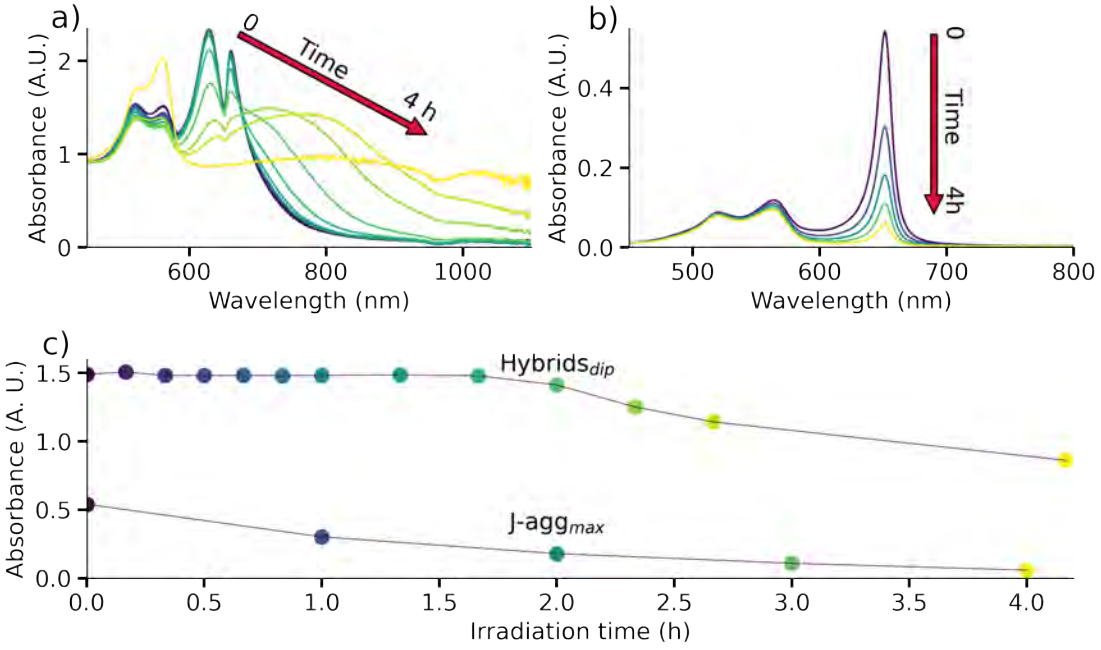

Figure 3.11: Photostability of plexcitonic system. **(a)** The time-dependent UV-Vis-NIR spectra of plexcitonic system show invariance of the spectral signature, followed by a gradual broadening of LSPR due to aggregation. **(b)** The absorbance response of J-aggregates shows degradation under light irradiation. **(c)** Evolution of the dip between the doublet structure of the plexcitonic system to asses the system colloidal stability under light irradiation, and the J-band intensity to quantify the J-aggregates degradation.

Initially, we observe negligible variations in the UV-Vis-NIR response for ∼2h,

after which noticeable redshifts become apparent in the presented spectrum. This redshift is indicative of the aggregation of AuBPs in the solution, as is confirmed by the absence of spectroscopic signals from AuBPs within 4h (yellow spectrum in Figure 3.11 **(a)**).

The J-aggregates spectra evolution can be seen in Figure 3.11 **(b)**, where the J-band decrease is noticeable from the first spectra taken after illumination. This fast intensity reduction in the J-aggregates response with light exposure leads us to conclude that molecules are photodegraded. This drastic difference in the stability of J-aggregates in the presence and absence of AuBPs is clearly demonstrated in Figure 3.11 **(c)**. Here, we track the photostability of the plexcitonic system by monitoring the dip at 651 nm, and the photostability of J-aggregates by monitoring the peak at 651 nm. In this context, J-aggregates demonstrated photostability in the presence of plexcitonic coupling with AuBPs for ∼2h, while 67% of J-aggregates underwent photobleaching in the same time frame. This exceptional resistance to photodegradation of our plexcitonic system (for ∼2h) is directly attributed to colloidal stability given by the AuBPs interaction with J-aggregates. Therefore, we provide compelling evidence that the plexcitonic system exhibits superior photostability when compared to bare J-aggregates. At the same time, the presented system is limited by particle aggregation due to electrostatic interactions between negatively charged dye and positively charged particles. Furthermore, photothermal effects can also come into play under prolonged exposure to light and can contribute to the instability of the system, as seen in Figure 3.11 **(a)** spectra after two hours of light exposure. This issue can be resolved by appropriately varying the surface chemistry of the AuBPs, where the interaction between the NPs and the dye can be established along with enhanced colloidal stability of the plexcitonic system.

3.5 Conclusions

A new plexcitonic system was established using plasmonic nanostructures and J-aggregates. A competitive optical characterization by the system absorbance and PL response in NIR spectral region was performed. Using these data, we were able to determine the Rabi-splitting energy and investigate the coupling regime through the estimated coupling strength parameter. There exist several parameters to distinguish the coupling regimes, and according to most of them, the system interacts in the strong coupling regime. Finally, we investigated the changes in the photophysical and photochemical properties through its photoluminescence response and photodegradation. The presented hybrid systems show improved properties in comparison to bare J-aggregates like enhanced photostability and widened absorption spectral range. The plexcitonic system's emergent properties are due to the two hybrid states' formation; they make these hybrid systems suitable for different applications. In photocatalysis, there are already some coupled systems that have been applied, like AuNPs coupled to a Fabry-Pérot nanocavity that resulted in enhanced water-splitting [136, 171] and water oxidation. [137]

The limitations of these plexcitonic systems are drawn by the nature of their

components. These emerge from the aggregation of the AuBPs in the presence of oppositely charged dye monomer, as well as the sensitivity of the plexcitonic system to photothermal effects. However, we presume that it is possible to overcome these limitations by appropriately varying the surface chemistry of the AuBPs, where the interaction between the NPs and the dye can be established along with enhanced colloidal stability of plexcitonic system.

Chapter 4

Plexcitonic System based on Strongly coupled J-aggregates to CTAB Stabilized Gold Nanoparticles

4.1 Introduction

The light-matter strong coupling interaction results in two new hybrid states [68]. From this, the properties of a strongly coupled system differ from the ones presented by its pure components [82]. Nowadays, several studies have already reported changes in the chemical reactivity [172, 173] and charge electron transport [174, 175] in strongly coupled systems. These modifications presented by the hybrid systems make them more valuable for applications than pure chromophores or semiconductor materials. However, one of the limitations of plexcitonic systems is marked by their stability against hard ambient conditions. Although some studies reported photo-oxidation [82, 176], temperature or pH [80] resistant systems -compared to the pure organic chromophores- these improvements are restricted. Then, a notable improvement in the stability of the J-aggregates-based plexcitonic systems can support the development of plexcitonic systems applications. Here we present an extraordinarily photo-resistant plexcitonic system based on the coupling of J-aggregates and gold particles.

This chapter delves into an examination of the intricate interplay between J-aggregates of JC-1 molecule and CTAB-coated gold plasmonic nanostructures. After analyzing the exciton coherence length of these molecular chains in **Chapter 2**, here we present the investigation of the establishment of a robust plexcitonic system operating within the strong coupling regime based on JC-1 J-aggregates. The characteristics of this nanohybrid system are meticulously scrutinized through the application of spectroscopic methodologies. To begin with, we investigated the

strength of the coupling regime, ascertained through a comprehensive analysis of absorbance and PL responses. Subsequently, an in-depth exploration of the chemical and physical attributes of the hybrid system is conducted, elucidating its potential for prospective applications. Finally, a particular emphasis is placed on the examination of the system's photostability, an interesting feature for future applications in varied domains.

4.2 Materials and Methods:

4.2.1 Materials:

The 5,5',6,6'-Tetrachloro-1,1',3,3'-tetraethyl-imidacarbocyanine iodide, 5,5',6,6'-Tetrachloro-1,1',3,3'-tetraethylbenzimidazolocarbocyanine iodide (JC-1 dye) was purchased from FEW Chemicals. Sodium Hydroxide (NaOH), Cetyltrime-thylammonium Bromide (CTAB), Tetrachloroauric Acid ($HAuCl_4$, $\geq$ 99%), Cetyltrimethylammonium chloride (CTAC), Sodium Borohydride ($NaBH_4$), Silver Nitrate($AgNO_3$), Chloridrich Acid (HCl), and Ascorbic Acid (AA) were purchased from Sigma Aldrich.

4.2.2 Synthesis of AuBPs

AuBPs were synthesized by growing gold pentatwinned seeds [21], as mentioned in Chapter 3. To synthesize the plexcitonic systems, we employed AuBPs solutions of $[Au^0]$ = 0.5mM in CTAB 1 mM.

4.2.3 Hybrid systems

The synthesis of AuNPs/J-aggregates hybrid systems was also carried out in solution. We produced the plexcitonic systems by adding dye (250 μM, 20 μL) to AuBPs-CTAB ($[Au^0]$ = 0.5mM, 2mL). Then, we adjusted the solution pH to 8 using NaOH (0.1M, 20 μL), all this under magnetic stirring to initiate J-aggregates formation. Within 10 mins, we observed the spectroscopic signatures indicating the formation of a plexcitonic system, i.e. formation of a doublet structure near the exciton and plasmon resonance position (595 nm).

4.2.4 Characterization:

The J-aggregates, CTAB-coated AuBPs, and hybrid solutions were characterized using a Cary 3500 spectrophotometer to obtain their UV-Vis-NIR spectra. Furthermore, the emission spectra were measured using a Cary Eclipse Fluorescence Spectrophotometer (Agilent Technologies). For the PL decay analysis, we used a time-resolved confocal fluorescence microscope system MicroTime 200 and a laser excitation of 485 nm. The PL lifetime values were estimated by fitting the photoluminescence decay curves with SymPhoTime 64 software. In addition, the hybrid systems PL was measured using a 532 nm laser in a confocal Raman microscopy setup (Alpha300, WITec) from a droplet of a liquid sample deposited on a microscope glass slide.

Finally, for photo-stability experiments, we employed a Type AAA solar simulator (pico, G2V), with a spectral range of 650 to 800 nm and a power density of 90.4 mW/cm^2. All photostability measurements were performed under ambient conditions.

4.3 Optical Characterization:

The study of the hybrid system properties was carried out by applying different characterization methods, such as UV-vis-NIR spectra, time-resolved spectroscopy, and PL spectra.

4.3.1 Absorbance

The UV-vis-NIR spectra allowed us to monitor the spectral signature of the pure J-aggregates, the AuBPs colloidal solution, and the hybrid systems once they are formed. In this latter step, we can appreciate the evidence of the resulting doublet feature (see Figure 4.1). The spectrum depicted by the purple line shows the distinct response of the newly formed hybrid states. This hybrid response comes after adding the J-aggregates solution (pink spectrum) to the AuBPs solution (blue spectrum).

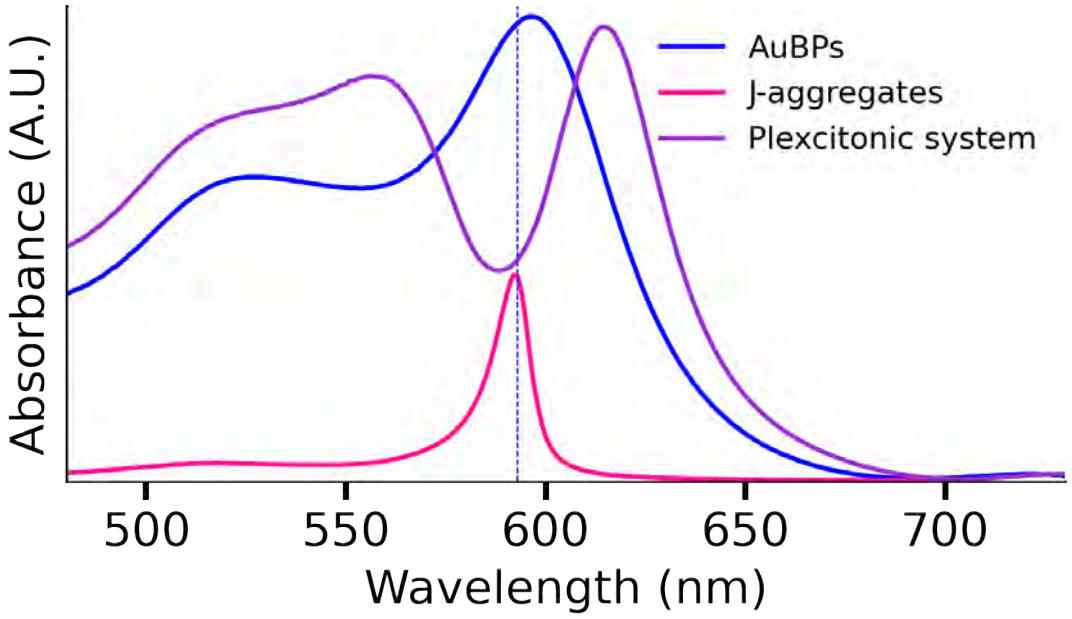

Figure 4.1: Plexcitonic system based on JC-1 J-aggregates and AuBPs. The initial components were analyzed through UV-Vis NIR spectra: J-aggregates in aqueous solution (pink line), CTAB-coated AuBPs (blue line), and the already established plexcitonic system (violet line). The blue dashed line shows the absorption maximum of J-band in J-aggregates.

The salient advantage of this specific hybrid system (AuBPs/J-aggregates) resides in its compatibility with JC-1, where the interaction between J-aggregates

and gold nanostructures occurs without compromising the colloidal stability of the latter [80, 109, 161]. JC-1 molecule's J-aggregates are known to penetrate cell membranes [177] and from this, we hypothesize a similar interaction helps to build up this plexcitonic system. Hence, in our system, they permeate the CTAB bilayer, once form molecular chains at pH 8, a behavior akin to that observed in cellular environments [41, 94]. Once J-aggregates (pink line) are formed into the AuBPs solution (blue line), the ensuing coupling response becomes discernible through the distinctive spectral signatures of the emergent hybrid states (purple line), as illustrated in Figure 4.1.

A comprehensive investigation into the detuning influence was undertaken upon successfully establishing the methodology for generating plexcitonic systems incorporating J-aggregates. The examination of the plasmon-exciton detuning in plexcitonic systems serves as a systematic approach to assess the system's response across specific wavelengths, aiming to achieve optimal performance. This methodology is widely employed for the meticulous customization of the plexcitonic system's optical properties, fine-tuning energy transfer processes, ensuring system stability, facilitating the design of functional devices, and deepening our fundamental comprehension of these hybrid systems. Here we utilize gold bipyramids with different spectral positions of the localized surface plasmon resonance bands (see Appendix Figure 5.7). The longitudinal plasmon bands encompass a spectral range from 560 to 960 nm, specifically targeted for this analysis. The spectral signature of the formed plexcitonic systems' is shown in Figure 4.2, providing a visual representation of the impact of LSPR detuning from the excitonic response. The variations in the hybrid states are intricately correlated with the progressive alteration and detuning of the LSPR, thereby affording valuable insights into the interplay between J-aggregates excitons and Au nanostructures plasmons in the creation of plexcitonic entities.

It is appreciable that the most tuned samples (587, 596 nm) present a symmetric doublet spectral signature. This response comes from the hybrid states formation within the plexcitonic system and it is related to the mixed light and matter nature of these new states, which will be discussed further once we analyze its coupling strength.

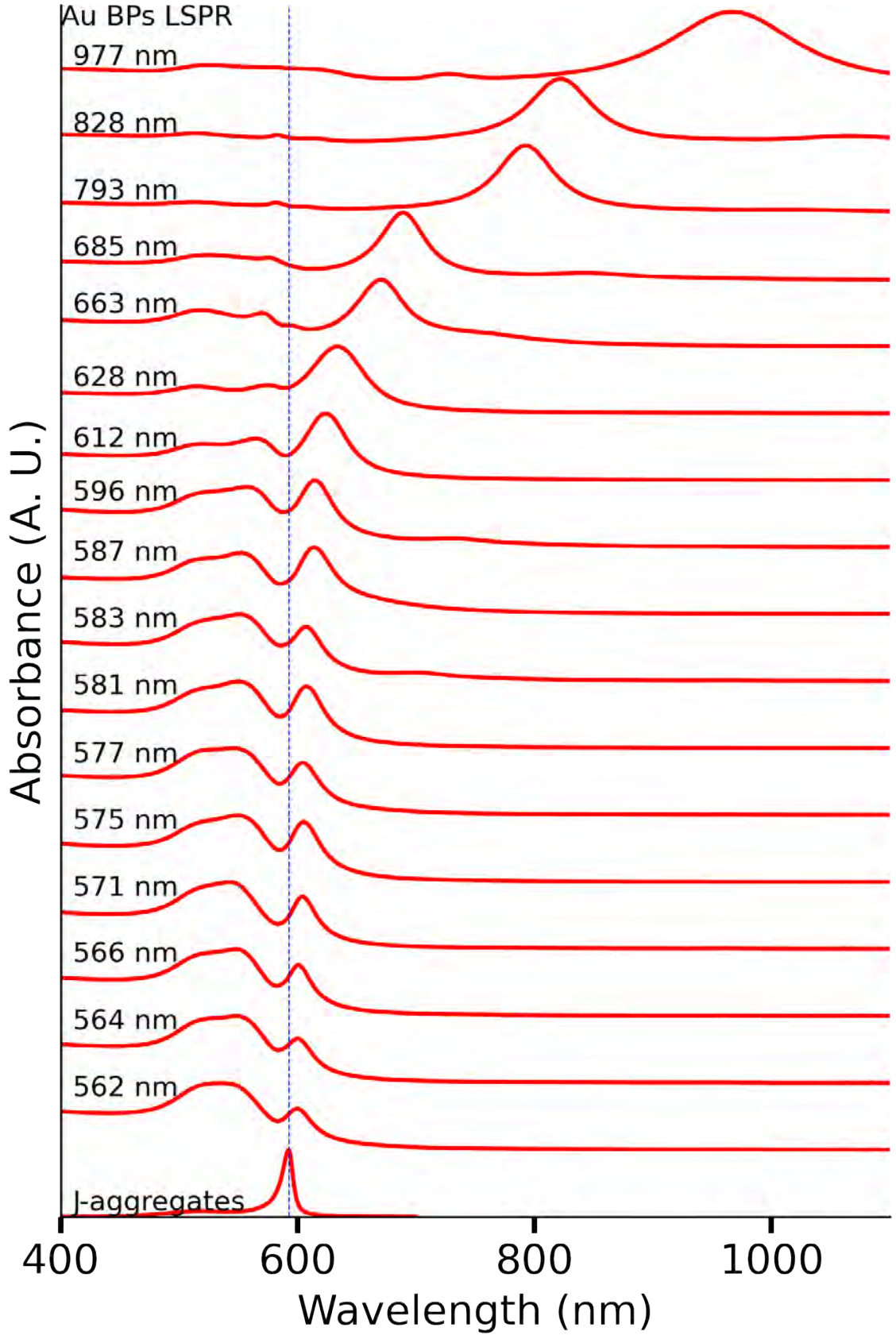

Figure 4.2: Effect of detuning in plexcitonic systems. Gold bipyramids with plasmon bands ranging from 560 to 980 nm were coupled to J-aggregates to examine the coupling in the plexcitonic systems. The blue dotted line represents the J-aggregates response.

4.3.1.1 System's Coupling Strength.

The analysis of the coupling strength nature of the plasmon-exciton interactions within these hybrid structures can be carried out using the previously obtained absorbance spectra, as it was conducted in Chapter 3, applying the model described in Chapter 1 in section 1.6. The variation of the plasmonic response allows an easy adjustment of the tuning in our plexcitonic system and ensures testing the coupling regime.

In the context of this study, focused on plasmon mode detuning, a pronounced anti-crossing behavior within the extinction spectrum is discerned. This distinctive spectral feature arises from the hybridization of modes within the plexcitonic system. The observed anti-crossing phenomenon furnishes valuable insights that enable subsequent estimations of the coupling strength parameter (g), particularly tailored to the characteristics of this specific plexcitonic system. This nuanced analysis not only enhances our understanding of the interplay between plasmon and exciton modes but also provides quantifiable parameters for characterizing and predicting the behavior of such hybrid systems. The dispersion curve formed by the Plexciton Upper and Lower Resonances showing the anti-crossing behavior allows the application of Equation 1.10 (see Figure 4.3 **(a)**). From this analysis, we were able to estimate the Rabi splitting energy for this hybrid system: $\Omega_R = 270$ meV. We used $\Gamma_{SP} = 0.148$ and $\Gamma_{ex} = 0.037$ eV for the line widths of the plasmon and exciton from their UV-Vis-NIR spectra.

Using the estimated Ω_R value, we can also calculate the system's coupling strength g using Equation 1.11. The result of this is $g = 191$ meV. This value grants the evaluation of the system coupling strength regime by using the criteria presented in **Chapter 3**. The first one implies $g > 1/2(\Gamma_{SP} - \Gamma_{ex})$ [67]. Then, we considered $g > 1/4(\Gamma_{SP} + \Gamma_{ex})$ [67]. In the analyzed system, both criteria are fulfilled. And also the relation: $4g^2 \gg \Gamma_{SP}\Gamma_{ex}$ [142, 143, 162, 163], therefore ensuring that our system is in the strong coupling regime.

On the other hand, the cooperative factor (C) defined in Equation 4.1 can be used to determine the spectral response of the resonant hybrid system, and $C > 1$ [67] can be taken as an extra guideline to distinguish a hybrid system coupling regime.

$$C = \frac{g^2}{\Gamma_{SP}\Gamma_{ex}} \tag{4.1}$$

For the g value previously obtained the cooperative factor results as $C = 5.9$, probing that our system is in the strong coupling regime. Then, taking into account all the criteria applied for this hybrid system based on AuBPs/J-aggregates we can conclude that we established a strongly coupled system in the colloidal phase.

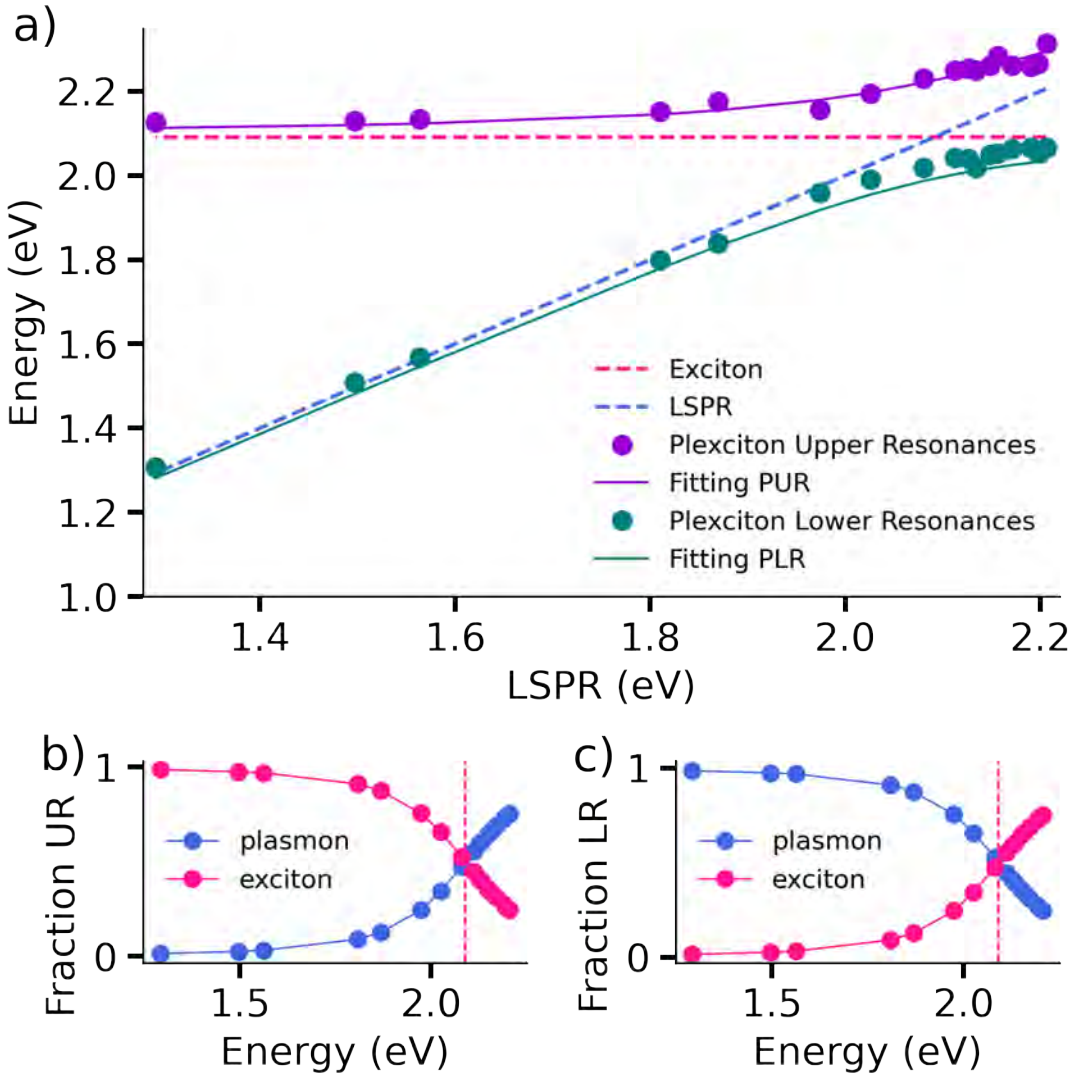

Figure 4.3: Analysis of hybrid system comprising AuBPs and J-aggregates. **(a)** The dispersion curve was obtained by plotting the plexcitonic system's upper (purple dots) and lower resonances (green dots) showing the anti-crossing behavior limited by the J-aggregates excitonic response (pink dotted line) and the plasmonic response (blue dotted line). The fitted curves obtained by applying equation 1.10 to the plexcitonic upper and lower resonances are represented by the continuous lines. **(b)** The estimated Hopfield coefficients for the Upper Resonances and **(c)** the Lower Resonances in the hybrid system. These coefficients show the plasmonic (blue dots) and exciton (pink dots) fractions in the plexcitonic system, according to the estimated Rabi-splitting energy.

However, the coupling strength value can be also estimated using the coupled harmonic oscillator theoretical model. Here, the modeled responses from the uncoupled plasmonic structure and the coupled system were obtained through Equation 1.9 (see Figure 4.4).

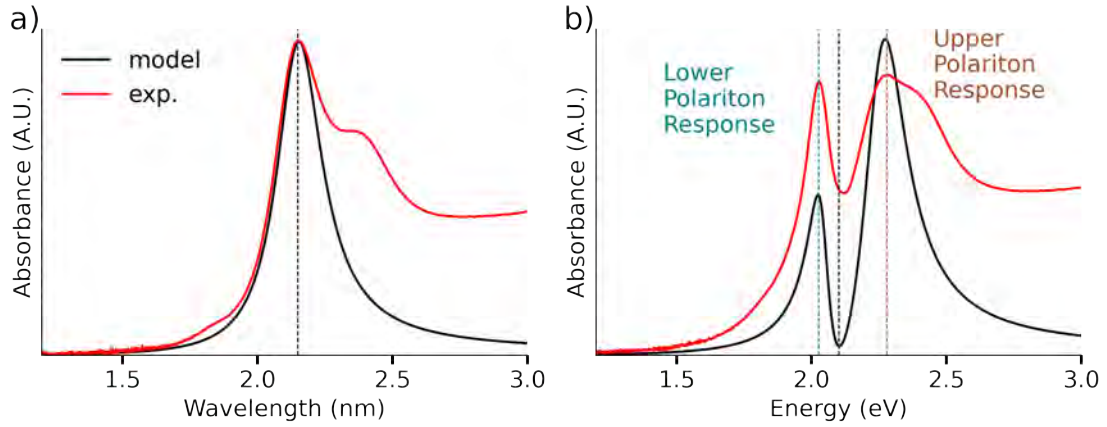

Figure 4.4: Analysis of the plexcitonic system using a theoretical model. **(a)** The theoretical plasmonic response (black line) was simulated using the measured spectral optical response of the AuBPs (red line). **(b)** Then, the theoretical plexcitonic response (black line) was obtained using the experimental AuBPs spectral parameters and the new hybrid states response (red line).

The modeled optical response of the hybrid systems depends on ω_{ex} (2.1 eV), ω_{SP} (2.07 eV), Γ_{ex} (0.03 eV) and Γ_{SP} (0.18 eV), all these parameters were obtained from the experimental characterization (absorbance spectra presented in the previous section). First, we recreated the longitudinal plasmonic resonance tuned with the exciton (at 599 nm). Then, we proceeded to model the plexcitonic system absorbance response using the required parameters. To obtain an accurate value of the coupling strength we looked for a matching spectral signature building an algorithm that allows us to vary the parameter g. Here, we took into account the coupling strength obtained from the dispersion curves analysis as a guide for the applied g values in the model (ranging between 100 and 250 meV). Then, to choose the most accurate modeled spectrum (according to g) we mainly considered the hybrid states' response position: the resulting modeled spectra should have an identical doublet feature as the experimental one. From this, the estimated g is 190 meV, agreeing with the value obtained from the dispersion curve analysis. We should remark that the transversal plasmonic mode was neglected in our calculations to simplify this problem, however, we cannot expect a more identical spectral response.

4.3.2 Photoluminescence

The impact of strong coupling was also evaluated by analyzing the PL response of the plexcitonic systems. These spectra were measured using laser excitation at 532 nm. From observing the spectrum of a resonantly tuned sample (LSPR = 599 nm) it is noticeable a doublet signature as the one obtained in the absorbance spectra, also we can remark the presence of the characteristic Surface-Enhanced Raman Scattering (SERS) peaks of JC-1 J-aggregates at 561.6, 567, 568.7, 573.1, 574.7, 578, 591.3, and 610.3 nm [161] (see Figure 4.5, purple line). Some previous studies of JC-1 J-aggregates-based plexcitonic systems already reported these Raman peaks' presence in similar measurements where the gold NPs coupling enhances this response [178,

179]. However, in our work the clear spectral signature (doublet feature) of the hybrid states is remarkable.

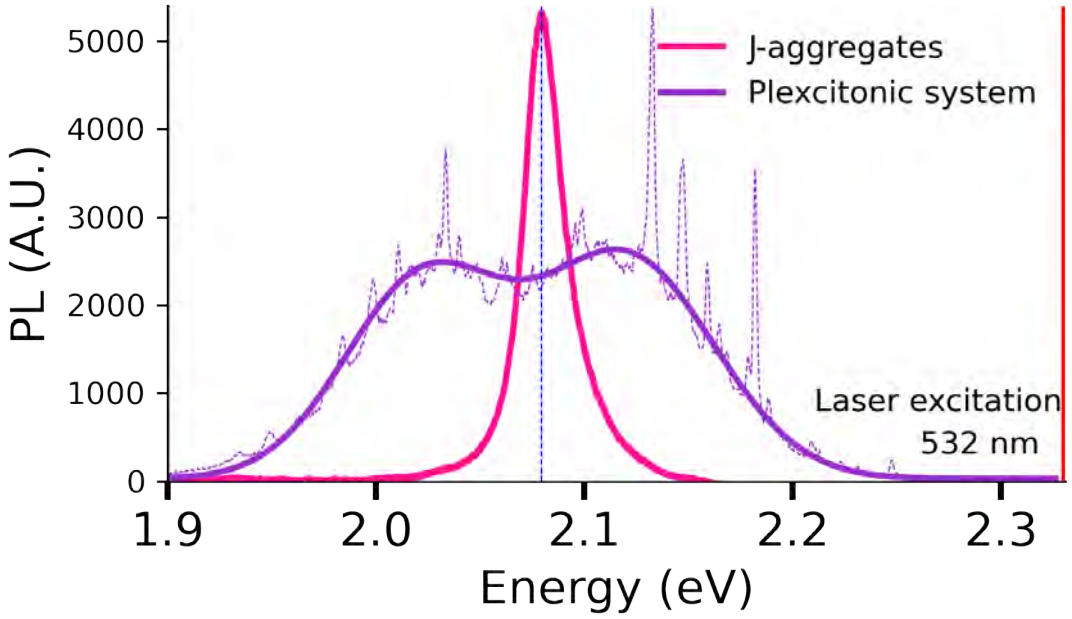

Figure 4.5: PL response of a plexcitonic system based on JC-1 J-aggregates and AuBPs. J-aggregates (pink line) and the plexcitonic system (violet line) photoluminescence spectra were measured. The blue dashed line shows the J-aggregates maxima. Sharp peaks superimposed on the PL spectra are the Raman signals enhanced by the SERS mechanisms.

The spectrum of JC-1 J-aggregates PL (pink line) measured using the same setup, resulted in a single peak highly intense response in comparison with the acquired hybrid system's signal.

The effect of plasmon detuning from the excitonic transition response can provide further information about the PL signal collected from hybrid structures. In Figure 4.6 **(a)** we present the acquired PL spectra of plexcitonic systems where the plasmonic band varies from 560 to 670 nm. Within these spectra, the doublet feature signature is present only for the samples with LSPR between 580 and 620 nm. However, in all of these spectra, the characteristic JC-1 J-aggregates Raman features are superimposed. Herein, the most detuned samples (LSPR 560 nm and 670 nm) show less intense Raman responses, the most affected by this intensity decrease are the ones located at energies lower than 2.1 eV.

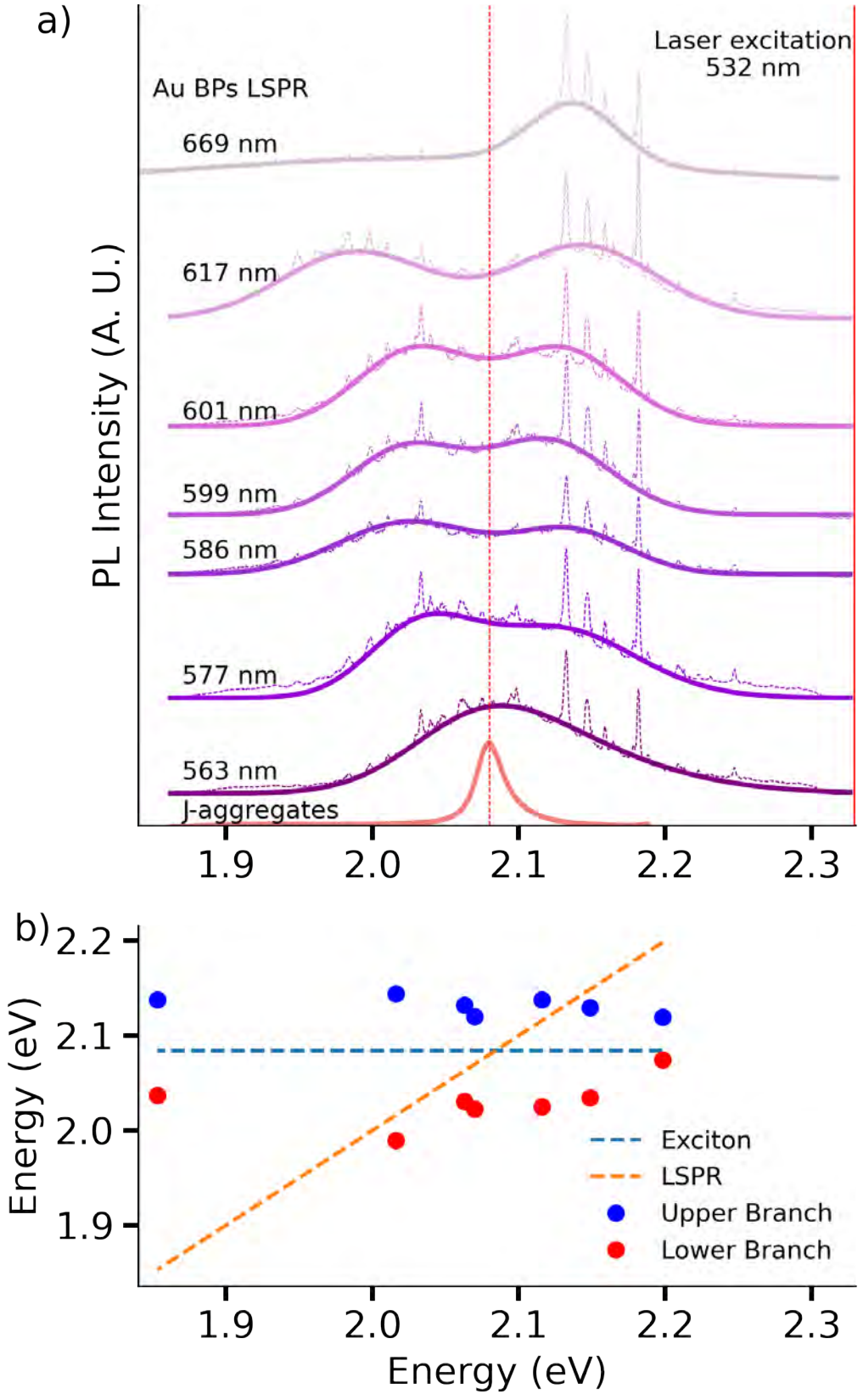

Figure 4.6: PL response analysis of detuned plexcitonic systems. **(a)** Plexcitonic systems formed with AuBPs with plasmonic response ranging from 560 to 680 nm. **(b)** Dispersion curve from the upper and lower branches of the PL spectra obtained from hybrid systems formed varying the plasmonic response.

The effect of SERS in strongly coupled plasmon-exciton-based systems has been already reported. In general, since this phenomenon comes from the plasmonic-surface interaction, it is attributed to excitation enhancement or the lightning rod effect. Specifically in plexcitonic systems, this pronounced Raman signal has been related to chemical enhancement coming from the hybrid states [180].

The behavior of the hybrids' doublet feature in PL differs from the presented in the absorbance dispersion (see Figure 4.6 **(b)**). In this case, we cannot apply Equation 1.10 to estimate Ω_R because there is no PL response from the AuBPs. In addition, as can be seen in Figure 4.6 **(b)** the PL signal does not follow the anti-crossing behavior limited by the exciton (blue dotted lines) and plasmon response (orange dotted lines). It seems to follow a different trend. Due to this limitation, we will apply a different model to reach the coupling strength value.

4.3.2.1 System's Coupling Strength.

Since it is possible to analyze the PL response to estimate the coupling strength using a modeled response, we will analyze further the measured PL spectra of the plexcitonic systems to estimate g. However, to reach this goal we require the Heisenber-Langevin equations due to the quantum nature of spontaneous emission. The solution to this problem takes into account the emitter in its excited state and a zero plasmon mode as initial conditions [67] and is presented in Equation 4.2.

$$I_{ex}(\omega) = \frac{\Gamma_{exc}}{2\pi} \left| \frac{1/2\Gamma_{SP} - i(\omega - \omega_{SP})}{[1/4(\Gamma_{SP} + \Gamma_{ex}) + i/2(\omega_{SP} - \omega_{ex}) - i(\omega - \omega_{SP})]^2 + \Omega_R^2} \right|^2 \tag{4.2}$$

For this analysis, the measured PL spectrum of the J-aggregates (pink spectrum in Figure 4.5) was used to extract the values of ω_{ex} and Γ_{ex} which were later applied in Equation 4.2. However, since the PL plasmonic parameters were not available for our system we varied them until we obtained the best fit for the modeled response to the experimental spectrum (see Figure 4.7). For this fit, we considered mainly the doublet feature position in the experimental response, then the model should present upper and lower polariton responses at the same energy as the measured spectrum. Finally, it is important to remark that in this analysis to estimate g we used a plexcitonic system conformed by AuBPs tuned to the excitonic system (LSPR = 599 nm).

The obtained Ω_R was 240 meV, and applying Equation 1.11 we can estimate the g value as 160 meV. We can notice that the values of the coupling strength and Rabi energy are 30 meV lower than the ones estimated in the absorbance spectra analysis. This discrepancy was previously reported in some colloidal nanohybrid systems where the PL signal could be measured [178, 179] but also for individual nanohybrid systems [181], where the double feature in the PL response is notably narrower. In this latter study, the origin of the doublet signature is questioned due to the lower splitting energy in PL than in absorbance and the proximity of the Upper Polariton Branch to the exciton response.

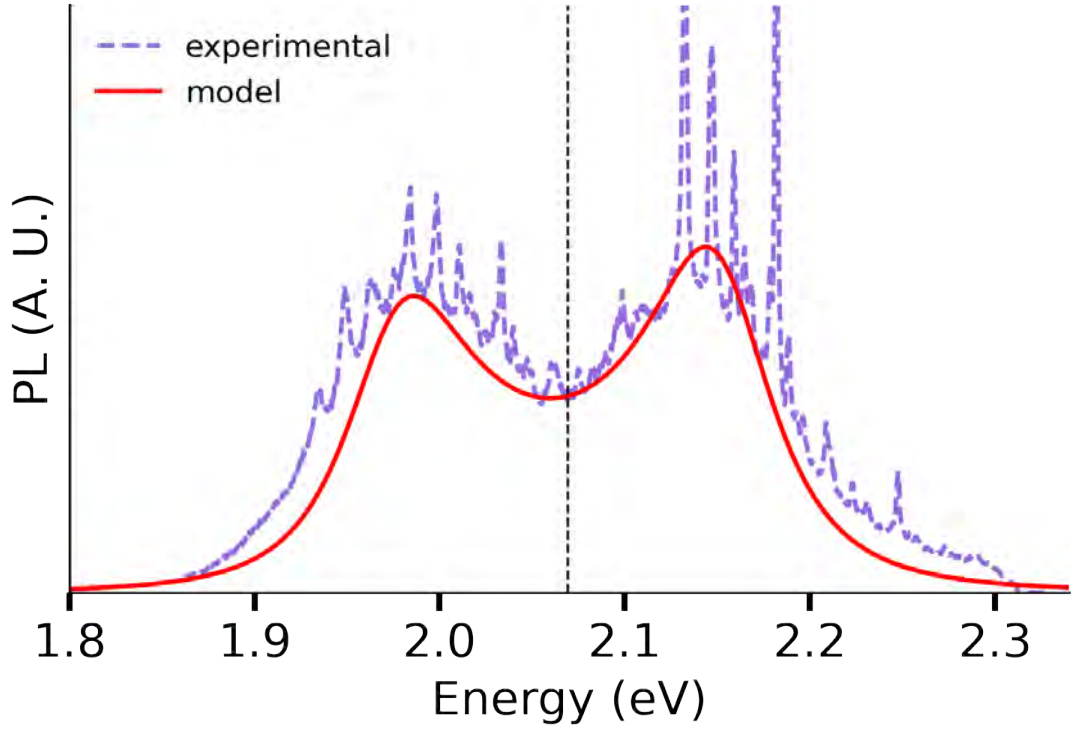

Figure 4.7: Tuned plexcitonic system based on JC-1 J-aggregates and AuBPs. The measured photoluminescence spectrum of the plexcitonic (purple line) and the estimated spectrum (red line) are presented. The black dashed line shows the PL J-aggregates maxima.

The interaction of the molecular chains with the NPs, where the coupling of N J-aggregates with one AuBP results in two bright states ($|+\rangle$ and $|-\rangle$) and N-1 dark states, corresponding to the uncoupled molecules [181]. From this, Zengin et al. concluded that the observed PL Upper Branch comes from the uncoupled molecules in the hybrid system and not from a hybrid state. Also, they take into account the value of the Rabi-splitting energy of their plexcitonic system, which is higher than the one reported from vibrational modes of the J-aggregates (TDBC dye, $\omega_{vib}^{J} < 180$ meV). On the other hand, for the Lower Branch in PL, it is claimed that corresponds to the emission of the lower polariton state [182]. In the case of our system, we do not observe an Upper Polariton Branch response close to the J-aggregates PL. In fact, this response given by a dotted line in Figure 4.7 is in the middle of the doublet feature. Then, we consider that further characterization is required to conclude about the origin of this doublet feature. The first step could be to analyze the value of Ω_R from the PL and absorbance responses of the sample at low temperatures. Also, the position of the doublet feature at low temperatures could give more details about the origin of this signal.

4.3.2.2 Time Resolved Photoluminescence

The photophysical characterization of this hybrid system was extended through the analysis of the PL signal decay, to assess the impact of strong coupling on PL intensity and lifetime components. The analyzed colloidal system showed a noticeable modification in its PL intensity compared to pure J-aggregates response, as can be observed in Figure 4.8.

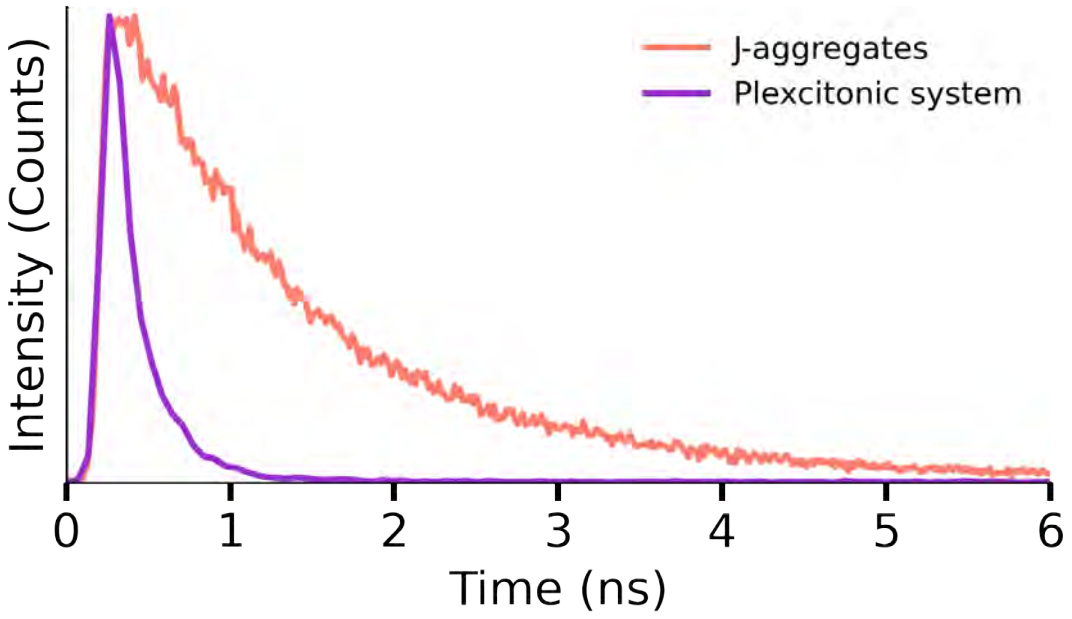

Figure 4.8: JC-1 J-aggregates and tuned plexcitonic system PL decay curves. J-aggregates (orange line) and the plexcitonic system (violet line) normalized decays show the influence of strong coupling in the PL response.

The PL decays belonging to J-aggregates (orange spectrum) and the plexcitonic system (purple spectrum) were analyzed using a double exponential fitting because the cyanine dye J-aggregates generally present two lifetimes components [165, 166, 176]. We applied here the same analysis done in Chapter 3 for hybrid systems to estimate the lifetime values. From this analysis, we obtained $\tau_1 = 0.2$ ns and $\tau_2 = 1$ ns for the tuned and strongly coupled system (LSPR = 599 nm). This change in the PL decay is commonly observed in gold nanoparticle coupled systems. Where the coupling interaction modifies the local photonic mode density and consequently radiative decay rate increases [168, 169, 176].

Accordingly, the hybrid system lifetimes are also affected by the plasmon-exciton detuning. This influence can be seen in table 4.1, where the detuned samples show a larger second component and fractional amplitude (A_2), and also a higher lifetime (τ_{av}) concerning the tuned sample. This difference is mainly remarkable in the τ_{av} values.

Table 4.1: Estimated lifetimes of plexcitonic systems.

AuBPs LSPR (nm)	τ_1 **(ns)**	$\mathbf{A}_1$ (%)	τ_2 **(ns)**	$\mathbf{A}_2$ %	τ_{av} **(ns)**
586	0.2	94.4	1.5	5.6	0.6
599	0.2	97.5	1	2.5	0.3
669	0.2	93	2	7	0.9

4.4 Photostability of hybrid system

After the exploration of the photophysical properties of this plexcitonic system, in this section, we will focus our study on probing the system's photostability.

The influence of the coupling strength in the systems' photobleaching is remarkable, mainly the strong coupling impact in chemical reactions [172]. This molecular chemical reaction change was already reported in strongly coupled molecules with plasmonic resonators [82, 173, 176]. Also, we explored this property for a different plexcitonic system in Chapter 3 section 3.4 where our analyzed nanohybrid system shows a notable increase in photostability compared to bare J-aggregates. This result motivated us to test the influence of the strong coupling interaction in the JC-1/AuBPs-based system.

The JC-1 J-aggregates photodegradation was tested using light irradiation in the range between 420 to 790 nm (see Figure 4.9).

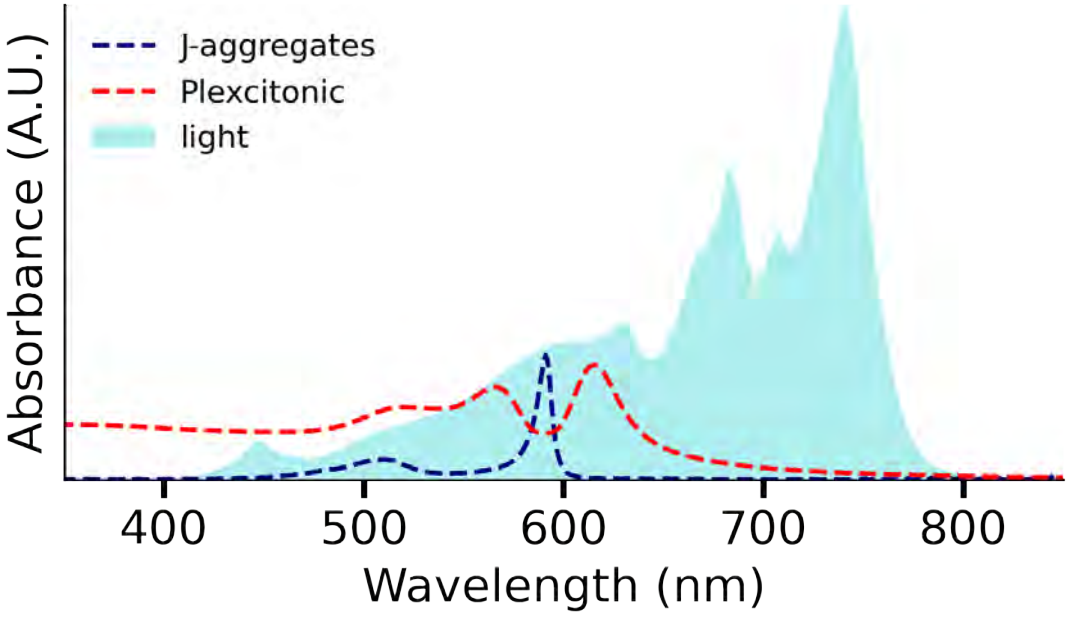

Figure 4.9: Used light spectrum to irradiate JC-1 J-aggregates and plexcitonic systems from the G2V pico solar simulator.

The J-aggregates solution was irradiated for 1 hour, and after this time the UV-

vis spectrum showed no signature of J-aggregates. From the absence of spectral signatures of the molecules, we concluded that they were photodegraded due to light exposure. The JC-1 sensitivity to light was already reported [80], showing this fast photobleaching. To quantify the pure J-aggregates fast degradation we used the J-band intensity in the absorbance response (see Figure 4.10).

On the other hand, once the plexcitonic system is established we also expose the nanohybrids in solution to light from the solar simulator. We took the spectrum after 5 and 24 hours and no remarkable change in the solution spectrum could be noticed. It should be noted that after 11 hours of light irradiation, it was possible to perceive some particle aggregation just in the spot hit by light. Here a blue stain was noticed, but the system was easily recovered after gently shaking the containing cuvette.

The spectrum shown in Figure 4.10 **(a)** (yellow line) corresponds to the measurement done after 24 hours and after mixing the sample. The dip between the hybrid system's new states' response (pink arrow at 590 nm) was monitored to evaluate the system evolution after light irradiation, see part **(b)**.

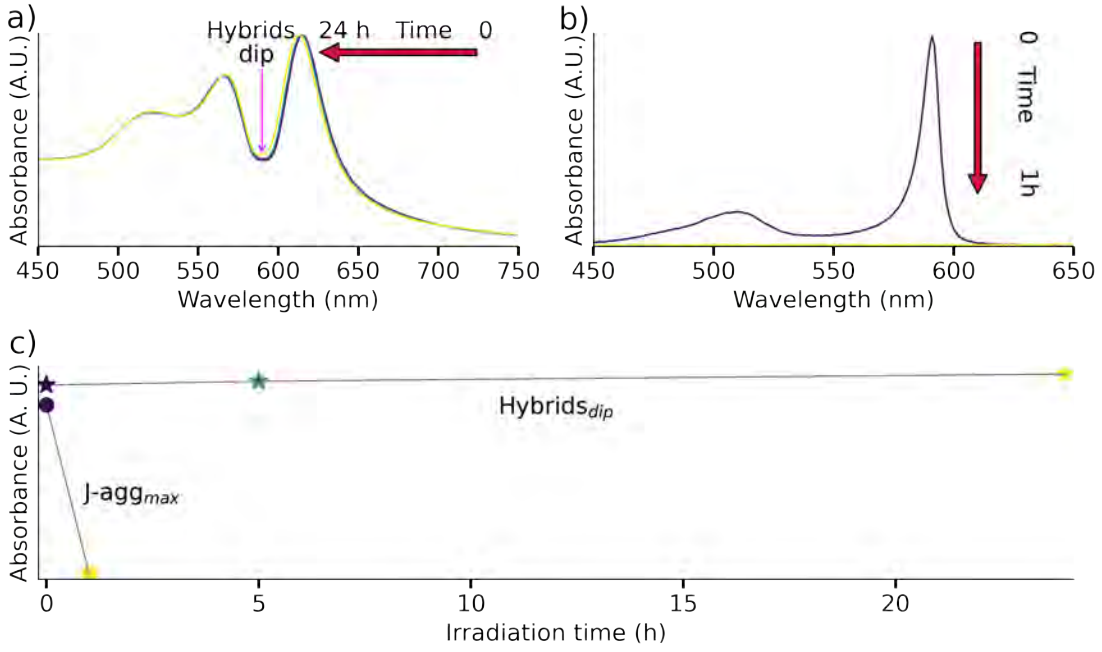

Figure 4.10: Photostability of JC-1 J-aggregates and plexcitonic system. **(a)** The time-dependent UV-Vis-NIR spectra of plexcitonic system show no appreciable change in the spectral signature. **(b)** The absorbance response of J-aggregates presents fast degradation under light irradiation, after 1 hour there is no J-aggregates response. **(c)** Evolution of the dip between the doublet structure of the plexcitonic system (pink arrow) to asses the system colloidal stability under light irradiation, and the J-band intensity to quantify the J-aggregates degradation.

This experiment confirmed the system photostability acquired from AuBPs coupling in J-aggregates-based hybrids. The photodegradation-resistance enhancement

was also noted for the S2275-based hybrid system (2 hours), however, the JC-1-based system shows longer-time photostability (24 hours). The explanation for this difference can come from the influence of the system's coupling strength. Battulga et al. presented a study about the photobleaching suppression in strongly coupled systems and the enhancement dependence on the Rabi splitting energy. The study demonstrates that the population of the triplet state in the hybrid system is inhibited due to the relaxation pathways modification from the strong coupling interaction [82].

4.5 Conclusions

In this Chapter, the elucidation of the established plexcitonic system, featuring the synergy of J-aggregates and gold nanoparticles, has been an undertaking marked by notable findings. The analysis of Rabi splitting energy, derived from both absorbance and PL responses, unequivocally substantiates the characterization of this system as strongly coupled. This distinctive feature underscores the efficient interaction between the molecular excitations and plasmonic resonances, affirming the system's potential for applications in quantum optics and light-matter interactions. Furthermore, the observed attributes of immense photostability increase the suitability of this nanohybrid system as a candidate for photocatalytic applications. All these characteristics not only ensure the sustained integrity of the plexcitonic system under external perturbations but also open avenues for its dynamic adaptation in response to varying environmental conditions, thereby broadening its applicability across diverse technological domains. These results motivated further exploration and analysis of this system's chemical properties, which will be discussed in the following chapter.

Chapter 5

Switchable Plexcitonic System

5.1 Introduction

As mentioned in the introductory chapter (Chapter 1), the examination of reversible plexcitonic systems assumes paramount significance due to its profound implications for both fundamental research and prospective applications across diverse disciplines. The salient rationales underpinning the exploration of reversible plexcitonic systems are rooted in the potential attainment of dynamic control over system properties. This prospect extends to optical modulation, information processing, and biological and chemical sensing, thereby contributing significantly to comprehending fundamental processes within hybrid systems. The reversibility inherent in plexcitonic systems facilitates control over the coupling strength, wherein a comprehensive understanding of the interplay between exciton and plasmon becomes pivotal for tailoring optical characteristics.

The properties of plexcitonic systems based on JC-1 J-aggregates coupled to plasmonic nanoparticles have been previously studied using different nanostructures such as gold nanorods [80, 178], Au nanostars [179], or silver triangles [81]. One of the advantages of these systems comes from the experimental feasibility of their formation, that is, the need for increased pH of the solution and their stability in CTAB solution, as shown in Chapter 2. They also present colloidal steadiness at high pH values, temperature fluctuations, and light irradiance [80]. Specifically, this system's photostability was analyzed and discussed in Chapter 4 Such stability indicates that the molecular system of aggregates close to the metal surface is rigid and well protected by the surrounding surfactant bilayer. Therefore, the plexcitonic system based on JC-1 aggregates can be considered a good candidate for sensing applications.

In the present Chapter, a question was posed whether one can revert the strong coupling in the plexcitonic system based on gold nanoparticles and JC-1 upon vary-

ing the pH conditions of the medium. We found that such reversibility under limiting high and low pH conditions is indeed possible. It was observed that the reversible formation of strong coupling can be performed cyclically and measured optically by UV-Vis-NIR and PL, as well as modeled computationally. We also detected Raman features in the PL spectra of the switchable plexcitonic system, which showed different intensities under weak and strong coupling. We show that the strong coupling regime enlarges Raman spectral spread. Finally, we proposed a preliminary chemical mechanism behind the pH-dependent switchable character of the plexcitonic system, shedding light on the possible origin of fast coupling and slow decoupling processes.

5.2 Switchable J-aggregates

It has been shown in the previous chapters that JC-1 forms J-aggregates upon the increase of pH. Once at high pH (> 8), the J-aggregates are present in the solution. We subjected the J-aggregates solution to pH variation. The schematic representation of such an experiment is presented in Figure 5.1 **(a)**.

First, the pH value is increased to 8 (to induce the formation of J-aggregates), then the pH value is decreased to 2 followed by its recovery back to 8. The system response to the pH change was monitored by absorbance and PL techniques. The absorbance of the J-band reaches its maximum with the addition of NaOH (pH=8) (red spectrum in Figure 5.1 **(b)**). One can also observe the presence of the monomeric response at 500 nm. Once HCl is added, the J-band along with the monomeric band disappears (blue spectrum in Figure 5.1 **(b)**). There is also a color change of the solution from pink (J-aggregates, solution pH > 8) to clear one (no J-aggregates, low pH). The band can be recovered, bringing back the value of pH to 8. This reversible behavior was tested for 3 cycles, meaning that it was possible to recover the J-aggregates response as long as the pH exceeds 8 (Figure 5.1 **(c)**). Also, the cyclic formation of J-aggregates under changing pH was confirmed by photoluminescence measurements, showing a similar trend (Figure 5.1 **(d, e)**).

In a control experiment, we performed the reversible formation of J-aggregates in the presence of cationic surfactant (CTAB, 1 mM). The surfactant is needed to sustain the colloidal stability of plasmonic nanoparticles during the formation of plexcitonic systems, being 1 mM (critical micelle concentration) the lower concentration threshold below which the colloidal stability can be compromised. Therefore, it was necessary to perform experiments of reversible J-aggregate formation in the presence of surfactant to exclude any potential interference of the surfactant micelles with the JC-1 dye. We observed that CTAB did not affect the reversible aggregation of molecular dye upon pH change (see Appendix Figure 5.7).

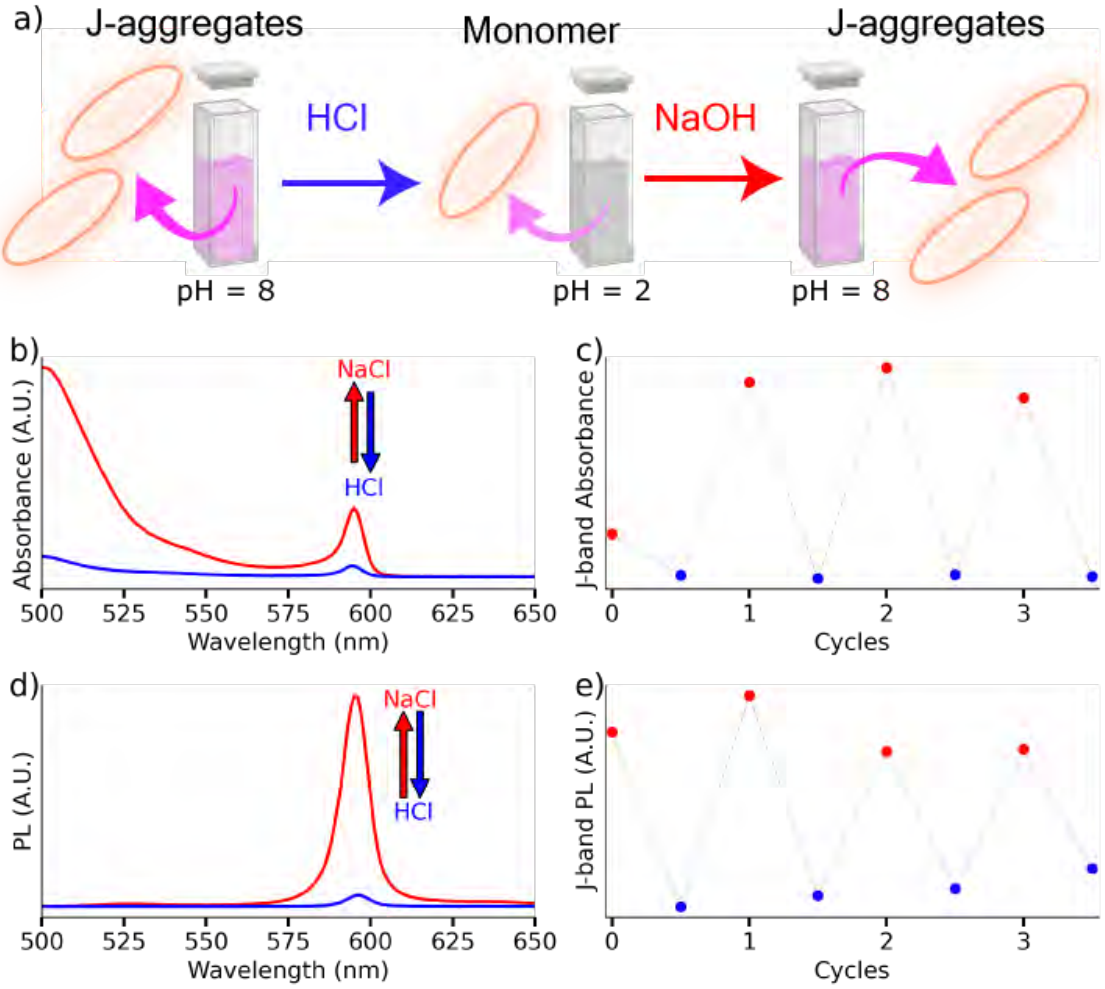

Figure 5.1: Reversible J-aggregates under pH change. **(a)** Schematic representation of experimental procedure of reversible J-aggregates, showing the experiment workflow. We begin with a J-aggregates solution (pH=8), then HCl is added (pH=2), and no J-band response is observed. Finally, if we increase the solution pH we obtain again a J-aggregates solution. **(b)** Absorbance spectra of J-C1 in water solution at pH=8 (red) and pH=2 (blue). **(c)** Cyclic change of J-band intensity at high and low pH. **(d)** PL spectra of J-C1 in water solution at pH=8 (red) and pH=2 (blue). **(e)** Cyclic change of emission band intensity at high and low pH.

5.3 Gold Bipyramids

Gold bipyramids were synthesized through an established protocol. [21] The experimental conditions were adjusted to obtain nanoparticles with the maximum of LSPR located at 599 nm, that is, to match the J-band location of JC-1 aggregates (See Figure 5.1)). The characterization by the transmission electron microscopy revealed that the width of the as prepared nanoparticles was 25 ± 4 nm and the length was 50 ± 3 nm (Figure 5.2). The as-prepared nanoparticles were washed 2 times to remove the excess reagents (e.g., ascorbic acid, silver ions) and stored in a CTAB solution of 1mM concentration. It was mandatory to test the colloidal stability of

nanoparticles under both low pH (HCl 10 mM) and high pH (NaOH 11 mM). It was observed that the storage of gold bipyramids (CTAB 1mM) for several days at high and low pH did not affect their colloidal stability, as witnessed by the invariance of extinction spectra (compare blue and red spectra in Figure 5.2 **(a)**).

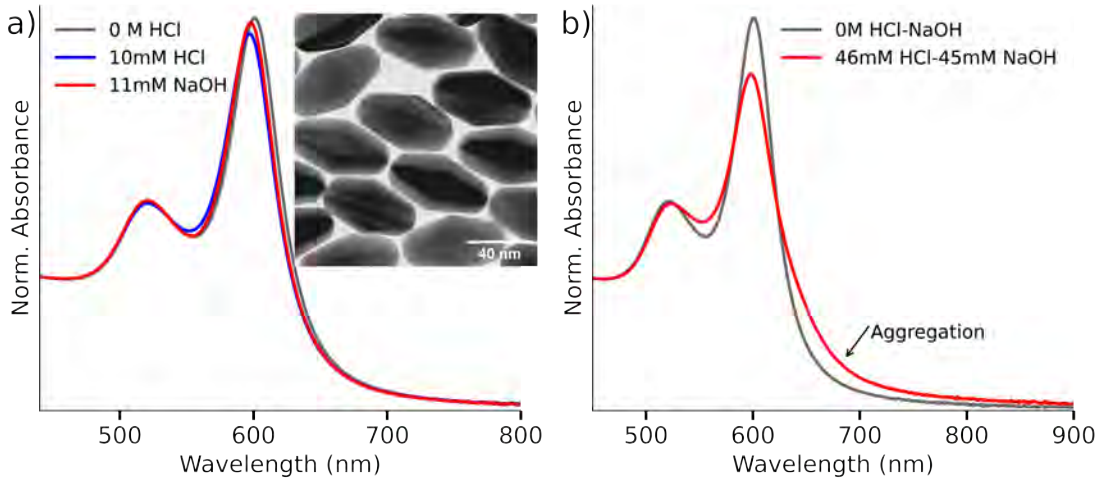

Figure 5.2: Effect of pH change on the colloidal stability of AuBPs in 1 mM CTAB. **(a)** Absorbance spectra of initial solution (gray line) after HCl addition (blue line) and subsequent NaOH addition (red line). Inset: a typical TEM of as-prepared gold bipyramids. **(b)** Effects of cyclic addition of HCl and NaOH on colloidal stability of gold bipyramids. Initial spectra (gray line) and after cyclic addition of HCl and NaOH (orange dotted lines) until reaching final concentration of HCl and NaOH, 46 mM and 45 mM, respectively (red spectra).

To study the change of strong coupling for several pH cycles, one needs to expose the nanoparticles to even more harsh pH conditions. That is, the switchable plexcitonic system involves the accumulation of ions in the solution, as there is no washing step after bringing the system to a given pH. Such an accumulation of ions can increase the ionic strength of the solution which can eventually compromise the colloidal stability of the plexcitonic system, thus making the optical characterization impossible. In further control experiments, the sample of nanoparticles was subjected to more severe pH conditions. In doing so, HCl and NaOH were added cyclically to reach a total concentration that corresponds to three cycles of switchable J-aggregates, as shown in Figure 5.1 **(b)**. No significant aggregation was noticed, even after storing the solution for several days (Figure 5.2 **(b)**). However, at pH $>$ 12, the slight asymmetry of the plasmon band emerged. The appearance of the shoulder at 680 nm suggests a small aggregation. Worth mentioning is the fact that such aggregation appears at times much longer than the time of a typical experiment for switchable plexcitonic. Therefore, it was concluded that the imposed cyclically changing experimental conditions are not affecting the colloidal stability of gold nanoparticles.

5.4 Switchable plexcitonic system

Since the most convenient mean to evaluate experimentally the switchable character of the plexcitonic system is spectroscopy we calculated theoretical spectra for two limiting scenarios of the coupled and uncoupled system by using Equation 1.9 and input parameters of ω_{exc} = 2.1 eV, ω_{SP} = 2.07 eV, Γ_{exc} = 0.03 eV, Γ_{SP} = 0.18 eV obtained from experimental samples in Chapter 4.

Figure 5.3 **(a)** shows the resulting spectra of coupled and uncoupled systems, that will serve as a guide while evaluating switchable plexcitonic systems. The experimental realization of a switchable plexcitonic system was similar to that of J-aggregates. The solution of the as-prepared plexcitonic system was washed to remove the excess of J-aggregates and JC-1 monomers and redispersed in 1 mM CTAB at pH 10. Then, the addition of HCl caused a progressive decrease in pH from 10 to 2. The sample was stored for 6 to 8 hours. Later, the pH of the solution was increased back to 10. The process was repeated three times. The absorbance spectra at pH are shown in Figure 5.3 **(b)**, indicating the disappearance of the splitting in the absorbance spectra at lower pH. Importantly, the spectral features could be recovered. One can notice that the band intensity in the coupled system (pH 10) decreases with each cycle. This can be associated with decreasing colloidal stability of the sample due to increasing ionic strength in the solution. This issue can be avoided by washing the sample after the re-coupling process, to eliminate the salt or by using different compatible compounds to trigger the pH change.

The speed of coupling and decoupling processes is dramatically different. We performed time-dependent absorbance measurements for both scenarios: the addition of either HCl or NaOH. The spectra were recorded in 0.5 s time intervals for the coupling phase and 1 minute for decoupling. The original plasmon band of gold bipyramids splits into two bands within 10 seconds after the addition of NaOH (Figure 5.3 **(d)**). Thus, the formation of a coupled system is practically immediate. To decouple the system, however, one needs nearly 8 hours to fully merge both bands after the addition of HCl (Figure 5.3 **(c)**). Such a difference in kinetics suggests that two processes follow different pathways which is discussed in detail below. Nevertheless, the transition from one state to another is highly reproducible, as shown by initial and final spectra for both scenarios (Figure 5.3 **(e,f)**).

A rather slow dynamics of decoupling upon lowering the pH opens up the possibility of estimating the change of coupling strength over time for different concentrations of acid. We monitored the spectral change every 20 minutes for 6 hours for acid concentrations ranging from 5 to 200 mM. Figure 5.4 **(a)** shows the typical evolution of spectra with time for [HCl] = 8 mM. It is visible that two branches merge 2 hours after injection of acid.

To calculate the coupling strength for each spectrum we used the known experimental parameters (ω_{exc} = 2.1 eV, ω_{SP} = 2.07 eV, Γ_{exc} = 0.03 eV, Γ_{SP} = 0.18 eV) using Equation 1.9. The only unknown parameter in this equation is coupling strength, g.

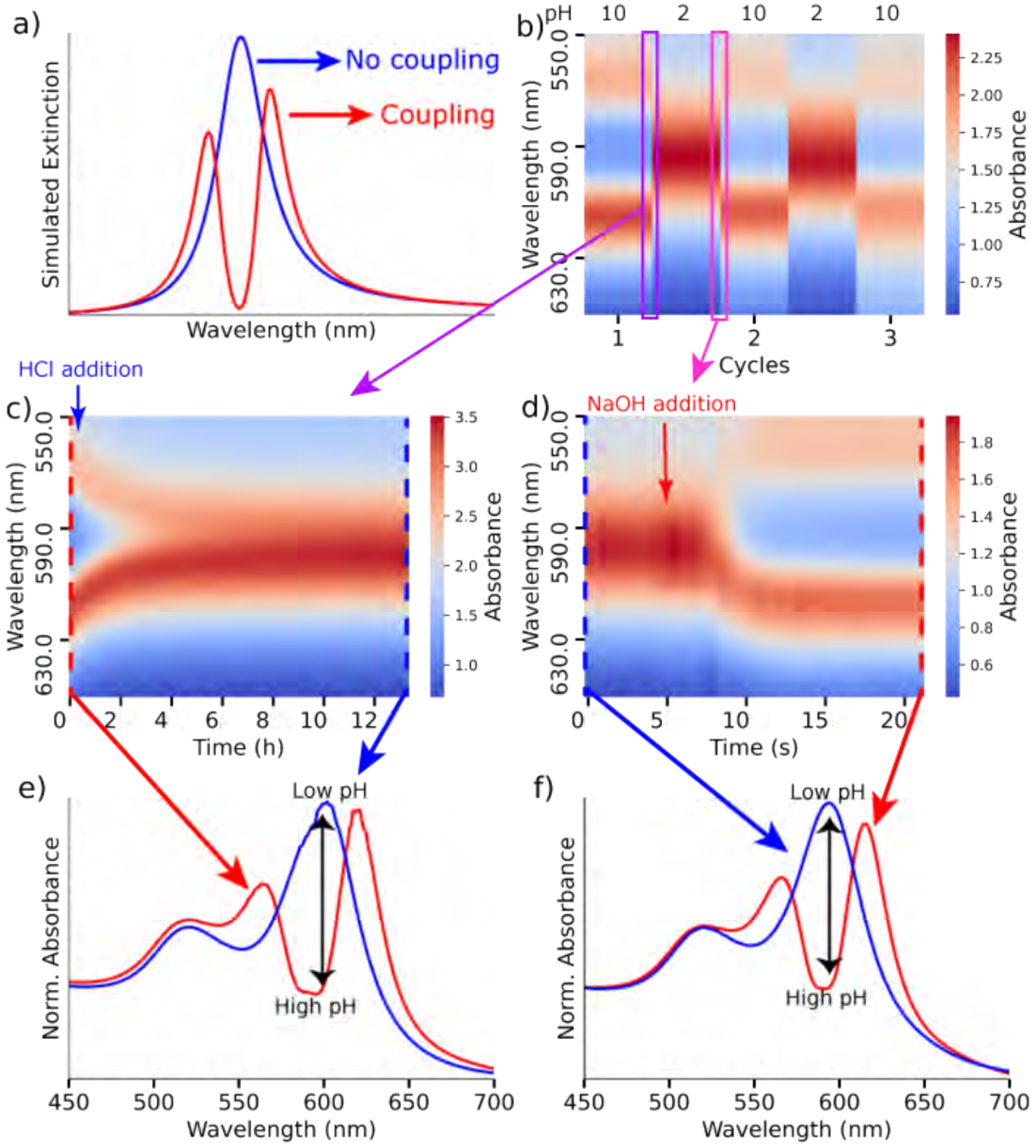

Figure 5.3: Switchable character of plexcitonic systems under pH. **(a)** Calculated optical response of uncoupled (blue line) and coupled (red line) plexcitonic system, indicating the expected optical output in experimental samples. **(b)** pH-dependent switchable character of plexcitonic system performed for 3 cycles with clearly visible spectral splitting. **(c)** Time-dependent monitoring of spectral change upon the addition of HCl to the preformed coupled system, showing slow decoupling over several hours **(d)** Time-dependent monitoring of spectral change upon the addition of NaOH to decoupled system, showing fast decoupling within several seconds. **(e,f)** Initial and final spectra for both cases (HCl and NaOH addition) showing the switchable character of plexcitonic system.

Therefore, to obtain the g value, it was necessary to iterate the Equation 1.9 with the input value of g within limits of 0 and 200 meV, where the upper limit was conditioned by experimental findings in the previous chapter. A simple algorithm

was used then to filter the spectral match of generated numerical spectra with the experimental ones for given g values. That is the algorithm applied criteria in which the generated spectra for a given g value should exhibit two spectral branches with separation similar to that in experimental spectra. As a result, one can find the best spectral match and therefore extract the g value at each stage of the decoupling phase after the addition of a given concentration of acid.

Figure 5.4 **(b)** shows the resulting theoretical spectra that indicate a remarkable match with experimental data ([HCl] = 8 mM). The coupling strength for each step showed a progressive decrease to zero during three hours. The same process was applied to a wider range of acid concentrations.

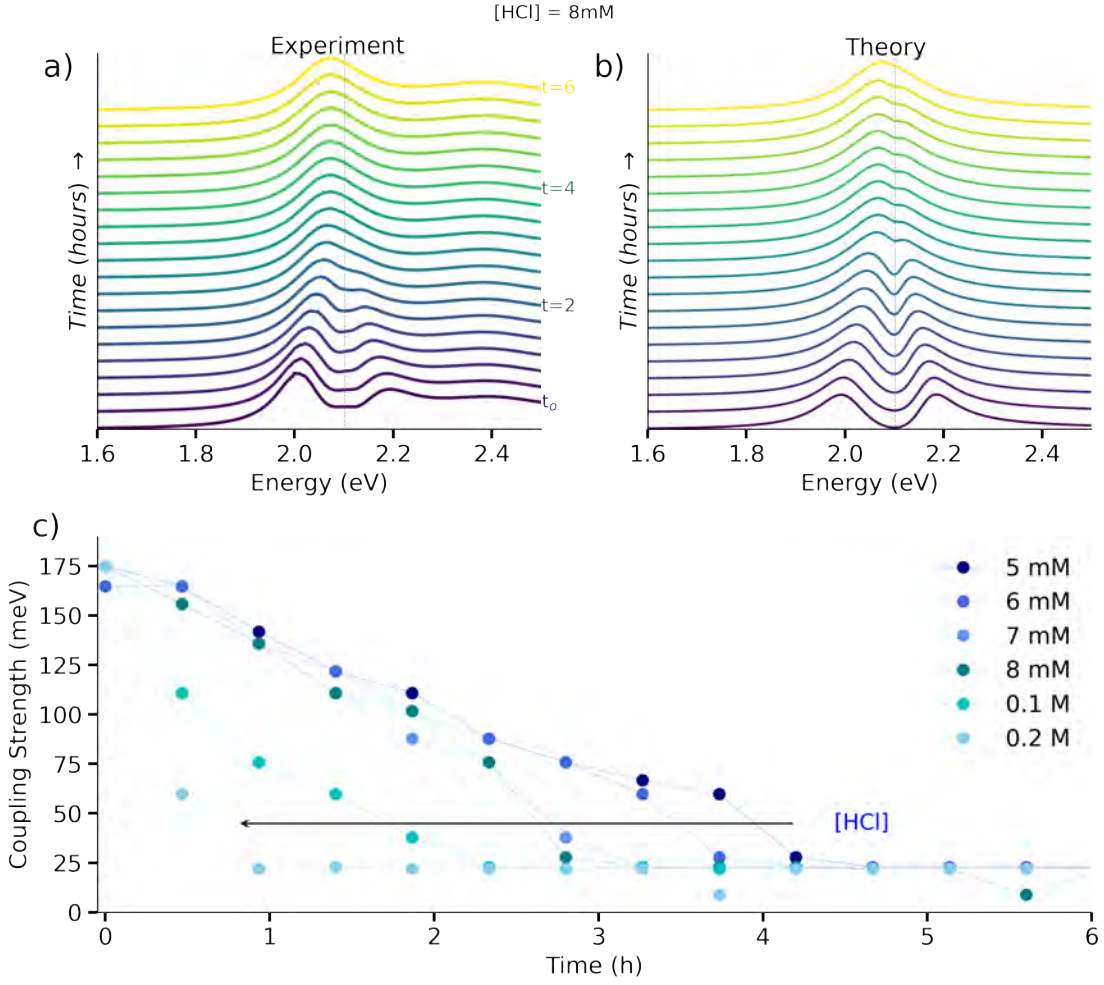

Figure 5.4: Effect of acid concentration on decoupling speed, evidenced by disappearance of Rabi Splitting. **(a)** Time-dependent UV-Vis-NIR spectra of the decoupling process taken in the interval of 20 minutes during 6 hours. **(b)** Modeled spectra response for the decoupling phase used to estimate g during the process. **(c)** Change of coupling strength for different HCl concentrations.

Figure 5.4 **(c)** shows the temporal evolution of coupling strength for the entire range of acid concentration, showing that for the highest acid concentration (200

mM) one needs 50 minutes to reach full decoupling. Still, it is remarkable to notice that at such a high concentration of HCl, this process is rather slow in comparison to the coupling phase which takes 10 seconds to complete.

The experimental and theoretical spectra for the other HCl concentrations can be found in the Apendix 5.7.

There is an acid concentration threshold below which full decoupling cannot be achieved. It was found that below 5 mM of HCl, the two spectral branches can approximate to each other, indicating decoupling, without fully merging (Figure 5.5 **(a)**.

Interestingly, at acid concentrations below the decoupling threshold, the spectral feature remains stable over time. That is, an addition of acid (0-5 mM) to the preformed plexcitonic system causes partial decoupling that remains stable, for at least 3 days. Such temporal stability allowed us to measure the photoluminescence properties of the plexcitonic system under given acid concentrations. The PL response is shown in Figure 5.5 **(b)**. There is a band (red line) for 0 mM HCl, where the maximum of the upper and lower branches were located at 585 nm and 615 nm, respectively. The excitation wavelength for all samples was 532 nm. With increasing acid concentrations, the low-energy band progressively disappeared. The high energy band remains stable, showing a slight blue shift towards the J-band of pure J-aggregates, but even in the final stage is $\approx$ 20 nm red-shifted from the J-band response. Overall, the PL measurements confirm the acid-controlled decoupling of the plexcitonic system.

Photoluminescence measurements were also implemented to study the switchable character of the plexcitonic systems. A solution containing a strongly coupled plexcitonic system was exposed to HCl (8 mM) followed by time-dependent measurement of both absorbance and emission (Figure 5.5 **(c, d)**). As expected, the high and low branches progressively merged over time after acid addition (spectra from red to blue in Figure 5.5 **(c)**). While in the absorbance spectra, one can observe one band only, in the emission spectra there are no characteristic features, that is, the system exhibits no emission, neither from pure J-aggregates [181]. Once NaOH was added, the doublet feature was recovered in both absorbance and emission spectra. First, we added half of the necessary amount of NaOH, resulting in an intermediate-stage system (Figure 5.5 **(c, d)** - violet lines). Further NaOH addition caused full recovery of the strongly coupled system.

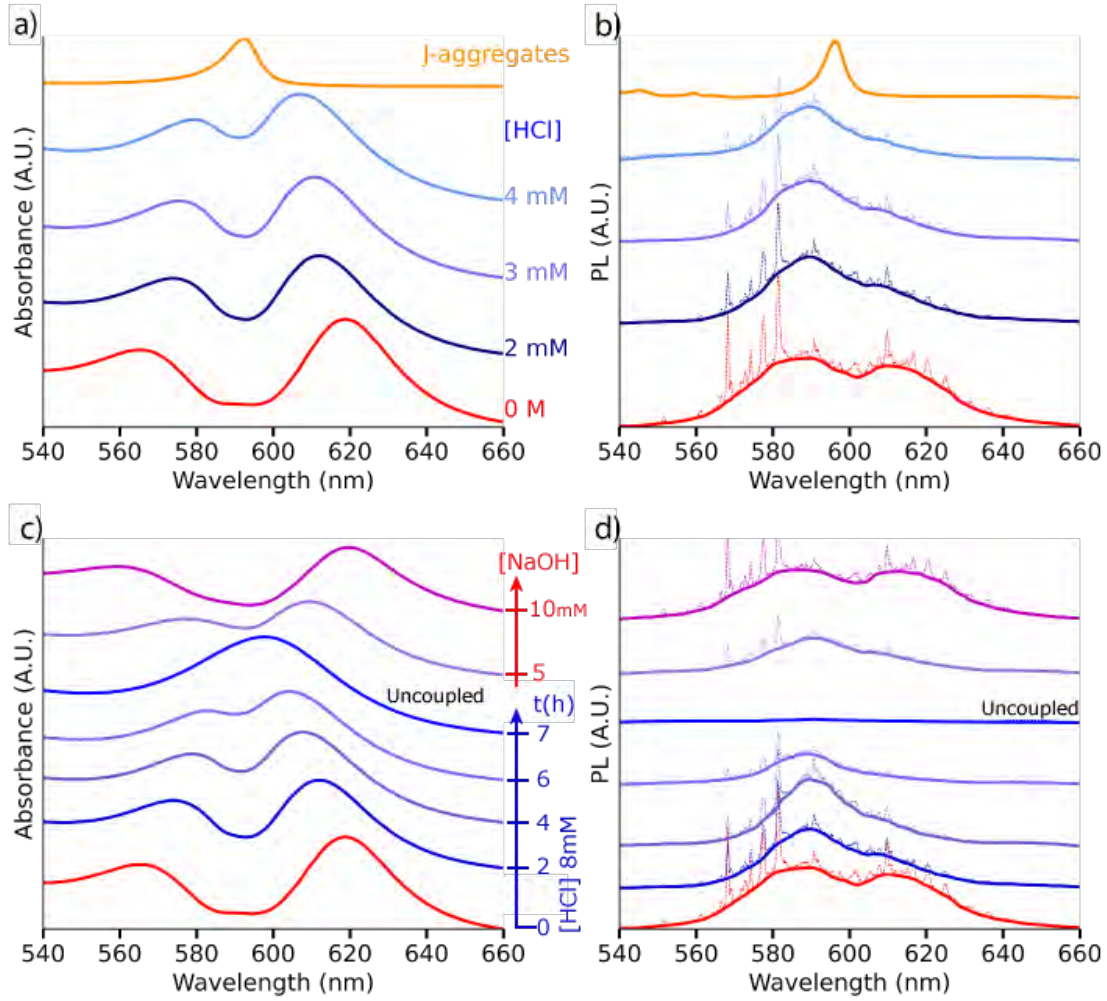

Figure 5.5: Reversible plexcitonic system, measured by absorbance and PL. **(a)** Absorbance spectra of plexcitonic system upon the addition of acid at concentrations insufficient to cause full decoupling. The intermediate system at low acid concentrations is stable over time. **(b)** PL response of the plexcitonic systems from panel a, showing doublet feature for the strongly coupled system and progressive disappearance of the lower polaritonic branch with increasing HCl concentration. **(c)** Absorbance spectra of one reversibility cycle of the plexcitonic system. The blue spectra refer to the sample after HCl is added, starting from the strongly coupled system. Once the system is decoupled, NaOH is added to return to the strong coupling regime (violet lines). **(d)** PL response of the plexcitonic systems from panel (c) during one cycle of reversibility. The initial doublet feature (strong coupling) progressively disappeared (one band only) to reach a fully decoupled regime with no PL signal. In (b, d) panels, the sharp peaks are Raman (SERS) features overlapping the PL spectra. The thick lines represent the PL signal after removing those features.

The PL lifetimes of the decoupling system were also analyzed to investigate the recombination dynamics in the coupled/decoupled system. The lifetime values were sensitive to the decoupling process. Under strong coupling, the first lifetime components of 1.9 ns progressively increase to 2.9 ns upon decoupling, corresponding to the lifetime value of pure J-aggregates (3 ns). The second component remained constant (0.2 ns). However, the distribution of these lifetime components is remarkably

different from the obtained in pure J-aggregates. The longer component represents 3% and the shorter %97, a behavior similar to the one in coupled systems. In pure J-aggregates, the longest component (3.3 ns) represents 30 % and the shortest one (0.9 ns) represents 70 %. In the case of strongly coupled hybrids, the longer component decreases to 2-4 % (see Table 4.1) so the PL is dominated by the second component (the shortest one) that also has a smaller value (0.2 ns). In conclusion, the PL signal of a decoupling system shows a notable decrease in intensity compared to the coupled one, and the estimated lifetime components (τ_2) are longer.

To close the present section, during pH-regulated coupling, the optical properties of the system changed, switching from the state of the hybrid system to states of corresponding components. Absorbance measurements showed the presence of spectral doublet upon strong coupling and response corresponding to bare gold particles under a decoupled state. PL characterization showed that during decoupling, the optical response approaches that of bare J-aggregates response. The lifetime of excited states of the system in the decoupling stage showed an increase in the first-lifetime component, this change can be related to chain size modification during the process but also because of the lower interaction with the gold particles.

5.4.1 Raman features in PL spectra

A careful reader will ask about the origin of the sharp peaks in PL spectra, as shown in Figure 5.5. These peaks are well-known Raman (SERS) responses of J-aggregates systems and have been shown to provide information about the molecular structure of the system under study. [161]

Although a detailed analysis of Raman features in plexcitonic system falls beyond the scope of the present dissertation, we put an effort to provide preliminary results on such a Raman response of the system under coupled and decoupled states. Figure 5.6 shows PL spectra along with Raman features from three different experimental scenarios:

- Physical mixture of gold bipyramids with JC-1 monomers at neutral pH showing Raman features superimposed on the PL background spectrum (Figure 5.6 - light blue line).
- Fully coupled hybrid system at high pH with two PL bands (Lower Polariton Branch and Higher Polariton Branch) and SERS features overlapping the PL spectrum (Figure 5.6 - purple line).
- Partially decoupled system at low pH with an intense high energy band and accompanied by SERS features in the spectral range corresponding to that high energy band (Figure 5.6 - blue line).

These data indicate that mixing JC-1 dye with bipyramids leads to partial adsorption of molecules on a metal surface (or incorporation of molecules within a surfactant bilayer), resulting in the formation of a weakly coupled system.

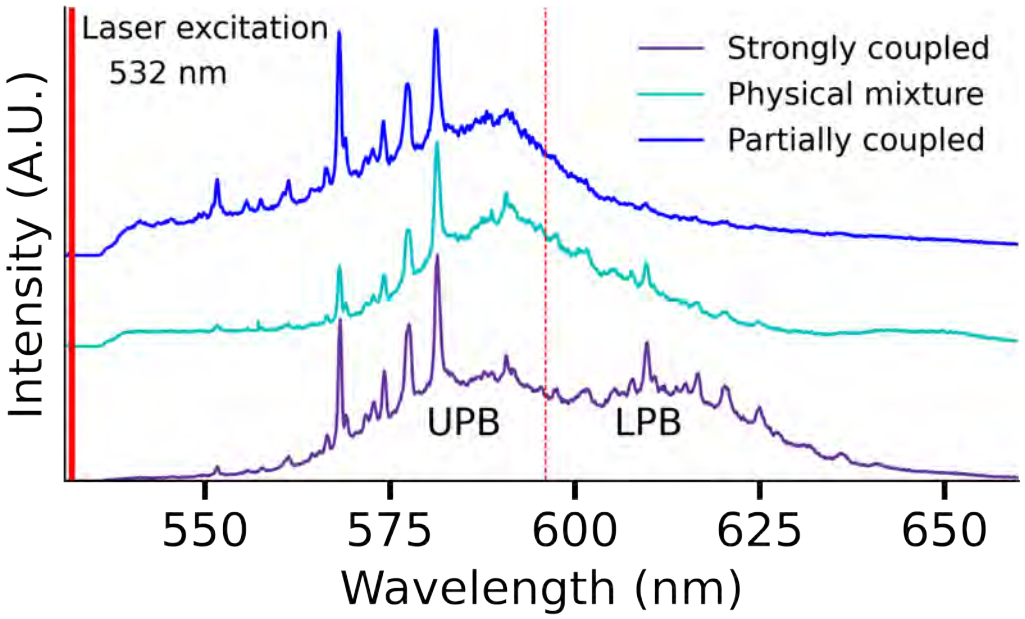

Figure 5.6: PL and SERS spectra of fully coupled plexcitonic system at high pH (purple spectrum), the partially decoupled system at low pH (blue spectrum). The spectrum in the middle (light blue) corresponds to a physical mixture of JC-1 and gold bipyramids at neutral pH showing features that resemble a partially coupled system.

The plasmonic character of gold acting as a nanoantenna can to some extent enhance the Raman response of the molecules close to the metal surface. This is particularly visible for fully coupled and partially decoupled systems where the difference in Raman features is considerable, see the spectral range between 600 and 625 nm. Our results presented in Figure 5.6 clearly demonstrate that it is possible to significantly expand the spectral region in which SERS acts by exploiting the strong coupling phenomenon. This finding has important implications for advances in SERS sensing.

Further Raman analysis is needed to fully resolve the composition of the metal-J-aggregates interface under different pH conditions.

5.5 Reversibility Mechanism

Although pH is the main driving force in controlling the degree of coupling, the presence of surfactant molecules has an important effect on the interaction of JC-1 molecules and their aggregates with metal surfaces. Previous literature showed that JC-1 is commonly used as an optical sensor in microbiology, where JC-1 molecules selectively incorporate and aggregate within the biological membrane. JC-1 monomers have limited solubility in water, that is, they have a slightly hydrophobic character that gets pronounced when molecules form aggregates, favoring their accommodation in the hydrophobic bilayer. In our case, gold nanoparticles are covered by a bilayer of surfactant molecules. Previous studies showed that the thickness of the

bilayer is around 4 nm [183], making thus a physical space to accommodate JC-1 molecules. Therefore, the physical mixing of gold bipyramids with JC-1 under neutral pH leads to spontaneous incorporation of the molecules into the surfactant bilayer, which is witnessed by the formation of weak coupling with visible Raman features in PL spectra (Figure 5.6). Further increase of pH leads to the immediate formation of J-aggregates, the emergence of J-band that in the presence of plasmon band leads to the formation of a new state of strong coupling. The hydrophobic aggregates remain protected in a hydrophobic environment within the surfactant bilayer. Subsequent decrease of pH leads to slow disintegration of J-aggregates and thus transition from strong to weak coupling state. Thus, one can assume that switchable coupling is ruled by the interplay of retaining J-aggregates close to a metal surface through a surfactant bilayer at high pH and their dis-aggregation and eventual release to bulk solution upon lowering pH (Figure 5.7 **(a)**).

We performed a series of control experiments to evaluate the fate of JC-1 molecules in the plexcitonic system upon pH change. First, the plexcitonic system was prepared by mixing AuBPs with JC-1 at pH=10 followed by washing via centrifugation and redispersion in CTAB (pH=7) (Figure 5.7 **(b)** - coupled system). Next, the pH of this solution was lowered to 2, resulting in a slow decoupling (Figure 5.7 **(b)** - uncoupled system). The sample was centrifuged and the supernatant (no particles) was physically separated from the precipitate (particles). The optical characterization of the supernatant showed an absorbance band located at 300 nm and a PL band at 400 nm, instead of the expected band of JC-1 monomer at 500 nm. It is well known that the monomer band at 500 nm of JC-1 can get suppressed at low pH, which is due to the protonation and thus breakage of the conjugated structure within the molecules (or withdrawn of pi electrons), making detectable the absorbance from benzimidazole unit only. [151, 184–186] Further increase of pH of supernatant leads to recovery of the monomer band and eventually the formation of J-band when the pH value is increased even more (pH=8) (Figure 5.7 **(b)** - middle column). Such behavior was also confirmed for a fresh solution of JC-1 molecules. We mixed fresh JC-1 molecules with CTAB solution (1mM) and subjected it to pH treatment, observing absorbance at 300 nm (benzimidazole unit) at pH=2, JC-1 band at 500 nm at pH=7 and formation of J-aggregates at pH=9 (Figure 5.7 **(b)** - left column). Overall, the pH-responsive behavior of JC-1 is intricately linked to the protonation/deprotonation of functional groups within the molecule and induces aggregation of molecules due to changes in electrostatic repulsion.

Importantly, the precipitate containing AuPBs only was redispersed in CTAB (1mM) and subjected to the increase of pH to 8, showing no change of optical properties (Figure 5.7 **(b)** - right column). That is, no hybrid system was formed, suggesting too low a concentration of JC-1 molecules in the proximity of metal to form J-aggregates and thus generate a coupled system. These experiments show that upon the decrease of pH in a hybrid system, the J-aggregates disintegrate followed by the release of monomers to the bulk solution that can be separated physically by centrifugation and later re-used to form J-aggregates upon increase of pH.

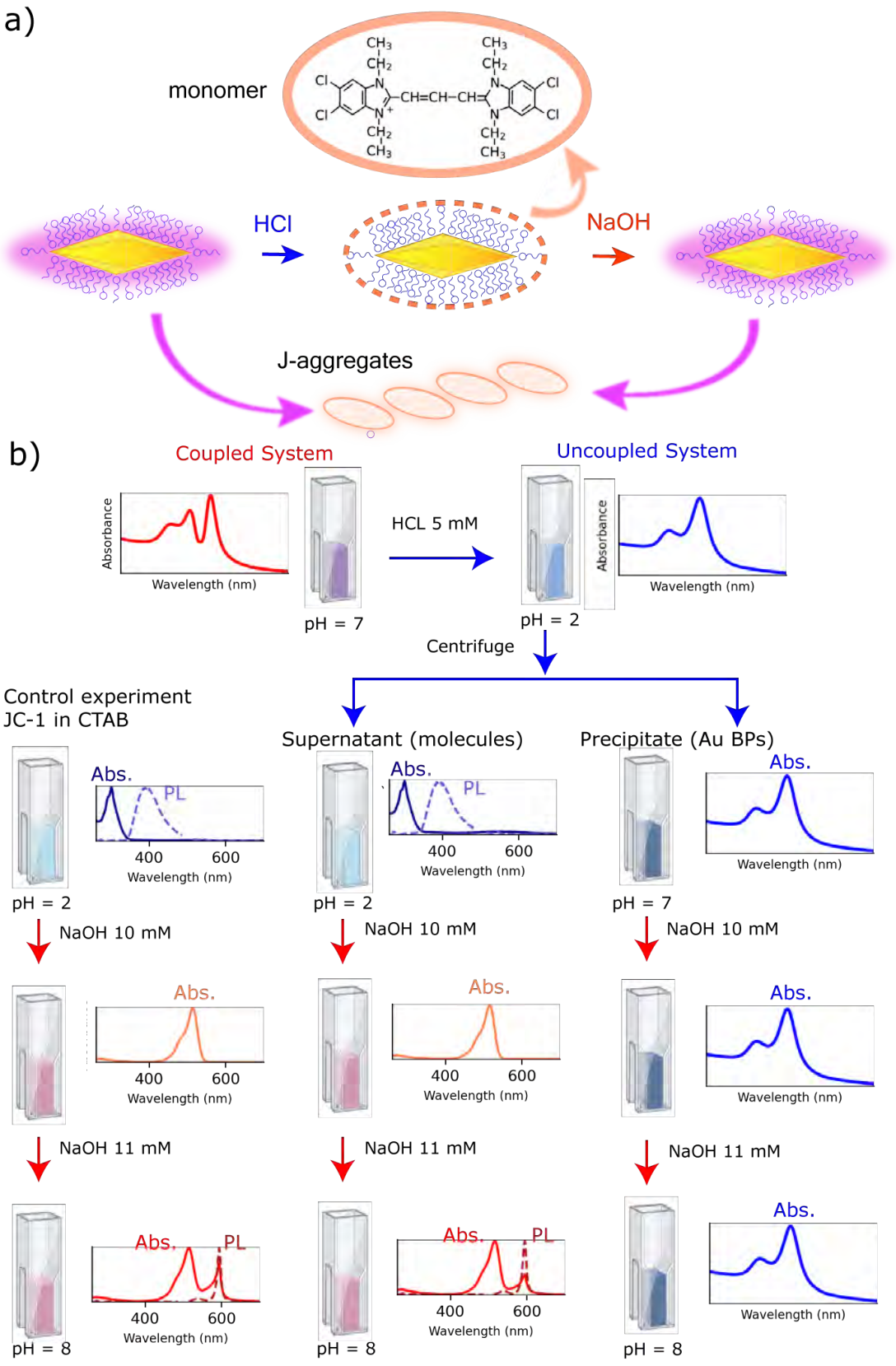

Figure 5.7: Working mechanism behind the reversible behavior of the plexcitonic system. **(a)**Schematic representation: HCl presence in the plexcitonic system triggers J-aggregates disintegration and NaOH establishes the plexcitonic system by the J-aggregates recovering. **(b)** Schema of the experimental procedure. The absorbance and PL spectra at every stage of the hybrid system, supernatant, precipitate, and JC-1 molecule in CTAB solution were compared.

The remaining puzzle is the huge kinetic asymmetry of coupling and decoupling processes. One can postulate that the fast formation of a strongly coupled system (seconds) is a result of cooperative intermolecular forces where pi-pi and hydrophobic attractive interactions drive JC-1 molecules to form J-aggregates within the surfactant bilayer. Now, the reversal of this process requires an additional energetic input to overcome attractive intermolecular, forces leading to slow dis-aggregation and diffusion of molecules out of the surfactant bilayer. Certainly, an additional study is needed to fully understand the chemical mechanism behind the pH-dependent formation of plexcitonic systems. For example, real-time Raman measurements of the system under different pH conditions can provide valuable information on the interactions between JC-1 molecules and/or the interaction of JC-1 molecules with metal surfaces. Raman response of the molecules can be further enhanced through the SERS effect, bearing in mind the presence of plasmonic components.

Overall, these data indicate that the switchable plexcitonic system is the result of a subtle interplay of pH-dependent solubility of JC-1 molecules in their accommodation within the surfactant bilayer. There are several intermolecular forces (pi-pi, electrostatic, and hydrophobic) that can drive cooperatively the formation of supramolecular aggregates in proximity to the metal surface to eventually give rise to a new hybrid system.

5.6 Conclusions

In this Chapter we demonstrated a new chemical means to control reversibly the degree of strong and weak coupling in a plexcitonic system. We showed that pH is the suitable chemical means to control such a switchable character, where a plexcitonic system under strong coupling at high pH can be switched to a weak coupling regime upon lowering pH. Three reversible cycles were conducted, as demonstrated by UV-Vis-NIR measurements. An interesting feature of switchable plexcitonic was a huge temporal difference in coupling (seconds) and decoupling (minute) processes. Such a slow decoupling allowed us to monitor in detail the process and quantify the change of coupling strength under different acid concentrations, showing that 5 mM of HCl is the lower limit to fully decouple the plexcitonic system. The reversibility was also confirmed by PL measurements, showing a gradual transition from double-band emission (strong coupling) to single-band emission (weak coupling) and finally the disappearance of emission. Through the realization of control experiments, we pictured the preliminary mechanism behind the switchable plexcitonic system. The interplay of protonation/deprotonation of JC-1 molecules and the presence of a surfactant bilayer with hydrophobic confinement seems to be central to controlling the rate of J-aggregate formation in the proximity to the metal surface.

To the best of our knowledge, this is the first experimental example of a switchable plexcitonic system in bulk colloidal solution. Having in mind the simplicity of the trigger - concentration of protons in the solution -, we foresee totally new possibilities in the design and fabrication of novel (bio)sensors and actuators.

The results obtained also clearly show the potential to greatly broaden the

spectral range within which SERS operates by leveraging the strong coupling phenomenon. This discovery holds significant ramifications for the advancement of SERS sensing technologies with added functionality.

Conclusions and Outlook

5.7 Conclusions and Outlook

This work is focused on investigating the interplay between plasmon-exciton interactions within strongly coupled plexcitonic systems. Here, gold nanoparticles were used as the plasmonic component, and molecular chains known as J-aggregates formed the excitonic component. Chapter 2, shows the analysis applied to characterize the photophysical properties of the excitonic systems using different spectroscopic techniques, including estimation of the exciton delocalization length in J-aggregates. This analysis was applied to two organic dyes that show the formation of J-aggregates upon increase of ionic strength and pH respectively. Later, in Chapters 3 and 4, we used carefully chosen interparticle interactions to establish the formation of two different plexcitonic systems using both dyes in a colloidal solution. This demonstrates our control over the design principles to reliably establish strongly coupled systems using different plasmonic and excitonic components. Subsequently, thorough characterizations were conducted to analyze the photophysical properties and evaluate the strength of coupling between the plasmonic and excitonic components. The results of this study draw the first steps into the application of strongly coupled plexcitonic systems for sensing and photocatalytic applications. Chapter 5, shows our control over interparticle interactions to realize the formation of reversible strongly coupled plexcitonic systems, a nontrivial task in the field. A detailed summary of each thesis Chapter is presented below.

- In Chapter 2 we conduct a detailed investigation into the excitonic properties of two dyes forming J-aggregates. Here we applied a range of spectroscopic techniques including absorption, transient absorption, photoluminescence spectra, and photoluminescence lifetimes. The findings underscore the necessity of a comprehensive approach for accurately determining the exciton coherence length. It is evident from our analysis that a singular experimental analysis under fixed conditions is insufficient. By integrating data from multiple techniques, a clearer understanding of excitonic behavior has been attained. Studying the complete kinetics of forming J-aggregates with multiple spectro-

scopic techniques can deepen the understanding of the interactions in the system. Moreover, the quantification of parameters within complex supramolecular systems like J-aggregates holds significant implications for their present and future utilization across a spectrum of light-related applications. Looking ahead, the characterized J-aggregate systems for both dyes serve as foundational components in subsequent chapters, where we will construct plexcitonic systems and explore their optical properties, evaluating their potential suitability for photophysical applications.

- In Chapter 3 we discuss the establishment of a novel plexcitonic system through the integration of plasmonic nanostructures with J-aggregates, successfully demonstrating it is in the strong coupling regime. Through a comprehensive optical characterization utilizing absorbance and PL responses, we analyzed its response in the near-infrared (NIR) spectral region. From this we have elucidated key parameters related to the coupling regime, such as the Rabi-splitting energy and coupling strength, indicating operation within the strong coupling regime. The superior properties exhibited by the hybrid systems, including enhanced photostability and broadened absorption spectral range, underscore their potential for various applications. Notably, our investigation into photophysical changes through photoluminescence response and photodegradation analyses further validates the utility of these systems. As evidenced by existing applications in photocatalysis, such as Au nanoparticles coupled to a Fabry-Pérot nanocavity for enhanced water-splitting and oxidation, the emergent properties of plexcitonic systems hold promise for advancing diverse fields of study and technological applications. The limitations inherent in plexcitonic systems stem from the characteristics of their constituent components. In this system, they arise primarily from the aggregation behavior of the gold nanobipyramids in the presence of oppositely charged dye monomers, as well as the susceptibility of the plexcitonic system to photothermal effects. Nevertheless, these limitations can be surmounted through strategic adjustments to the surface chemistry of the gold bipyramids, to modulate the interaction between the nanoparticles and the dye molecules. This can concurrently enhance the colloidal stability of the plexcitonic system and pursue the mitigation of this limitation. This approach holds promise for expanding the utility and robustness of plexcitonic systems in various applications.

- In Chapter 4 we present the elucidation of a second plexcitonic system, featuring the synergy of J-aggregates and gold nanobipyramids. Even though, the interaction of gold nanostructures with JC-1 Jaggregates was already reported, this study has been an undertaking marked by notable findings. Once the plexcitonic systems were established, we pursued the analysis of the Rabi splitting energy, derived from both absorbance and PL responses. We analyzed the dispersion curves resulting from the plasmon-exciton detuning and the theoretical models predicting this interaction response for the systems' scattering and emission. These analyses unequivocally substantiate the characterization of this plexcitonic system as strongly coupled. The photostability of this system was tested because of the immense importance of this feature

in applications. It was subjected to light irradiation, specifically the system's range of absorbance. The results showed a high resistance to photo-oxidation of the strongly coupled system, showing the profound modifications this coupling entails. Since J-aggregates present a high rate of degradation under light irradiation, the resistance of this nanohybrid system makes it a more suitable candidate for photocatalytic applications.

- In Chapter 5 we explore further the plexcitonic system characteristics to establish a switchable colloidal nanohybrid system. We analyzed the system's reversibility, which is derived from the J-aggregate's sensitivity to pH modifications. Also, using the absorbance and PL responses of the system we studied possible modifications in the system's properties during the complete reversible cycle. Both absorbance and PL showed that our system can recover its properties with minimal dumping even after 3 cycles of reversibility. These cycles consist of an initial strongly coupled system that slowly decouples with decreasing pH until reaching just the plasmonic response. Once the pH is raised, our system recovers all the spectroscopic signatures of a strongly coupled system. Through an exhaustive analysis of each of the steps of the reversible cycle in the plexcitonic system and pure J-aggregates, we established the mechanism behind this behavior. However, the limits of the plexcitonic system's reversibility are drawn by the particles' stability against the inevitable increase in the ionic strength of the solution.

This investigation is intended as a preliminary study of the application of plexcitonic systems in photocatalytic processes. There are several aspects requiring further studies that can provide a clearer picture of the processes taking place in the strong coupling interaction within these systems. Even though, we consider the presented results could be considered as a promising first step towards interesting and useful applications of gold nanoparticles/J-aggregates strongly coupled systems.

Appendix

Synthesis of gold nanoparticles

The synthesis method employed to obtain gold nanoparticles for this work is further explained in the following sections.

Gold Nanorods

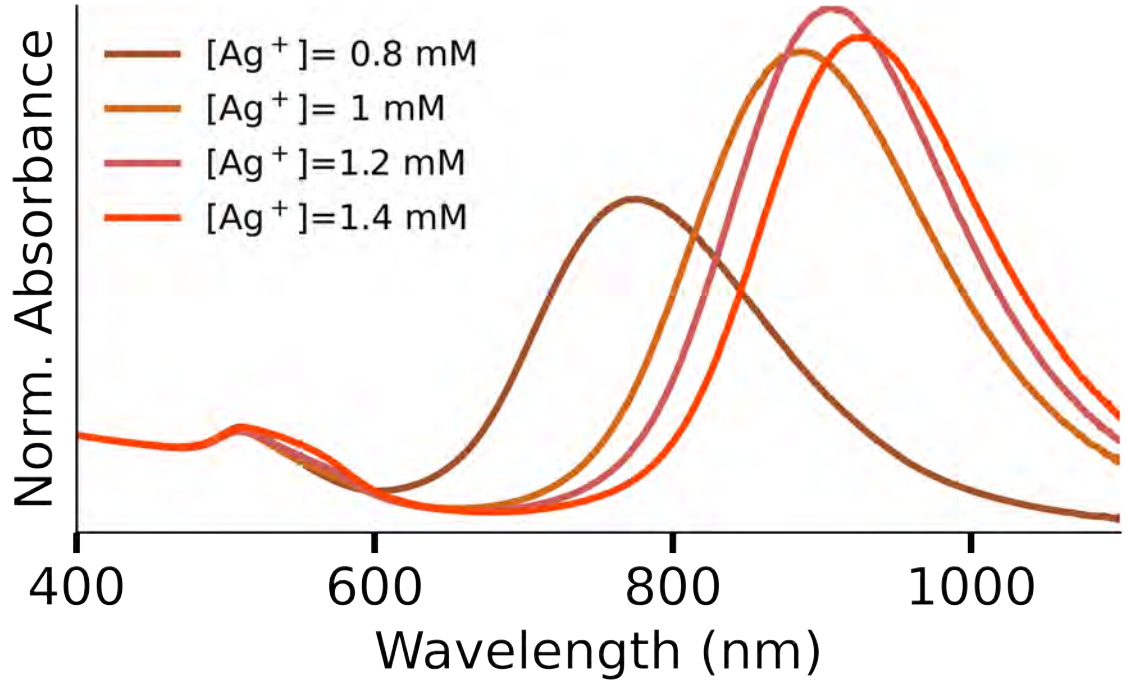

Figure 1: Effect of silver concentration on the position of longitudinal surface plasmon resonance. The LSPR in the NRs samples is noticeably affected by the silver ions concentration, this is seen in their absorbance response where at higher Ag^{+} concentrations the plasmonic resonances are localized at higher wavelengths.

The Au NRs employed in our analysis were synthesized using common gold seeds that we proceeded to grow to produce single-crystalline NRs. In the applied method, cethyltrimethyl ammonium bromide (CTAB) is employed to assist the seed-mediated growth process involving silver nitrate [187,188]. Here, the control of the NRs' optical properties can be established by the reagent concentrations in the growing process, the silver ions, or gold seeds concentration. The influence of silver ion concentration in the growing step can be observed in Figure 1, where plasmonic responses at higher wavelengths are obtained for higher silver concentrations. Also, we can observe two plasmon modes: the longitudinal and the transversal modes emerging from the electronic oscillations in the two main axes of the rod. Since the longitudinal plasmon resonance redshifts as the NR aspect ratio increases, we can conclude that the rods enlarge with increasing $[Ag^{+}]$. On the other hand, the transversal plasmon response wavelength remains constant because there is no change in the rod diameter. The plasmon resonance narrowing with the redshift is due to the interband transitions' reduced contribution [17]. During the synthesis process, we employed a mild reducing agent (ascorbic acid) to prevent the origin of a secondary nucleation. The correct formation of Au NRs can be checked using the UV-vis-NIR spectra of the final solution, where it is possible to discern the Au NRs' plasmonic signatures.

Oxidative Etching

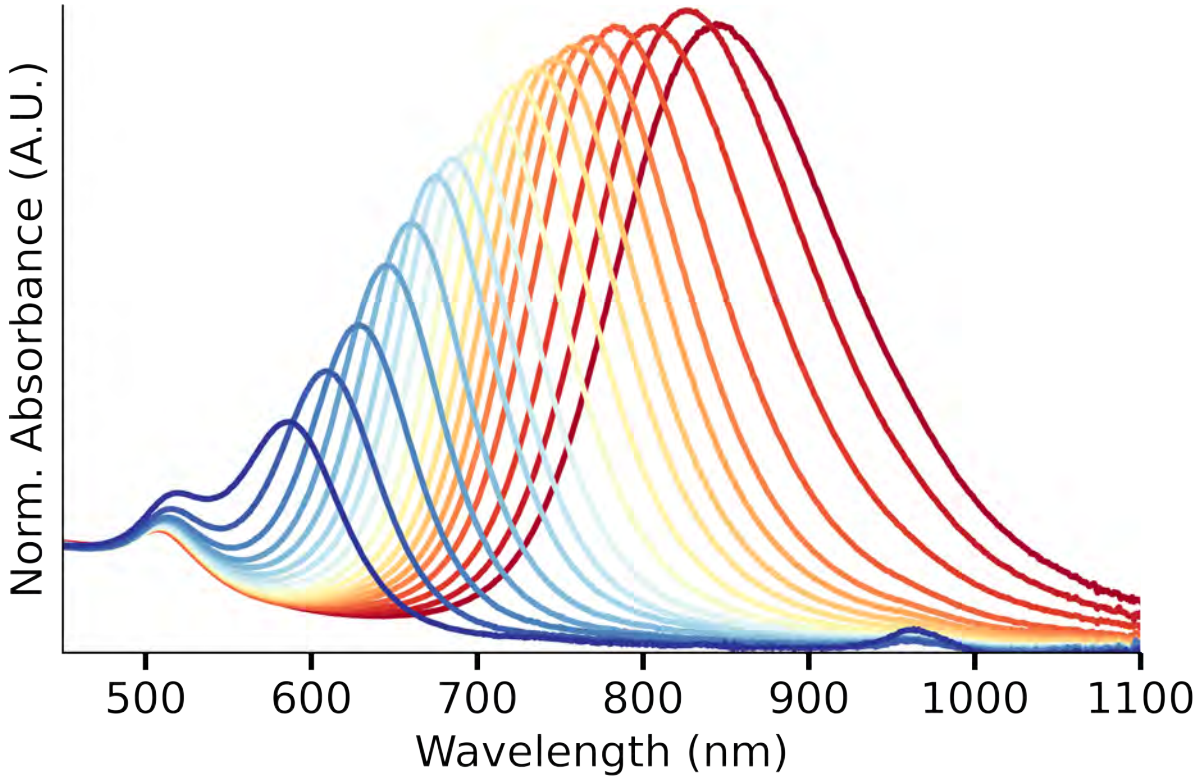

Figure 2: Oxidative etching process applied to Au NRs.

The LSPR of Au NRs was modified by applying the oxidative etching process. Figure 2 shows the LSPR shift from an initial longitudinal plasmonic response at 850 nm to 590 nm, in this case, the wavelength of the response decreases at around 10 nm. This method allows to shorten the length of the particles while preserving their width.

Gold Bipyramids

The Au BPs represent anisotropic nanostructures characterized by distinct features attributed to the intense electric field generated at their edges and tips. This anisotropy contributes to heightened local field enhancement and monodispersity, surpassing those observed in NRs and other morphologies, resulting in a notably narrow absorbance feature. Liu et al. [17] have extensively explored the unique properties of Au BPs, emphasizing their pentatwinned crystal structure and the manifestation of a distinctive narrow and intense localized LSPR response in comparison to gold nanorods. To manipulate the plasmonic response of BPs, the concentration of Au seeds in the growth solution was systematically varied.

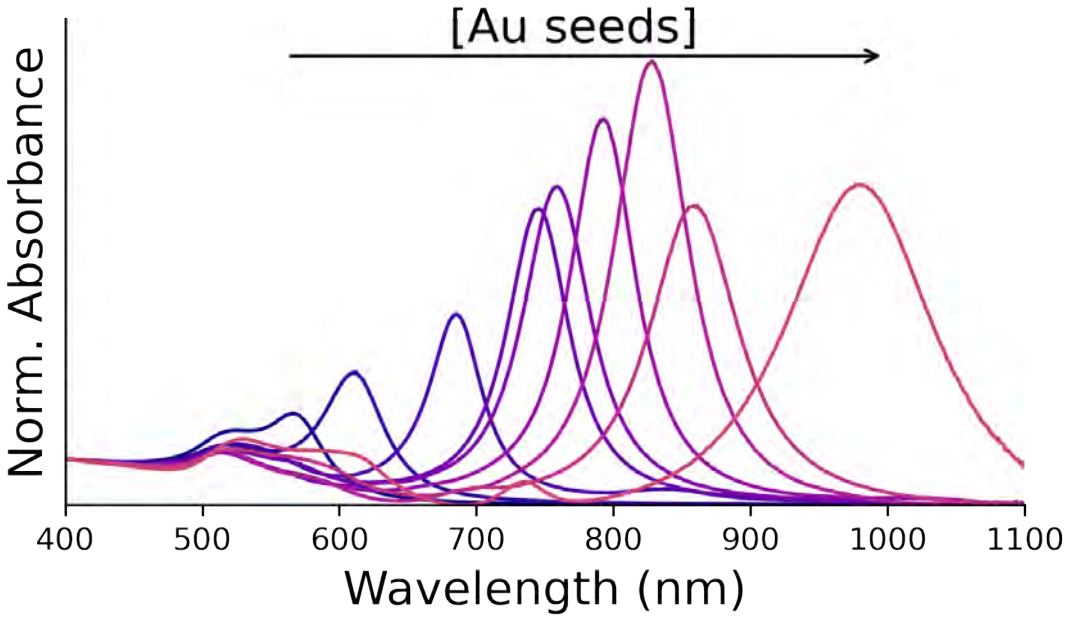

Figure 3: Effect of seeds concentration during the Au BPs synthesis process.

Figure 3 illustrates that an increase in the Au seed concentration correlates with a redshift in the LSPR wavelength. This observed phenomenon is consistent with the modulation of the BPs' size. Unlike gold nanorods, where tuning primarily affects longitudinal and transversal plasmon modes, the enlargement of BPs introduces additional contributions to their plasmonic response. Notably, the width of the BPs remains constant despite the size increase induced by higher seed concentrations, resulting in an unaltered wavelength for the transversal plasmon mode.

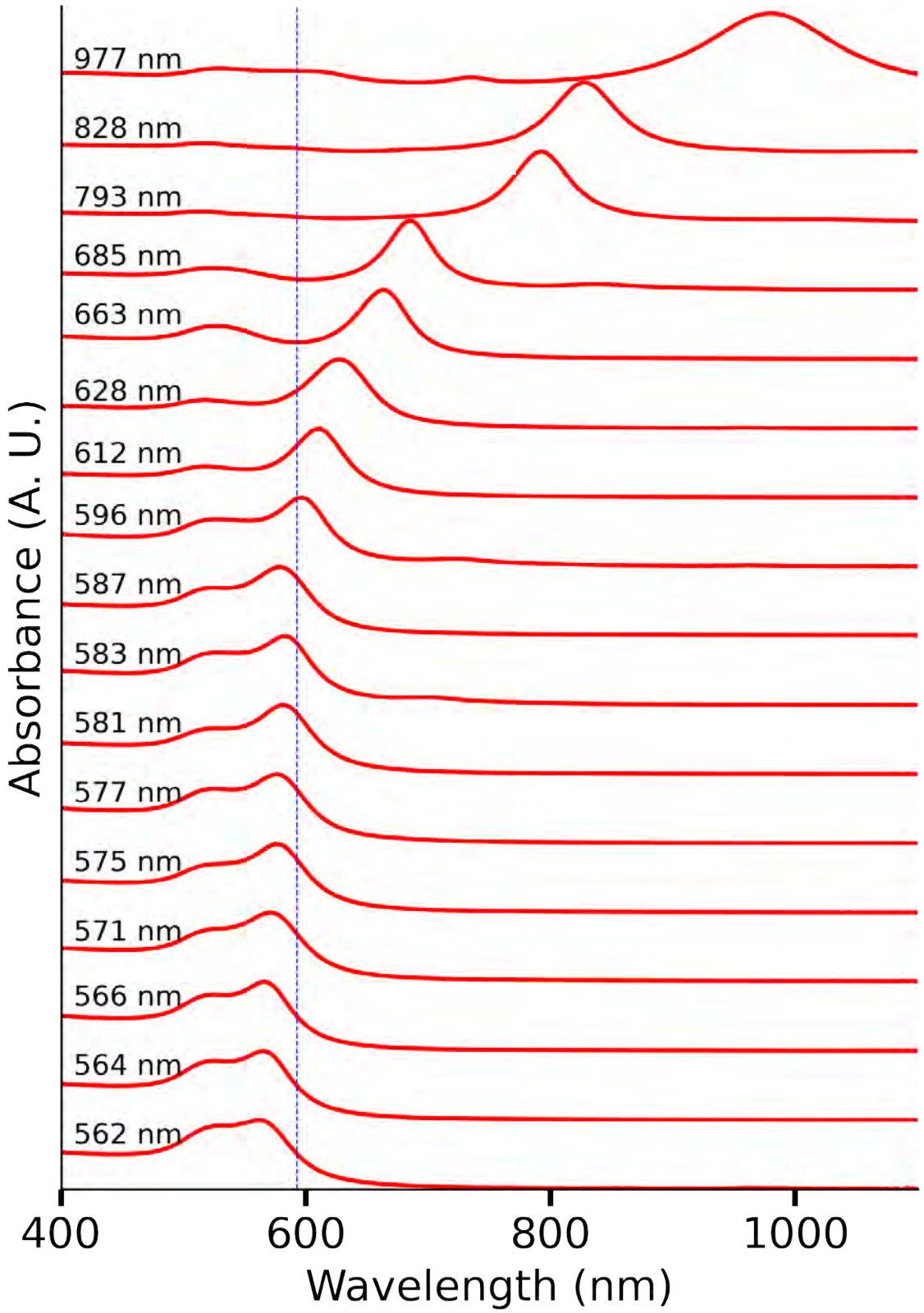

Figure 4: Au BPs synthesized using Au pentatwinned seeds. These samples were used to couple with JC1 J-aggregates and build plexcitonic systems.

Plasmonic NPs Comparison

The difference in the plasmonic responses of Au NRs and BPs is notable. Gold bipyramids possess a narrower and more intense plasmonic response, as seen in Figure 5 **(a)**. The plexcitonic system based on Au NRs (Figure 5 **(b)**) was previously reported and the obtained Rabi-splitting energy has a similar value as the obtained for AuBPs (≈ 200 meV) [178].

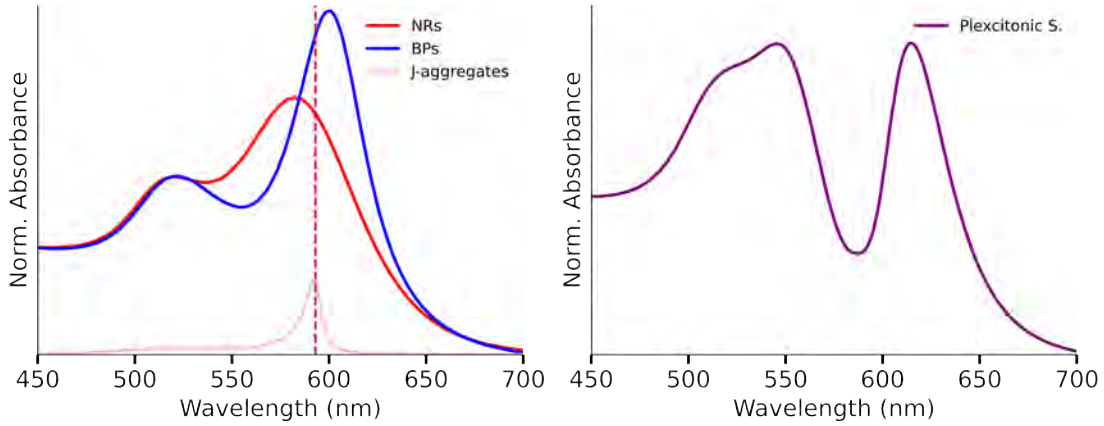

Figure 5: **(a)** Plasmonic response of Au NRs (red line), Au BPs (blue line). **(b)** Absorbance of a plexcitonic system based on Au NRs and JC-1 J-aggregates.

J-aggregates

Reported coherence length

The value of N_{coh} has been reported for several J-aggregates of cyanine dyes, these values were obtained from different experimental analyses like the monomer and aggregates concentration comparison (using absorbance spectra), enthalpy consideration, transient absorption spectroscopy, etc. The coherence length of each one of these dyes and the used technique is summarized in the following table.

Table 1: Table with the values of N_{coh} reported for J-aggregates of certain compounds.

Compound	N_{coh}	Experimental Technique	Reference
BIC	12-13	PL decay, T = 60 K	[107]
Cyanine dye S120	30	TEM	[125]
Cy3	55	Absorption linewidth	[189]
C8O3 tubular TDBC	95	Transient absorption T = 1.5 K	[123]
DMDC	4	Absorption (water)	[111]
JC1	8	2-D Aggregation structure	[190]
	30	Absorption, RT	[130]
L-21	32	Absorption	[131]
MC	10	Absorption	[125]
Me-DS	26	Absorption, transient absorption	[117]
amphi-PIC	30	Absorption	[191]
PIC	2-3	Absorption	[132]
	4	PL decay	[110]
	5	Radiative lifetime, T = 140K	[192]
	5-29	Pressure-induced absorption	[121]
	7-25	Ethalpy consideration	[126]
	8.9	Relative PL intensities	[193]
	26	Absorption, RT	[124]
	30	Absorbance linewidth	[194]
	60	Absorption	[114]
	70	Two-color transient absorption	[120]
	100	Transient absorption	[88]
	100	PL decay, T = 4.2 K	[48]
	100	Transient absorption	[113]
PIC-AgBr	2.1-2.5	Absorption, RT	[128]
PIC-Br	10	PL decay, T = 220 K	
	20	Transient absorption	[129]
	50	Absorption, T = 1.5 K	[118]
	115	PL decay, T = 1.5 K	[116]
	340	Transient absorption, T = 77 K	[127]
PIC-I	100	Absorption, PL at T = 77 K	[122]
TC	4	Absorption linewidth	[195]
TDC	4	Absorption linewidth	[195]
	25	Absorption linewidth	[196]
TDBC	4	Monomers and aggregates concentration comparison.	[34]
	6	PL decay	[115]

Compound	N_{coh}	Experimental Technique	Reference
TDBC	6.3, 6.3, 7.9, 8.3, and 9.4	Radiative rates (different surfactants)	[197]
	10	PL lifetime	[198]
TDBC (C2S4)	16	Femtosecond spectroscopy RT	[112]
	30 - 45	Transient absorption T = 1.5 K	[47]
THIATS	9	Absorption linewidth	[199]
	17	Radiative lifetime, T= 140K	[192]
	19	Absorbance linewidth	[196]
Thyacarbocyanine	6	Absorption	[119]

Plexcitonic Systems

Reversible Plexcitonic Systems

J-aggregates reversibility

CTAB possible effects on JC-1 J-aggregates were explored, by tracking their reversibility in a 1mM CTAB solution. Here, we used a solution of JC-1 (25 μM) in an aqueous solution and the same concentration in CTAB to analyze the absorbance response of both solutions.

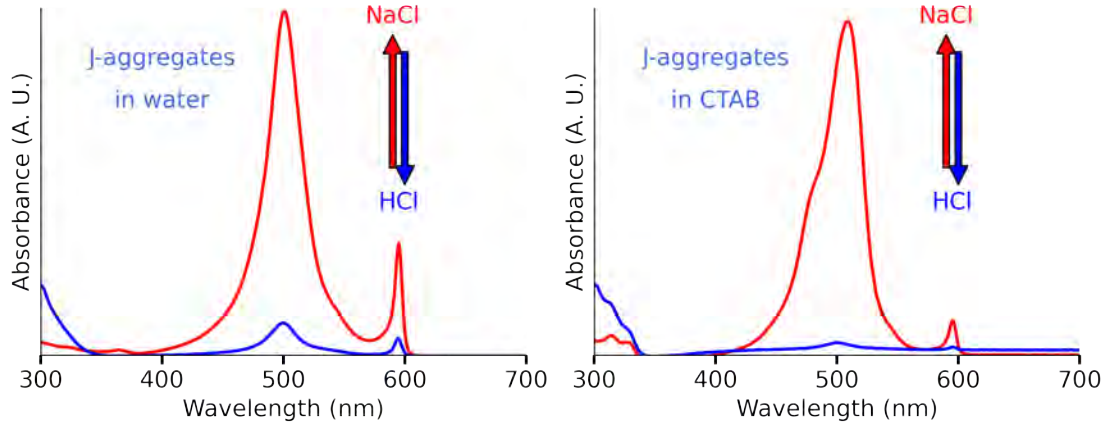

Figure 6: The effect of Au seeds concentration on the position of longitudinal surface plasmon resonance of Au BPs. The LSPR in the NRs samples is noticeably affected by the silver ions concentration, this is seen in their absorbance response where at higher Ag^{+} concentrations the plasmonic resonances are localized at higher wavelengths.

Later, we tested the influence of pH in a JC-1 solution with CTAB presence. The absorbance and PL responses showed the presence of enhancement of the benzimidazole response. In Figure 7 **(a)**, it is possible to observe the presence of benzimidazole

response at 300 nm at pH=7. Once HCl is added, decreasing the pH value, this response increases, and the monomer response at 510 nm disappears. It is remarkable that in absorbance signals the most abrupt increase takes place at [HCl] = 1 mM, later the increments are almost not appreciable.

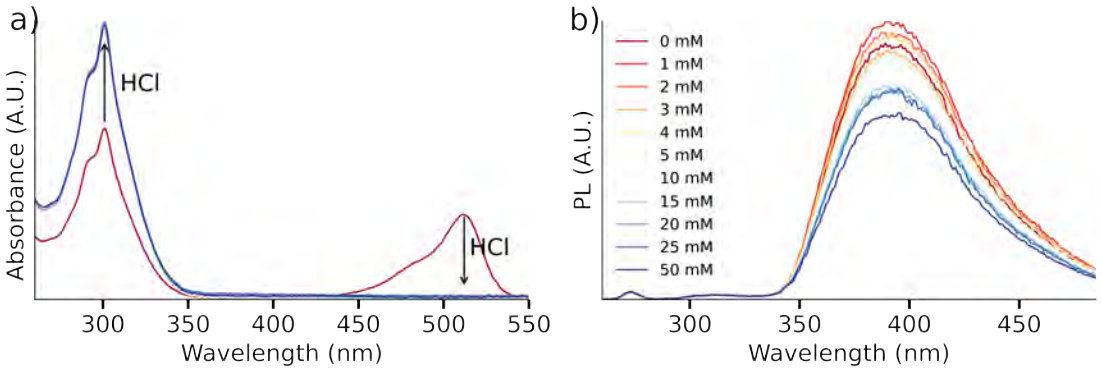

Figure 7: Effect of low pH in JC-1 absorbance and PL. **(a)** UV-vis spectra of JC-1 at decreasing pH, the benzimidazole response (300 nm) increases. **(b)** PL spectra showing the benzimidazole response at 400 nm, the maximum intensity was reached at [HCl] = 1 mM, then the intensity slowly decreases with HCl presence. For these measurements, excitation at 250 nm was applied.

Coupling strength analysis

The measured spectra for different HCl concentrations are presented in this section. After the HCl addition, the evolution of the plexcitonic systems was tracked through the absorbance spectra to evaluate the influence of HCl in the decoupling rate. The coupling strength of each stage of the system was analyzed using the theory given by Equation 1.9 using the ω and Γ values of the system's components (plasmonic and excitonic response). From this, the obtained theoretical spectra are presented for each HCl concentration in the following figures.

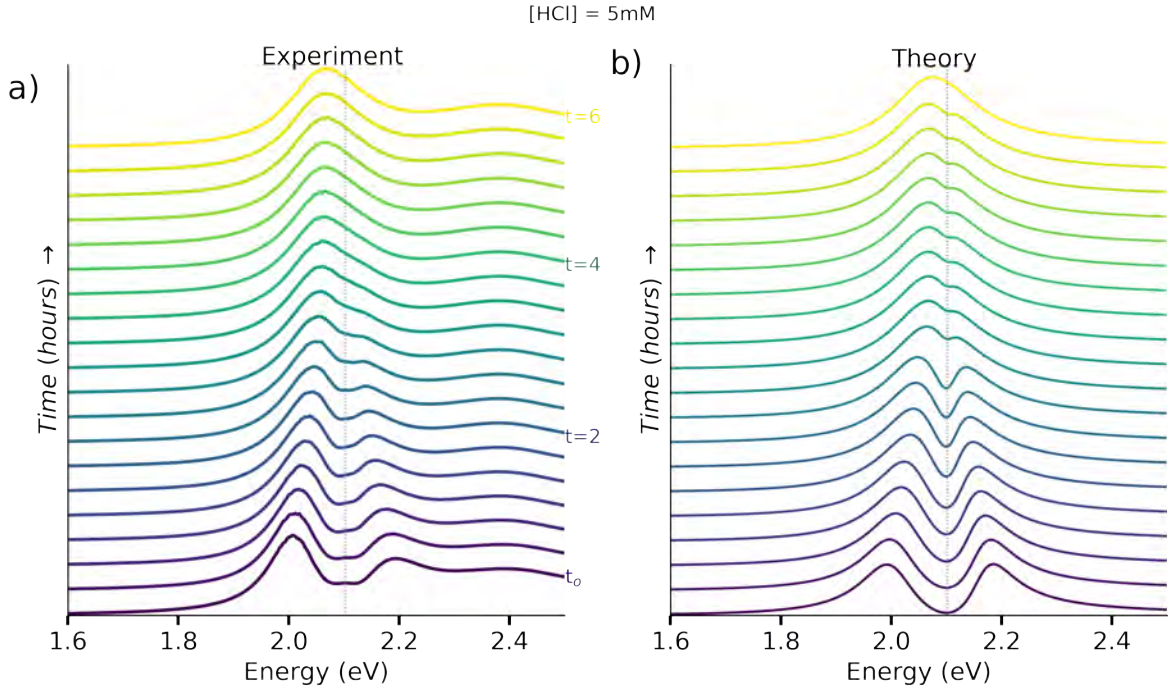

Figure 8: Effect of acid concentration on decoupling speed for [HCL]= 5 mM. **(a)** Time-dependent UV-Vis-NIR spectra of the decoupling process taken in the interval of 20 minutes during 6 hours. **(b)** Modeled spectra response for the decoupling phase used to estimate g during the process.

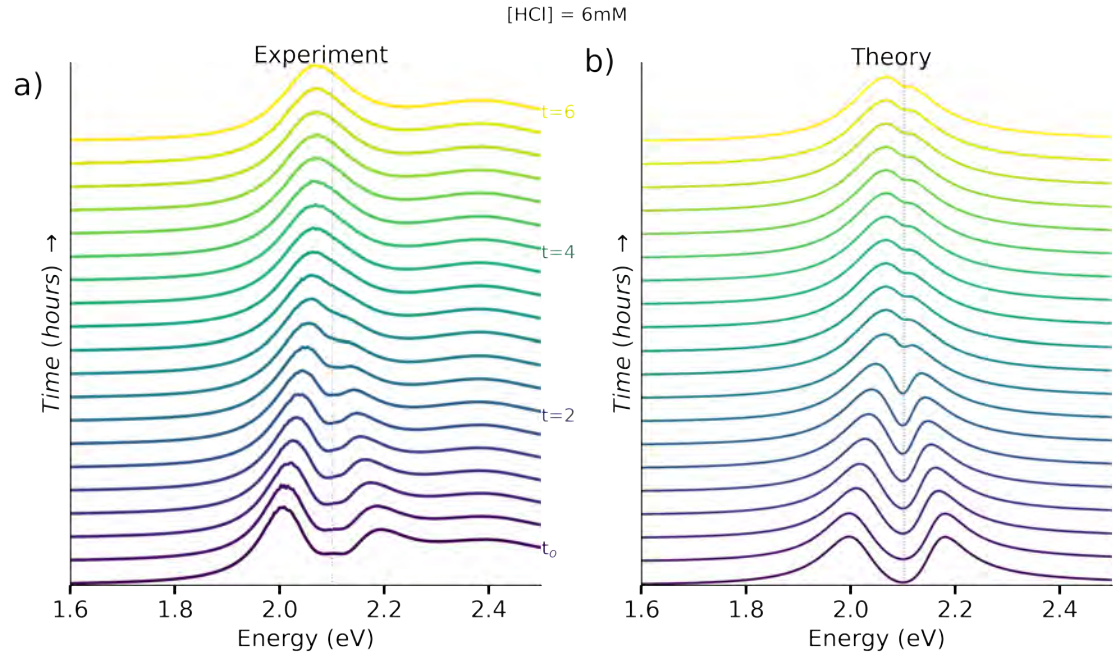

Figure 9: Effect of acid concentration on decoupling speed for [HCL]= 6 mM. **(a)** Time-dependent UV-Vis-NIR spectra of the decoupling process taken in the interval of 20 minutes during 6 hours. **(b)** Modeled spectra response for the decoupling phase used to estimate g during the process.

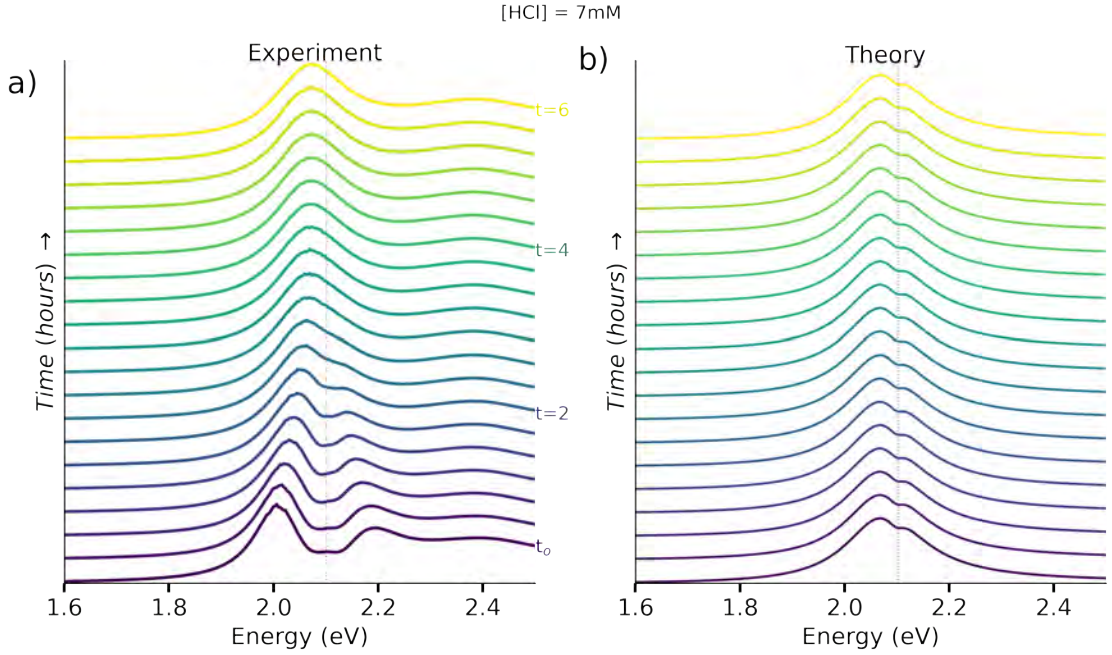

Figure 10: Effect of acid concentration on decoupling speed for [HCL]= 7 mM. **(a)** Time-dependent UV-Vis-NIR spectra of the decoupling process taken in the interval of 20 minutes during 6 hours. **(b)** Modeled spectra response for the decoupling phase used to estimate g during the process.

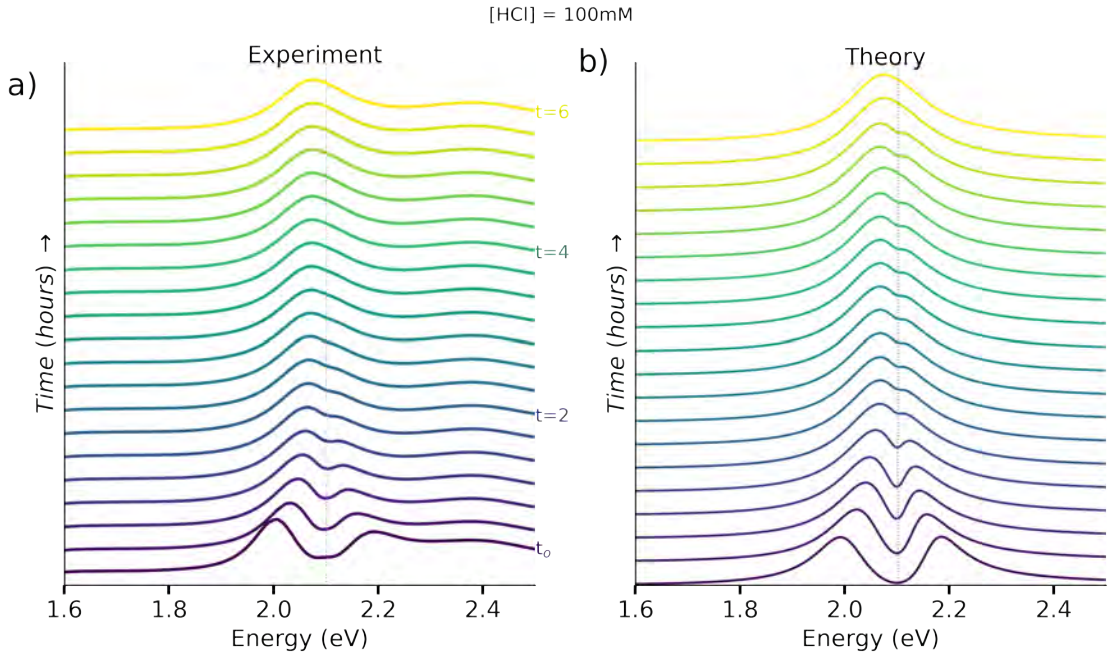

Figure 11: Effect of acid concentration on decoupling speed for [HCL]= 100 mM. **(a)** Time-dependent UV-Vis-NIR spectra of the decoupling process taken in the interval of 20 minutes during 6 hours. **(b)** Modeled spectra response for the decoupling phase used to estimate g during the process.

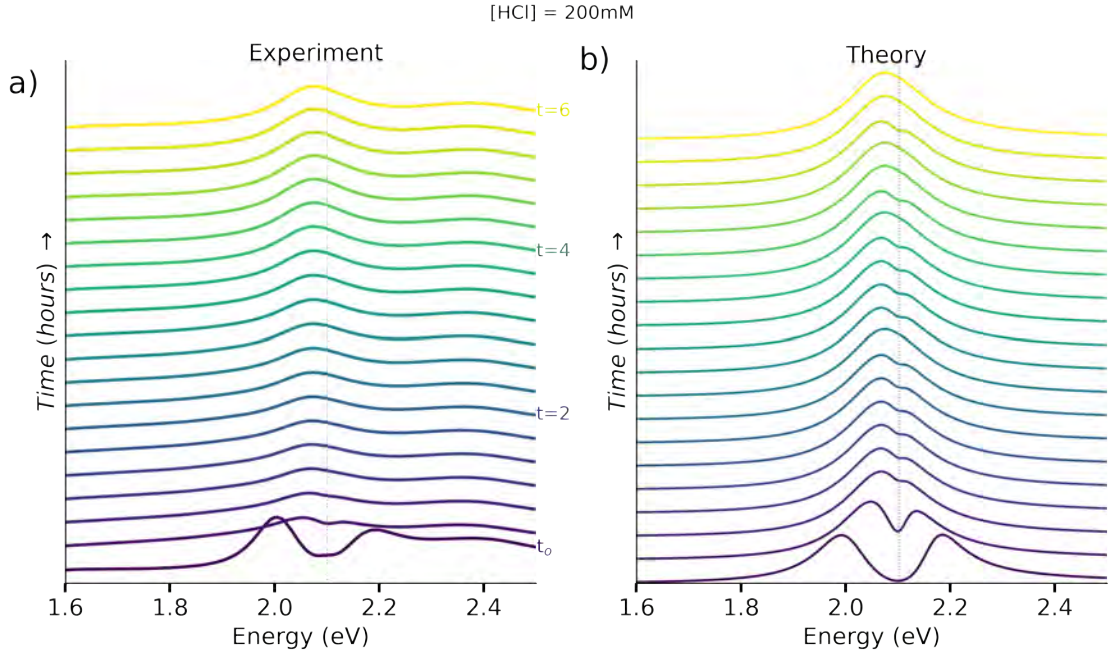

Figure 12: Effect of acid concentration on decoupling speed for [HCL]= 200 mM. **(a)** Time-dependent UV-Vis-NIR spectra of the decoupling process taken in the interval of 20 minutes during 6 hours. **(b)** Modeled spectra response for the decoupling phase used to estimate g during the process.

List of publications

Publications in preparation

- **Alba Jumbo-Nogales**, Marek Grzelczak, Yury P. Rakovich, *The rise of strong coupling in photocatalysis: How far can we go?*

- **Alba Jumbo-Nogales**, Anish Rao, Adam Olejniczak, Marek Grzelczak, Yury P. Rakovich, *A Reversible Plexcitonic System based on coupled gold nanoparticles/J-aggregates*

- Adam Olejniczak, Nikos Iliopoulos, **Alba Jumbo-Nogales**, Rubén Esteban Llorente, Javier Aizpurúa, Rainer Hillenbrand, Yury P. Rakovich, *Revealing of Exciton-Polariton Dark Modes in J-aggregate layer by Whispering Gallery Modes of Dielectric Microcavities*

Published articles

- **Alba Jumbo-Nogales**, Anish Rao, Adam Olejniczak, Marek Grzelczak, Yury P Rakovich, *Unveiling the Synergy of Coupled Gold Nanoparticles and J-aggregates in Plexcitonic Systems for Enhanced Photochemical Applications*, Nanomaterials, 14(1), 35, 2024.

- **Alba Jumbo-Nogales**, Victor Krivenkov, K Rusakov, A. Urban, Marek Grzelczak, Yury P Rakovich, *Cross Determination of Exciton Coherence Length in J-aggregates*, The journal of physical chemistry letters, 13, 43, 10198–10206, 2022

- Andrea Rogolino, Nathalie Claes, Judit Cizaurre, Aimar Marauri, **Alba Jumbo-Nogales**, Zuzanna Lawera, Joscha Kruse, María Sanromán-Iglesias, Ibai Zarketa, Unai Calvo, Elisa Jimenez-Izal, Yury P Rakovich, Sara Bals, Jon M Matxain, Marek Grzelczak, *Metal–Polymer Heterojunction in Colloidal-Phase*

Plasmonic Catalysis, The journal of physical chemistry letters 13 (10), 2264-2272, 2022

Bibliography

[1] Lily Filson. *Light Theory*, pages 1921–1923. Springer International Publishing, Cham, 2022. See page 1.

[2] M. Suhail Zubairy. *A Very Brief History of Light*, pages 3–24. Springer International Publishing, Cham, 2016. See page 1.

[3] Sungju Yu and Prashant K. Jain. Selective branching of plasmonic photosynthesis into hydrocarbon production and hydrogen generation. *ACS Energy Letters*, 4(9):2295–2300, 2019. See page 2.

[4] Jino George and Jaibir Singh. Polaritonic chemistry: Band-selective control of chemical reactions by vibrational strong coupling. *ACS Catalysis*, 13(4):2631–2636, 2023. See page 2.

[5] Yueyue Dong, Canyu Hu, Hailong Xiong, Ran Long, and Yujie Xiong. Plasmonic catalysis: New opportunity for selective chemical bond evolution. *ACS Catalysis*, 13(10):6730–6743, 2023. See page 2.

[6] Stefan A. Maier (auth.). *Plasmonics: Fundamentals and Applications*. Springer, 1 edition, 2007. See pages 3, 4.

[7] Catherine Louis; Olivier Pluchery. *Gold Nanoparticles for Physics, Chemistry and Biology*. Imperial College Press, 2012. See page 4.

[8] Yoon-Min Lee, Seong-Eun Kim, and Jeong-Eun Park. Strong coupling in plasmonic metal nanoparticles. *Nano Convergence*, 10(1):34, July 2023. See pages 4, 42.

[9] Prashant K. Jain, Wenyu Huang, and Mostafa A. El-Sayed. On the universal scaling behavior of the distance decay of plasmon coupling in metal nanoparticle pairs: A plasmon ruler equation. *Nano Letters*, 7(7):2080–2088, 2007. See page 4.

[10] Olivier Pluchery, Yoann Prado, and William Watkins. A complete explanation of the plasmonic colours of gold nanoparticles and of the bichromatic effect. *J. Mater. Chem. C*, pages –, 2023. See page 4.

[11] Clemens Burda, Xiaobo Chen, Radha Narayanan, and Mostafa A. El-Sayed. Chemistry and properties of nanocrystals of different shapes. *Chemical Reviews*, 105(4):1025–1102, 2005. See page 4.

[12] Younan Xia, Xiaohu Xia, and Hsin-Chieh Peng. Shape-controlled synthesis of colloidal metal nanocrystals: Thermodynamic versus kinetic products. *Journal of the American Chemical Society*, 137(25):7947–7966, 2015. See pages 4, 8.

[13] Susie Eustis and Mostafa A. El-Sayed. Why gold nanoparticles are more precious than pretty gold: Noble metal surface plasmon resonance and its enhancement of the radiative and nonradiative properties of nanocrystals of different shapes. *Chem. Soc. Rev.*, 35:209–217, 2006. See page 4.

[14] Jyoti Boken, Parul Khurana, Sheenam Thatai, Dinesh Kumar, and Surendra Prasad. Plasmonic nanoparticles and their analytical applications: A review. *Applied Spectroscopy Reviews*, 52(9):774–820, 2017. See page 4.

[15] Nikolai G. Khlebtsov and Lev A. Dykman. Optical properties and biomedical applications of plasmonic nanoparticles. *J. Quant. Spectrosc. Radiat. Transf.*, 111(1):1–35, 2010. See pages 5, 42.

[16] Roland P. M. Höller, Christian Kuttner, Martin Mayer, Ruosong Wang, Martin Dulle, Rafael Contreras-Cáceres, Andreas Fery, and Luis M. Liz-Marzán. Colloidal superstructures with triangular cores: Size effects on sers efficiency. *ACS Photonics*, 7(7):1839–1848, 2020. See page 5.

[17] Mingzhao Liu, Philippe Guyot-Sionnest, Tae-Woo Lee, and Stephen K. Gray. Optical properties of rodlike and bipyramidal gold nanoparticles from three-dimensional computations. *Phys. Rev. B*, 76:235428, Dec 2007. See pages 5, 98, and 99.

[18] Jorge Pérez-Juste, Isabel Pastoriza-Santos, Luis M. Liz-Marzán, and Paul Mulvaney. Gold nanorods: Synthesis, characterization and applications. *Coordination Chemistry Reviews*, 249(17):1870–1901, 2005. See page 7.

[19] Luis M Liz-Marzán. Nanometals: Formation and color. *Materials Today*, 7(2):26–31, 2004. See page 7.

[20] Marek Grzelczak and Luis M. Liz-Marzán. The relevance of light in the formation of colloidal metal nanoparticles. *Chem. Soc. Rev.*, 43:2089–2097, 2014. See page 8.

[21] Ana Sánchez-Iglesias, Naomi Winckelmans, Thomas Altantzis, Sara Bals, Marek Grzelczak, and Luis M. Liz-Marzán. High-yield seeded growth of monodisperse pentatwinned gold nanoparticles through thermally induced seed twinning. *J. Am. Chem. Soc.*, 139(1):107–110, 2017. See pages 8, 43, 62, and 79.

[22] Mingzhao Liu and Philippe Guyot-Sionnest. Mechanism of silver(i)-assisted growth of gold nanorods and bipyramids. *The Journal of Physical Chemistry B*, 109(47):22192–22200, 2005. See page 8.

[23] Fumitaka Mafuné and Tamotsu Kondow. Formation of small gold clusters in solution by laser excitation of interband transition. *Chemical Physics Letters*, 372(1):199–204, 2003. See page 8.

[24] Adam Olejniczak, Yury Rakovich, and Victor Krivenkov. Advancements and challenges in plasmon-exciton quantum emitters based on colloidal quantum dots, 2024. See page 10.

[25] Lukas Novotny and Bert Hecht. *Quantum emitters*, page 282–312. Cambridge University Press, 2012. See page 10.

[26] Aron Walsh, John Buckeridge, C. Richard A. Catlow, Adam J. Jackson, Thomas W. Keal, Martina Miskufova, Paul Sherwood, Stephen A. Shevlin, Mathew B. Watkins,

Scott M. Woodley, and Alexey A. Sokol. Limits to doping of wide band gap semiconductors. *Chemistry of Materials*, 25(15):2924–2926, 2013. See page 10.

[27] M. Liu, A.H. Kitai, and P. Mascher. Point defects and luminescence centres in zinc oxide and zinc oxide doped with manganese. *Journal of Luminescence*, 54(1):35–42, 1992. See page 10.

[28] Joseph R. Lakowicz. *New York*. Springer, 2007. See pages 10, 13.

[29] S. Swaminathan. Gfp: the green revolution. *Nat. Cell. Biol.*, 11((Suppl 1)):S20, 2009. See page 11.

[30] Elizabeth A. Specht, Esther Braselmann, and Amy E. Palmer. A critical and comparative review of fluorescent tools for live-cell imaging. *Annual Review of Physiology*, 79(1):93–117, 2017. See page 11.

[31] H.A. Shindy. Fundamentals in the chemistry of cyanine dyes: A review. *Dyes Pigm.*, 145:505–513, 2017. See pages 11, 12.

[32] Heinrich Zollinger. *Color Chemistry : Syntheses, Properties, and Applications of Organic Dyes and Pigments*. Weinheim, 1991. See page 11.

[33] Ghodsi Mohammadi Ziarani, Razieh Moradi, Negar Lashgari, and Hendrik G. Kruger. Chapter 8 - cyanine dyes. In Ghodsi Mohammadi Ziarani, Razieh Moradi, Negar Lashgari, and Hendrik G. Kruger, editors, *Metal-Free Synthetic Organic Dyes*, pages 127–152. Elsevier, 2018. See page 11.

[34] A.H. Herz. Aggregation of sensitizing dyes in solution and their adsorption onto silver halides. *Adv. Colloid Interface Sci.*, 8:237–298, 1977. See pages 11, 36, and 102.

[35] Frank Würthner, Theo E. Kaiser, and Chantu R. Saha-Möller. J-aggregates: From serendipitous discovery to supramolecular engineering of functional dye materials. *Angew. Chem. Int. Ed.*, 50(15):3376–3410, 2011. See pages 11, 42.

[36] Christopher D. Gabbutt, Lucy V. Gibbons, B. Mark Heron, and Suresh B. Kolla. The intramolecular capture of thermally generated merocyanine dyes derived from naphthopyrans: Photochromism of 5-(diarylhydroxymethyl)-2h-naphtho[1,2-b]pyrans. *Dyes and Pigments*, 92(3):995–1004, 2012. See page 11.

[37] Xiaoni Fang, Yongzan Zheng, Yaokai Duan, Yang Liu, and Wenwan Zhong. Recent advances in design of fluorescence-based assays for high-throughput screening. *Analytical Chemistry*, 91(1):482–504, 2019. See page 11.

[38] Xin Yan, Xinqian Chen, Zhiying Shan, and Lanrong Bi. Innovative cyanine-based fluorescent dye for targeted mitochondrial imaging and its utility in whole-brain visualization. *ACS Omega*, 0(0):null, 2024. See page 11.

[39] Jun-Feng Xiang, Yan-Xia Liu, Dan Sun, Su-Juan Zhang, Yi-Le Fu, Xiang-Han Zhang, and Lan-Ying Wang. Synthesis, spectral properties of rhodanine complex merocyanine dyes as well as their effect on k562 leukemia cells. *Dyes and Pigments*, 93(1):1481–1487, 2012. See page 12.

[40] Rian Aderne, Karen Strassel, Sandra Jenatsch, Matthias Diethelm, Roland Hany, Frank Nüesch, Rafael dos Santos Carvalho, Cristiano Legnani, and Marco Cremona. Near-infrared absorbing cyanine dyes for all-organic optical upconversion devices. *Organic Electronics*, 74:96–102, 2019. See page 12.

[41] Vera C. Keil, Frank Funke, Andre Zeug, Detlev Schild, and Michael Müller. Ratiometric high-resolution imaging of JC-1 fluorescence reveals the subcellular hetero-

geneity of astrocytic mitochondria. *Pflügers Archiv - European Journal of Physiology*, 462(5):693–708, November 2011. See pages 12, 64.

[42] Adarsh B. Vasista and William L. Barnes. Strong coupling of multimolecular species to soft microcavities. *J. Phys. Chem. Lett.*, 13(4):1019–1024, 2022. See pages 13, 48.

[43] Leon Koch, Roland Pollak, Simon Ebbinghaus, and Klaus Huber. A comparative study on cyanine dyestuffs as sensor candidates for macromolecular crowding in vitro and in vivo. *Biosensors*, 13(7), 2023. See pages 13, 46.

[44] Kevin Chevrier, Jean-Michel Benoit, Clementine Symonds, Julien Paparone, Julien Laverdant, and Joel Bellessa. Organic exciton in strong coupling with long-range surface plasmons and waveguided modes. *ACS Photonics*, 5(1):80–84, 2018. See page 13.

[45] Moll J., Daehne S., Durrant JR., and Wiersma DA. Excition dynamics in the j-aggregates of a carbocyanine dye. *Journal of Fluorescence*, 4((1)):57–59, 1994. See page 13.

[46] G. Scheibe. Über die veränderlichkeit der absorptionsspektren in lösungen und die nebenvalenzen als ihre ursache. *Angew. Chem. Int. Ed.*, 50:212–219, 1937. See pages 13, 23.

[47] J. R. Durrant J. Moll, S.Daehne and D. A. Wiersma. Optical dynamics of excitons in j aggregates of a carbocyanine dye. *J. Chem. Phys.*, 102:6362–6370, 1995. See pages 13, 36, and 103.

[48] Henk Fidder, Jacob Terpstra, and Douwe A. Wiersma. Dynamics of frenkel excitons in disordered molecular aggregates. *J. Chem. Phys.*, 94:6895–6907, 1991. See pages 13, 15, 23, 36, and 102.

[49] Vladimir V. Egorov. Quantum-classical mechanics: Luminescence spectra in polymethine dyes and j-aggregates. nature of the small stokes shift. *Results in Physics*, 13:102252, 2019. See page 14.

[50] Vladimir Agranovich. *Excitations in Organic Solids (International Series of Monographs on Physics)*. Oxford Science Publications, 2009. See pages 14, 15, and 16.

[51] G. Franco Bassani and V. M. Agranovich. *Electronic Excitations in Organic Based Nanostructures*. Academic Press, 2003. See pages 14, 15, and 30.

[52] Darius Abramavicius, Vytautas Butkus, and Leonas Valkunas. Chapter 1 - interplay of exciton coherence and dissipation in molecular aggregates. In Uli Würfel, Michael Thorwart, and Eicke R. Weber, editors, *Quantum Efficiency in Complex Systems, Part II*, volume 85 of *Semiconductors and Semimetals*, pages 3–46. Elsevier, 2011. See pages 14, 41.

[53] B.P. Zakharchenya and S.A. Permogorov. Excitons in crystals. In Franco Bassani, Gerald L. Liedl, and Peter Wyder, editors, *Encyclopedia of Condensed Matter Physics*, pages 171–179. Elsevier, Oxford, 2005. See page 14.

[54] Valey F. Kamalov, Irina A. Struganova, and Keitaro Yoshihara. Temperature dependent radiative lifetime of j-aggregates. *J. Phys. Chem.*, 100:8640–8644, 1996. See pages 15, 33, and 36.

[55] Kamalika Das, Jyotirban Dey, Mrigank Singh Verma, Manish Kumar, and Manabendra Chandra. Probing the role of oscillator strength and charge of exciton forming

molecular j-aggregates in controlling nanoscale plasmon–exciton interactions. *Phys. Chem. Chem. Phys.*, 22:20499–20506, 2020. See pages 15, 37.

[56] Frank C. Spano. The spectral signatures of frenkel polarons in h- and j-aggregates. *Accounts of Chemical Research*, 43(3):429–439, 2010. See pages 15, 16.

[57] I. G. Scheblykin, O. Yu. Sliusarenko, L. S. Lepnev, A. G. Vitukhnovsky, and M. Van der Auweraer. Excitons in molecular mggregates of 3,3‘-bis-[3-sulfopropyl]-5,5‘-dichloro-9- ethylthiacarbocyanine (thiats): temperature dependent properties. *J. Phys. Chem. B*, 105:4636–4646, 2001. See pages 16, 23.

[58] Lisette D Bakalis and Jasper Knoester. Linear absorption as a tool to measure the exciton delocalization length in molecular assemblies. *J. Lumin.*, 87-89:66–70, 2000. See pages 16, 23, and 36.

[59] Lisette D. Bakalis and Jasper Knoester. Can the exciton delocalization length in molecular aggregates be determined by pump-probe spectroscopy? *J. Lumin.*, 83-84:115–119, 1999. See pages 16, 35, and 36.

[60] Lisette D. Bakalis and Jasper Knoester. Pump-probe spectroscopy and the exciton delocalization length in molecular aggregates. *J. Phys. Chem. B*, 103:6620–6628, 1999. See pages 16, 35.

[61] Ajay P. Manuel, Aaron Kirkey, Najia Mahdi, and Karthik Shankar. Plexcitonics - fundamental principles and optoelectronic applications. *J. Mater. Chem. C*, 7:1821–1853, 2019. See pages 16, 21, 41, and 50.

[62] Qian Zhao, Wen-Jie Zhou, Yan-Hui Deng, Ya-Qin Zheng, Zhong-Hong Shi, Lay Kee Ang, Zhang-Kai Zhou, , and Lin Wu. Plexcitonic strong coupling: unique features, applications, and challenges. *J. Phys. D: Appl. Phys.*, 55:203002, 2022. See pages 16, 41.

[63] Yangkyu Kim, Aleksandr Barulin, Sangwon Kim, Luke P. Lee, and Inki Kim. Recent advances in quantum nanophotonics: plexcitonic and vibro-polaritonic strong coupling and its biomedical and chemical applications. *Nanophotonics*, 12(3):413–439, 2023. See pages 16, 18, and 42.

[64] Songyan Hou, Landobasa Y. M. Tobing, Xingli Wang, Zhenwei Xie, Junhong Yu, Jin Zhou, Daohua Zhang, Cuong Dang, Philippe Coquet, Beng Kang Tay, Muhammad Danang Birowosuto, Edwin Hang Tong Teo, and Hong Wang. Manipulating coherent light–matter interaction: Continuous transition between strong coupling and weak coupling in mos2 monolayer coupled with plasmonic nanocavities. *Adv. Opt. Mater.*, 7(22):1900857, 2019. See pages 17, 19.

[65] Manuel Hertzog, Mao Wang, Jürgen Mony, and Karl Börjesson. Strong light–matter interactions: a new direction within chemistry. *Chem. Soc. Rev.*, 48:937–961, 2019. See pages 17, 19.

[66] Nicola Peruffo, Gabriel Gil, Stefano Corni, Fabrizio Mancin, and Elisabetta Collini. Selective switching of multiple plexcitons in colloidal materials: directing the energy flow at the nanoscale. *Nanoscale*, 13:6005–6015, 2021. See pages 17, 20.

[67] Matthew Pelton, S. David Storm, and Haixu Leng. Strong coupling of emitters to single plasmonic nanoparticles: exciton-induced transparency and rabi splitting. *Nanoscale*, 11:14540–14552, 2019. See pages 18, 19, 41, 53, 66, and 71.

[68] P Törmä and W L Barnes. Strong coupling between surface plasmon polaritons and emitters: a review. *Reports on Progress in Physics*, 78(1):013901, dec 2014. See pages 18, 19, and 61.

[69] Michael Tavis and Frederick W. Cummings. Exact solution for an n-molecule—radiation-field hamiltonian. *Phys. Rev.*, 170:379–384, Jun 1968. See page 18.

[70] Xiaohua Wu, Stephen K. Gray, and Matthew Pelton. Quantum-dot-induced transparency in a nanoscale plasmonic resonator. *Opt. Express*, 18(23):23633–23645, Nov 2010. See page 19.

[71] Qinglan Huang, Taylor D. Canady, Rohit Gupta, Nantao Li, Srikanth Singamaneni, and Brian T. Cunningham. Enhanced plasmonic photocatalysis through synergistic plasmonic–photonic hybridization. *ACS Photonics*, 7(8):1994–2001, 2020. See page 19.

[72] Anne-Laure Baudrion, Antoine Perron, Alessandro Veltri, Alexandre Bouhelier, Pierre-Michel Adam, and Renaud Bachelot. Reversible strong coupling in silver nanoparticle arrays using photochromic molecules. *Nano Letters*, 13(1):282–286, 2013. See pages 20, 41.

[73] Jorge Cuadra, Denis G. Baranov, Martin Wersäll, Ruggero Verre, Tomasz J. Antosiewicz, and Timur Shegai. Observation of tunable charged exciton polaritons in hybrid monolayer ws2-plasmonic nanoantenna system. *Nano Letters*, 18(3):1777–1785, 2018. See pages 20, 21.

[74] Jinxiu Wen, Hao Wang, Weiliang Wang, Zexiang Deng, Chao Zhuang, Yu Zhang, Fei Liu, Juncong She, Jun Chen, Huanjun Chen, Shaozhi Deng, and Ningsheng Xu. Room-temperature strong light–matter interaction with active control in single plasmonic nanorod coupled with two-dimensional atomic crystals. *Nano Letters*, 17(8):4689–4697, 2017. See pages 20, 21.

[75] Linhan Lin, Mingsong Wang, Xiaoling Wei, Xiaolei Peng, Chong Xie, and Yuebing Zheng. Photoswitchable rabi splitting in hybrid plasmon–waveguide modes. *Nano Letters*, 16(12):7655–7663, 2016. See pages 20, 21.

[76] Molly A. May, David Fialkow, Tong Wu, Kyoung-Duck Park, Haixu Leng, Jaron A. Kropp, Theodosia Gougousi, Philippe Lalanne, Matthew Pelton, and Markus B. Raschke. Nano-cavity qed with tunable nano-tip interaction. *Advanced Quantum Technologies*, 3(2):1900087, 2020. See page 21.

[77] Heiko Groß, Joachim M. Hamm, Tommaso Tufarelli, Ortwin Hess, and Bert Hecht. Near-field strong coupling of single quantum dots. *Science Advances*, 4(3):eaar4906, 2018. See page 21.

[78] Audrey Berrier, Ruud Cools, Christophe Arnold, Peter Offermans, Mercedes Crego-Calama, Sywert H. Brongersma, and Jaime Gómez-Rivas. Active control of the strong coupling regime between porphyrin excitons and surface plasmon polaritons. *ACS Nano*, 5(8):6226–6232, 2011. See page 21.

[79] Nikita Nefedkin, Evgeny Andrianov, and Alexey Vinogradov. The role of strong coupling in the process of photobleaching suppression. *The Journal of Physical Chemistry C*, 124(33):18234–18242, 2020. See page 21.

[80] Thomas Hendel, Victor Krivenkov, Ana Sánchez-Iglesias, Marek Grzelczak, and Yury P. Rakovich. Strongly coupled exciton-plasmon nanohybrids reveal extraor-

dinary resistance to harsh environmental stressors: temperature, ph and irradiation. *Nanoscale*, 12:16875–16883, 2020. See pages 22, 41, 57, 61, 64, 75, and 77.

[81] Victor Krivenkov, Pavel Samokhvalov, Igor Nabiev, and Yury P. Rakovich. ph-sensing platform based on light–matter coupling in colloidal complexes of silver nanoplates and j-aggregates. *The Journal of Physical Chemistry C*, 125(3):1972–1979, 2021. See pages 22, 77.

[82] Battulga Munkhbat, Martin Wersäll, Denis G. Baranov, Tomasz J. Antosiewicz, and Timur Shegai. Suppression of photo-oxidation of organic chromophores by strong coupling to plasmonic nanoantennas. *Sci. Adv.*, 4(7):eaas9552, 2018. See pages 22, 61, 74, and 76.

[83] Vanessa N. Peters, Md Omar Faruk, Joshua Asane, Rohan Alexander, D'angelo A. Peters, Srujana Prayakarao, Sangeeta Rout, and M. A. Noginov. Effect of strong coupling on photodegradation of the semiconducting polymer p3ht. *Optica*, 6(3):318–325, Mar 2019. See page 22.

[84] Francisco J. Garcia-Vidal, Cristiano Ciuti, and Thomas W. Ebbesen. Manipulating matter by strong coupling to vacuum fields. *Science*, 373(6551):eabd0336, 2021. See page 22.

[85] Frank Würthner, Theo E. Kaiser, and Chantu R. Saha-Möller. J-aggregates: from serendipitous discovery to supramolecular engineering of functional dye materials. *Angew. Chem. Int. Ed.*, 50:3376–3410, 2011. See page 23.

[86] T Kobayashi. *J-Aggregates*. WORLD SCIENTIFIC, Singapore, 1996. See page 23.

[87] E. Jelley. Spectral absorption and fluorescence of dyes in the molecular state. *Nature*, 138:1009–1010, 1936. See page 23.

[88] B. Kopainsky and W. Kaiser. Ultrafast transient processes of monomers, dimers, and aggregates of pseudoisocyanine chloride (pic). *Chem. Phys. Lett.*, 88:357–361, 1982. See pages 23, 36, and 102.

[89] Alexander Humeniuk, Roland Mitrić, and Vlasta Bonačić-Koutecký. Size dependence of non-radiative decay rates in j-aggregates. *J. Phys. Chem. A*, 124:10143–10151, 2020. See pages 23, 31, 33, and 36.

[90] Huang Kun and Rhys Avril. Theory of light absorption and non-radiative transitions in f-centres. *Proc. R. Soc. Lond.*, 21:424–429, 1950. See page 23.

[91] Mathijs de Jong, Luis Seijo, Andries Meijerink, and Freddy T. Rabouw. Resolving the ambiguity in the relation between stokes shift and huang–rhys parameter. *Phys. Chem. Chem. Phys.*, 17:16959–16969, 2015. See pages 23, 31, and 36.

[92] Markus Grabolle, Monika Spieles, Vladimir Lesnyak, Nikolai Gaponik, Alexander Eychmüller, and Ute Resch-Genger. Determination of the fluorescence quantum yield of quantum dots: suitable procedures and achievable uncertainties. *Anal. Chem.*, 81:6285–6294, 2009. See pages 25, 26, and 27.

[93] R.F. Kubin and A.N. Fletcher. Fluorescence quantum yields of some rhodamine dyes. *Journal of Luminescence*, 27(4):455–462, 1982. See page 26.

[94] Martin Reers, Stephen T. Smiley, Cristina Mottola-Hartshorn, Ann Chen, Mei Lin, and Lan Bo Chen. [29] mitochondrial membrane potential monitored by jc-1 dye. In *Mitochondrial Biogenesis and Genetics Part A*, volume 260 of *Methods in Enzymology*, pages 406–417. Academic Press, 1995. See pages 28, 64.

[95] Weiguang Mao, Xing Xian Yu, Alan Zhong, Wenlu Li, Jennifer Brush, Steven W Sherwood, Sean H Adams, and Guohua Pan. Ucp4, a novel brain-specific mitochondrial protein that reduces membrane potential in mammalian cells. *FEBS Letters*, 443(3):326–330, 1999. See page 28.

[96] I. K. Katrunov, A. V. Sorokin, S. L. Yefimova, and Yu. V. Malyukin. Manifestation of exciton-lattice interaction in j-aggregates. *Mol. Cryst. Liq. Cryst.*, 535(1):57–63, 2011. See pages 29, 30.

[97] V.A. Malyshev. Localization length of one-dimensional exciton and low-temperature behaviour of radiative lifetime of j-aggregated dye solutions. *J. Lumin.*, 55:225–230, 1993. See pages 29, 30.

[98] Gleb Ya. Guralchuk, Ivan K. Katrunov, Roman S. Grynyov, Alexander V. Sorokin, Svetlana L. Yefimova, Igor A. Borovoy, and Yuri V. Malyukin. Anomalous surfactant-induced enhancement of luminescence quantum yield of cyanine dye j-aggregates. *J. Phys. Chem. C*, 112:14762–14768, 2008. See page 29.

[99] Andrei Tokmakoff. Excitons in Molecular Aggregates. In *Time dependent quantum mechanics and spectroscopy*. University of Chicago, 2020. See page 30.

[100] Jörg Pieper and Arvi Freiberg. *Electron–phonon and exciton–phonon coupling in light harvesting, insights from line-narrowing spectroscopies*, pages 45–77. Springer New York, New York, 2014. See page 31.

[101] Philip A. Shields, Robin J Nicholas, Nicolas Grandjean, and Jean Massies. Magnetophotoluminescence of gan/alxga1-xn quantum wells: valence band reordering and excitonic binding energies. *Phys. Rev. B*, 63:5319, 2001. See page 31.

[102] Igor V. Kukushkin, Nicolas J Pulsford, Klaus von Klitzing, K. H. Ploog, and Vladislav B. Timofeev. Magnetooptics of the incompressible fermi liquid and of the wigner solid. *Surf. Sci.*, 263:30–38, 1992. See page 31.

[103] Hajime Yamagata and Frank C. Spano. Strong photophysical similarities between conjugated polymers and j-aggregates. *J. Phys. Chem. Lett.*, 5:622–632, 2014. See pages 32, 36.

[104] E.G. McRae and M. Kasha. The molecular exciton model. In *Physical processes in radiation biology*, pages 23–42. A P., New York, 1964. See pages 33, 36.

[105] Eion G. McRae and Michael Kasha. Enhancement of phosphorescence ability upon aggregation of dye molecules. *Chem. Phys.*, 28:721–722, 1958. See pages 33, 36.

[106] H. Stiel, K. Teuchner, W. Becker, W. Freyer, and S. Dähne. Fluorescence lifetime studies of pseudoisocyanine j-aggregates in the subnanosecond range. *J. Mol. Struct.*, 114:351–354, 1984. See page 34.

[107] Valey F. Kamalov, Irina A. Struganova, Tadaaki Tani, and Keitaro Yoshihara. Temperature dependence of superradiant emission of bic j-aggregates. *Chem. Phys. Lett.*, 220:257–261, 1994. See pages 34, 36, and 102.

[108] Jun-Feng Xiang, Xiaorong Yang, Ciping Chen, Yalin Tang, Wenpeng Yan, and Guangzhi Xu. Effects of nacl on the j-aggregation of two thiacarbocyanine dyes in aqueous solutions. *J. Colloid Interface Sci.*, 258:198–205, 2003. See page 34.

[109] Thomas Simon, Dimitry Melnikau, Ana Sánchez-Iglesias, Marek Grzelczak, Luis M. Liz-Marzán, Yury Rakovich, Jochen Feldmann, and Alexander S. Urban. Exploring the optical nonlinearities of plasmon-exciton hybrid resonances in coupled colloidal

nanostructures. *J. Phys. Chem. C*, 120(22):12226–12233, 2016. See pages 34, 36, and 64.

[110] E. Michelbacher. Abklingzeitmessungen an pseudoisocyanindiäthylchlorid mit einem phasenfluorometer mit 200 mhz-lichtmodulation:. *Z. Naturforsch. A*, 24:790–796, 1969. See pages 36, 102.

[111] R. E. Ballard and B. J. Gardner. The j-band of 1,1'-diethyl-9-methyl-4,5;4',5'-dibenzthiacarbocyanine chloride. *J. Chem. Soc. B*, pages 736–738, 1971. See pages 36, 102.

[112] D. A. van Burgel, M.; Wiersma and K. Duppen. The dynamics of one-dimensional excitons in liquids. *J. Chem. Phys.*, 102:20–33., 1995. See pages 36, 103.

[113] R. Gadonas R. Gagel and A. Laubereau. Evidence for biexcitons and dynamic stark effect in j-aggregates from femtosecond spectroscopy. *Chem. Phys. Lett.*, 217:228–233, 1994. See pages 36, 102.

[114] E.W. Knapp. Lineshapes of molecular aggregates, exchange narrowing and intersite correlation. *Chem. Phys.*, 85:73–82, 1984. See pages 36, 102.

[115] Christian Spitz and Siegfried Daehne. Architecture of j-aggregates studied by pressure-dependent absorption and fluorescence measurements. *Ber. Bunsenges. Phys. Chem.*, 102:738–744, 1998. See pages 36, 102.

[116] Steven De Boer and Douwe A. Wiersma. Dephasing-induced damping of superradiant emission in j-aggregates. *Chem. Phys. Lett.*, 165:45–53, 1990. See pages 36, 102.

[117] Claus Duschl, Wolfgang Frey, and Wolfgang Knoll. The crystalline structure of two-dimensional cyanine dye single crystals as revealed by electron diffraction. *Thin Solid Films*, 160:251–255, 1988. See pages 36, 102.

[118] Henk Fidder, Jasper Knoester, and Douwe A. Wiersma. Observation of the one-exciton to two-exciton transition in a j aggregate. *J. Chem. Phys.*, 98:6564–6566, 1993. See pages 36, 102.

[119] A. A. Ivanov, P. V. Mezentsev D. A. Akimov, A. I. Plekhanov, M. V. Alfimov, and A. M. Zheltikov. Pump-probe nonlinear absorption spectroscopy of molecular aggregates using chirped frequency-shifted light pulses from a photonic-crystal fiber. *Laser Phys.*, 16:965–969, 2006. See pages 36, 103.

[120] James R. Durrant, Jasper Knoester, and Douwe A. Wiersma. Local energetic disorder in molecular aggregates probed by the one-exciton to two-exciton transition. *Chem. Phys. Lett.*, 222:450–456, 1994. See pages 36, 102.

[121] B. Neumann and P. Pollmann. Aggregation of pseudoisocyanine chloride in aqueous solutions at high pressures. *Ber. Bunsenges. Phys. Chem.*, 100:15–19, 1996. See pages 36, 102.

[122] Y. Hamanaka, H. Kurasawa, A. Nakamura, Y. Uchiyama, K. Marumoto, and S. Kuroda. Femtosecond transient absorption study of merocyanine j-aggregates. *J. Lumin.*, 94-95:451–455, 2001. See pages 36, 102.

[123] S. S. Lampoura, C. Spitz, S. Dähne, J. Knoester, and K. Duppen. The optical dynamics of excitons in cylindrical j-aggregates. *J. Phys. Chem. B*, 106:3103–3111, 2002. See pages 36, 102.

[124] Dzmitry Melnikau, Diana Savateeva, Andrey Chuvilin, Rainer Hillenbrand, and Yury P. Rakovich. Whispering gallery mode resonators with j-aggregates. *Opt. Express*, 19:22280–22291, 2011. See pages 36, 102.

[125] Hiroo Nakahara, Kiyoshige Fukuda, Dietmar Moebius, and Hans Kuhn. Two-dimensional arrangement of chromophores in j aggregates of long-chain merocyanines and its effect on energy transfer in monolayer systems. *J. Phys. Chem.*, 90:6144–6148, 1986. See pages 36, 102.

[126] E. Daltrozzo, G. Scheibe, K. Gschwind, and F. Haimerl. Structure of the j-aggregates of pseudocyanine. *Photogr. Sci. Eng.*, 18:441–450, 1974. See pages 36, 102.

[127] S. Kobayashi and F. Sasaki. Ultrafast spectroscopy of picbr j aggregates: the dynamics of large coherence length exciton. *J. Lumin.*, 58:113–116, 1994. See pages 36, 102.

[128] Joseph M. Lanzafame, Annabel A. Muenter, and Donald V. Brumbaugh. The effect of j-aggregate size on photoinduced charge transfer processes for dye-sensitized silver halides. *Chem. Phys.*, 210:79–89, 1996. See pages 36, 102.

[129] Kaoru Minoshima, Makoto Taiji, Kazuhiko Misawa, and Takayoshi Kobayashi. Femtosecond nonlinear optical dynamics of excitons in j-aggregates. *Chem. Phys. Lett.*, 218:67–72, 1994. See pages 36, 102.

[130] Diana Savateeva, Dzmitry Melnikau, Vladimir Lesnyak, Nikolai Gaponik, and Yury P. Rakovich. Hybrid organic/inorganic semiconductor nanostructures with highly efficient energy transfer. *J. Mater. Chem.*, 22:10816–10820, 2012. See pages 36, 102.

[131] G. Y. Guralchuk, I. K. Katrunov A. V. Sorokin, S. L. Yefimova, A. N. Lebedenko, Yu. V. Malyukin, and S. M. Yarmoluk. Specificity of cyanine dye l-21 aggregation in solutions with nucleic acids. *J. Fluoresc.*, 17:370–376, 2007. See pages 36, 102.

[132] H. Zimmermann and G. Scheibe. Zur konstitution und lichtabsorption der reversibel polymeren form des pseudoisocyanins. *Z. Elektrochem.*, 60:566–569, 1956. See pages 36, 102.

[133] Shiekh Zia Uddin, Eran Rabani, and Ali Javey. Universal inverse scaling of exciton–exciton annihilation coefficient with exciton lifetime. *Nano Lett.*, 21:424–429, 2021. See page 36.

[134] Rohit Chikkaraddy, Bart de Nijs, Felix Benz, Steven J. Barrow, Oren A. Scherman, Edina Rosta, Angela Demetriadou, Peter Fox, Ortwin Hess, and Jeremy J. Baumberg. Single-molecule strong coupling at room temperature in plasmonic nanocavities. *Nature*, 535(7610):127–130, 2016. See page 41.

[135] Ora Bitton, Satyendra Nath Gupta, and Gilad Haran. Quantum dot plasmonics: from weak to strong coupling. *Nanophotonics*, 8(4):559–575, 2019. See page 41.

[136] Xu Shi, Kosei Ueno, Tomoya Oshikiri, Quan Sun, Keiji Sasaki, and Hiroaki Misawa. Enhanced water splitting under modal strong coupling conditions. *Nat. Nanotechnol.*, 13:953–958, 2018. See pages 41, 58.

[137] Yoshiki Suganami, Tomoya Oshikiri, Xu Shi, and Hiroaki Misawa. Water oxidation under modal ultrastrong coupling conditions using gold/silver alloy nanoparticles and fabry–pérot nanocavities. *Angew. Chem. Int. Ed.*, 60(34):18438–18442, 2021. See pages 41, 58.

[138] Linhan Lin, Mingsong Wang, Xiaoling Wei, Xiaolei Peng, Chong Xie, and Yuebing Zheng. Photoswitchable rabi splitting in hybrid plasmon–waveguide modes. *Nano Letters*, 16(12):7655–7663, 2016. See page 41.

[139] Daniel O. Sigle, Liwu Zhang, Sandrine Ithurria, Benoit Dubertret, and Jeremy J. Baumberg. Ultrathin cdse in plasmonic nanogaps for enhanced photocatalytic water splitting. *J. Phys. Chem. Lett.*, 6(7):1099–1103, 2015. See page 41.

[140] Tomoya Oshikiri, Haruki Jo, Xu Shi, and Hiroaki Misawa. Boosting hydrogen evolution at visible light wavelengths by using a photocathode with modal strong coupling between plasmons and a fabry-pérot nanocavity. *Eur. J. Chem.*, 28(24):e202200288, 2022. See page 41.

[141] Xianzhong Yang, Hua Yu, Xiao Guo, Qianqian Ding, Tonu Pullerits, Rongming Wang, Guangyu Zhang, Wenjie Liang, and Mengtao Sun. Plasmon-exciton coupling of monolayer mos2-ag nanoparticles hybrids for surface catalytic reaction. *Mat. Today Energy*, 5:72–78, 2017. See page 41.

[142] Zhong-Jian Yang, Tomasz J. Antosiewicz, and Timur Shegai. Role of material loss and mode volume of plasmonic nanocavities for strong plasmon-exciton interactions. *Opt. Express*, 24(18):20373–20381, Sep 2016. See pages 41, 54, and 66.

[143] Gülis Zengin, Göran Johansson, Peter Johansson, Tomasz J. Antosiewicz, Mikael Käll, and Timur Shegai. Approaching the strong coupling limit in single plasmonic nanorods interacting with J-aggregates. *Sci. Rep.*, 3(1):3074, 2013. See pages 41, 54, and 66.

[144] Dzmitry Melnikau, Diana Savateeva, Konstantin I. Rusakov, and Yury P. Rakovich. Whispering gallery mode emission from a composite system of j-aggregates and photonic microcavity. *J. Lumin.*, 145:138–143, 2014. See pages 41, 55.

[145] Ilya V. Doronin, Alexey S. Kalmykov, Alexander A. Zyablovsky, Evgeny S. Andrianov, Boris N. Khlebtsov, Pavel N. Melentiev, and Victor I. Balykin. Resonant concentration-driven control of dye molecule photodegradation via strong optical coupling to plasmonic nanoparticles. *Nano Letters*, 22(1):105–110, 2022. See page 41.

[146] Dietmar Möbius. Scheibe aggregates. *Adv. Mater.*, 7:437–444, 1995. See page 41.

[147] A. Eisfeld and J.S. Briggs. The j- and h-bands of organic dye aggregates. *Chemical Physics*, 324(2):376–384, 2006. See page 41.

[148] A. Jumbo-Nogales, V. Krivenkov, K. Rusakov, A. S. Urban, M. Grzelczak, and Y. P. Rakovich. Cross determination of exciton coherence length in j-aggregates. *The Journal of Physical Chemistry Letters*, 13(43):10198–10206, 2022. See pages 41, 54.

[149] Gregory S. Engel. Quantum coherence in photosynthesis. *Procedia Chem.*, 3(1):222–231, 2011. 22nd Solvay Conference on Chemistry. See page 42.

[150] Lu Wang, Morteza Hasanzadeh Kafshgari, and Michel Meunier. Optical properties and applications of plasmonic-metal nanoparticles. *Adv. Funct. Mater.*, 30(51):2005400, 2020. See page 42.

[151] Julia L Bricks, Yuri L Slominskii, Ihor D Panas, and Alexander P Demchenko. Fluorescent j-aggregates of cyanine dyes: basic research and applications review. *Methods Appl. Fluoresc.*, 6(1):012001, 2017. See pages 42, 88.

[152] Matthew S. Kirschner, Wendu Ding, Yuxiu Li, Craig T. Chapman, Aiwen Lei, Xiao-Min Lin, Lin X. Chen, George C. Schatz, and Richard D. Schaller. Phonon-driven oscillatory plasmonic excitonic nanomaterials. *Nano Letters*, 18(1):442–448, 2018. See page 42.

[153] Manish Kumar, Jyotirban Dey, Swathi Swaminathan, and Manabendra Chandra. Shape dependency of the plasmon–exciton interaction at the nanoscale: Interplay between the plasmon local density of states and the plasmon decay rate. *The Journal of Physical Chemistry C*, 126(18):7941–7948, 2022. See page 42.

[154] A. P. Deshmukh. *Tuning the Excitonic Properties of Two-Dimensional Molecular Aggregates Across the Visible and Shortwave Infrared*. PhD thesis, UCLA, 2021. See page 46.

[155] Tsz Him Chow, Nannan Li, Xiaopeng Bai, Xiaolu Zhuo, Lei Shao, and Jianfang Wang. Gold nanobipyramids: An emerging and versatile type of plasmonic nanoparticles. *Acc. Chem. Res.*, 52(8):2136–2146, 2019. See page 47.

[156] Brian J. Walker, Gautham P. Nair, Lisa F. Marshall, Vladimir Bulović, and Moungi G. Bawendi. Narrow-band absorption-enhanced quantum dot/j-aggregate conjugates. *J. Am. Chem. Soc.*, 131(28):9624–9625, 2009. See page 48.

[157] Yurui Xue, Xun Li, Hongbin Li, and Wenke Zhang. Quantifying thiol–gold interactions towards the efficient strength control. *Nat. Commun.*, 5(1):4348, 2014. See page 49.

[158] Yohei Ishida, Jun Suzuki, Ikumi Akita, and Tetsu Yonezawa. Ultrarapid cationization of gold nanoparticles via a single-step ligand exchange reaction. *Langmuir*, 34(36):10668–10672, 2018. See page 49.

[159] Do Thi Hue, Tran Thi Thu Huong, Pham Thi Thu Ha, Tran Thu Trang, Nghiem Thi Ha Lien, and Vu Xuan Hoa. The dependence of medium refractive index on optical properties of gold nanorods and their SERS application. *AIP Adv.*, 11(5):055319, 2021. See page 49.

[160] Xiangsheng Liu, Haoyuan Huang, Qiao Jin, and Jian Ji. Mixed charged zwitterionic self-assembled monolayers as a facile way to stabilize large gold nanoparticles. *Langmuir*, 27(9):5242–5251, 2011. See page 51.

[161] Dzmitry Melnikau, Pavel Samokhvalov, Ana Sánchez-Iglesias, Marek Grzelczak, Igor Nabiev, and Yury P. Rakovich. Strong coupling effects in a plexciton system of gold nanostars and j-aggregates. *J. Lumin.*, 242:118557, 2022. See pages 53, 55, 64, 68, and 86.

[162] T. Yoshie, A. Scherer, J. Hendrickson, G. Khitrova, H. M. Gibbs, G. Rupper, C. Ell, O. B. Shchekin, and D. G. Deppe. Vacuum Rabi splitting with a single quantum dot in a photonic crystal nanocavity. *Nature*, 432(7014):200–203, 2004. See pages 54, 66.

[163] G. Khitrova, H. M. Gibbs, M. Kira, S. W. Koch, and A. Scherer. Vacuum Rabi splitting in semiconductors. *Nat. Phys.*, 2(2):81–90, 2006. See pages 54, 66.

[164] J. J. Hopfield. Theory of the contribution of excitons to the complex dielectric constant of crystals. *Phys. Rev.*, 112:1555–1567, Dec 1958. See page 54.

[165] K.-H. Feller, R. Gadonas, V. Krasauskas, V. Fidler, and S. Vajda. Time-Resolved Spectroscopy of Polymethine J-Aggregates. *Laser Chemistry*, 11:287617, 1900. Publisher: Hindawi Publishing Corporation. See pages 54, 73.

[166] Oleg P. Dimitriev, Johannes Zirzlmeier, Arjun Menon, Yuri Slominskii, and Dirk M. Guldi. Exciton dynamics in j- and h-aggregates of a tricarbocyanine near-infrared dye. *The Journal of Physical Chemistry C*, 125(18):9855–9865, 2021. See pages 54, 73.

[167] Frank C. Spano and Shaul Mukamel. Superradiance in molecular aggregates. *J. Chem. Phys.*, 91(2):683–700, 1989. See pages 54, 55.

[168] T. L. Jennings, M. P. Singh, and G. F. Strouse. Fluorescent lifetime quenching near d = 1.5 nm gold nanoparticles: Probing nset validity. *J. Am. Chem. Soc.*, 128(16):5462–5467, 2006. See pages 55, 73.

[169] J. Li, A. V. Krasavin, L. Webster, P. Segovia, A. V. Zayats, and D. Richards. Spectral variation of fluorescence lifetime near single metal nanoparticles. *Sci. Rep.*, 6(6):21349, 2016. See pages 55, 73.

[170] Klaus. Kemnitz, Keitaro. Yoshihara, and Tadaaki. Tani. Short and excitation-independent fluorescence lifetimes of j-aggregates adsorbed on silver(i) bromide and silica. *J. Phys. Chem.*, 94(7):3099–3104, 1990. See page 57.

[171] Yaguang Wang, Xu Shi, Tomoya Oshikiri, and Hiroaki Misawa. Improved water splitting efficiency of au-np-loaded ga2o3 thin films in the visible region under strong coupling conditions. *Nanoscale Adv.*, 5:119–123, 2023. See page 58.

[172] F. Galego, J.and Garcia-Vidal and J. Feist. Suppressing photochemical reactions with quantized light fields. *Nat. Commun.*, 7(13841), 2016. See pages 61, 74.

[173] Felipe Herrera and Frank C. Spano. Cavity-controlled chemistry in molecular ensembles. *Phys. Rev. Lett.*, 116:238301, Jun 2016. See pages 61, 74.

[174] E. Orgiu, J. George, J. A. Hutchison, E. Devaux, J. F. Dayen, B. Doudin, F. Stellacci, C. Genet, J. Schachenmayer, C. Genes, G. Pupillo, P. Samorì, and T. W. Ebbesen. Conductivity in organic semiconductors hybridized with the vacuum field. *Nature Materials*, 14(11):1123–1129, November 2015. See page 61.

[175] Johannes Schachenmayer, Claudiu Genes, Edoardo Tignone, and Guido Pupillo. Cavity-enhanced transport of excitons. *Phys. Rev. Lett.*, 114:196403, May 2015. See page 61.

[176] Alba Jumbo-Nogales, Anish Rao, Adam Olejniczak, Marek Grzelczak, and Yury Rakovich. Unveiling the synergy of coupled gold nanoparticles and j-aggregates in plexcitonic systems for enhanced photochemical applications. *Nanomaterials*, 14(1), 2024. See pages 61, 73, and 74.

[177] Natalie Groysman, Zulfiya Orynbayeva, Marina Katz, Sofiya Kolusheva, Marina Khanin, Michael Danilenko, and Raz Jelinek. Membrane processes and biophysical characterization of living cells decorated with chromatic polydiacetylene vesicles. *Biochimica et Biophysica Acta (BBA) - Biomembranes*, 1778(5):1335–1343, 2008. See page 64.

[178] Dzmitry Melnikau, Ruben Esteban, Diana Savateeva, Ana Sánchez-Iglesias, Marek Grzelczak, Mikolaj K. Schmidt, Luis M. Liz-Marzán, Javier Aizpurua, and Yury P. Rakovich. Rabi splitting in photoluminescence spectra of hybrid systems of gold nanorods and j-aggregates. *The Journal of Physical Chemistry Letters*, 7(2):354–362, 2016. See pages 68, 71, 77, and 101.

[179] D. Melnikau, D. Savateeva, Andrey L. Susha, A.and Rogach, and Yury P. Rakovich. Strong plasmon-exciton coupling in a hybrid system of gold nanostars and j-aggregates. *Nanoscale Res Lett*, 8(134), 2013. See pages 68, 71, and 77.

[180] Panit Chantharasupawong, Laurene Tetard, and Jayan Thomas. Coupling enhancement and giant rabi-splitting in large arrays of tunable plexcitonic substrates. *The Journal of Physical Chemistry C*, 118(41):23954–23962, 2014. See page 71.

[181] Martin Wersäll, Jorge Cuadra, Tomasz J. Antosiewicz, Sinan Balci, and Timur Shegai. Observation of mode splitting in photoluminescence of individual plasmonic nanoparticles strongly coupled to molecular excitons. *Nano Letters*, 17(1):551–558, 2017. See pages 71, 72, and 84.

[182] Gülis Zengin, Göran Johansson, Peter Johansson, Tomasz J. Antosiewicz, Mikael Käll, and Timur Shegai. Observation of mode splitting in photoluminescence of individual plasmonic nanoparticles strongly coupled to molecular excitons. *Nano Letters*, 17(1):551–558, 2017. See page 72.

[183] Sergio Gómez-Graña, Fabien Hubert, Fabienne Testard, Andrés Guerrero-Martínez, Isabelle Grillo, Luis M. Liz-Marzán, and Olivier Spalla. Surfactant (bi)layers on gold nanorods. *Langmuir*, 28(2):1453–1459, 2012. See page 88.

[184] Kristina Ilina and Maged Henary. Cyanine dyes containing quinoline moieties: History, synthesis, optical properties, and applications. *Chemistry – A European Journal*, 27(13):4230–4248, 2021. See page 88.

[185] Wafa Mazi. *NEAR-INFRARED FLUORESCENT PROBES FOR SENSITIVE DETERMINATION OF LYSOSOMAL & MITOCHONDRIAL pH IN LIVE CELLS*. PhD thesis, MICHIGAN TECHNOLOGICAL UNIVERSITY, 2019. See page 88.

[186] T. Y. Fonkui, M. I. Ikhile, P. B. Njobeh, and D. T. Ndinteh. Benzimidazole schiff base derivatives: synthesis, characterization and antimicrobial activity. *BMC Chemistry*, 13(127), 2019. See page 88.

[187] N. R. Jana, L. Gearheart, and C. J. Murphy. Seed-mediated growth approach for shape-controlled synthesis of spheroidal and rod-like gold nanoparticles using a surfactant template. *Advanced Materials*, 13(18):1389–1393, 2001. See page 98.

[188] Babak Nikoobakht and Mostafa A. El-Sayed. Preparation and growth mechanism of gold nanorods (nrs) using seed-mediated growth method. *Chemistry of Materials*, 15(10):1957–1962, 2003. See page 98.

[189] Reshmi Thomas, Anoop Thomas, Saranya Pullanchery, Linta Joseph, Sanoop Mambully Somasundaran, Rotti Srinivasamurthy Swathi, Stephen K. Gray, and K. George Thomas. Plexcitons: the role of oscillator strengths and spectral widths in determining strong coupling. *ACS Nano*, 12:402–415, 2018. See page 102.

[190] Narumi Sato, Takuya Fujimura, Tetsuya Shimada, Tadaaki Tani, and Shinsuke Takagi. J-aggregate formation behavior of a cationic cyanine dye on inorganic layered material. *Tetrahedron Lett.*, 56(22):2902–2905, 2015. See page 102.

[191] Svetlana Yefimova, Alexander Sorokin, I. Katrunov, and Yurii Malyukin. Exciton localization effects in nanoscale molecular clusters (j-aggregates). *Low Temp. Phys.*, 37, 2011. See page 102.

[192] I.G. Scheblykin, M.M. Bataiev, M. Van der Auweraer, and A.G. Vitukhnovsky. Dimensionality and temperature dependence of the radiative lifetime of j-aggregates

with davydov splitting of the exciton band. *Chemical Phys. Lett.*, 316:37–44, 2000. See pages 102, 103.

[193] Bricker WP, Banal JL, Stone MB, and Bathe M. Molecular model of j-aggregated pseudoisocyanine fibers. *J. Chem. Phys.*, 149, 2018. See page 102.

[194] Naoki Fukutake and Takayoshi Kobayashi. Size distribution of pseudoisocyanine (pic) j-aggregates studied by near-field absorption spectroscopy. *Chem. Phys. Lett.*, 356:368–374, 2002. See page 102.

[195] Alexander V. Sorokin, Alexander A. Zabolotskii, Nikita V. Pereverzev, Svetlana L. Yefimova, Yury V. Malyukin, and Alexander I. Plekhanov. Plasmon controlled exciton fluorescence of molecular aggregates. *J. Phys. Chem. C*, 118:7599–7605, 2014. See page 102.

[196] Nadia Vranken, Mark Van der Auweraer, Frans C. De Schryver, Hugo Lavoie, Philippe Bélanger, and Christian Salesse. Influence of molecular structure on the aggregating properties of thiacarbocyanine dyes adsorbed to langmuir films at the air-water interface. *Langmuir*, 16(24):9518–9526, 2000. See pages 102, 103.

[197] U. De Rossi, S. Daehne, and M. Lindrum. Increased coupling size in j-aggregates through n-n-alkyl betaine surfactants. *Langmuir*, 12:1159–1165, 1996. See page 103.

[198] Surendra B. Anantharaman, Joachim Kohlbrecher, Gabriele Rainò, Sergii Yakunin, Thilo Stöferle, Jay Patel, Maksym Kovalenko, Rainer F. Mahrt, Frank A. Nüesch, and Jakob Heier. Enhanced room-temperature photoluminescence quantum yield in morphology controlled j-aggregates. *Adv. Sci.*, 8:1903080, 2021. See page 103.

[199] E. Rousseau, M. Van der Auweraer, and F. C. De Schryver. Steady-state and time-resolved spectroscopy of a self-assembled cyanine dye multilayer. *Langmuir*, 16:8865–8870, 2000. See page 103.